Vector Boson Pair Production in NNLO QCD

Dissertation

zur

Erlangung der naturwissenschaftlichen Doktorwürde
(Dr. sc. nat.)

vorgelegt der

Mathematisch-naturwissenschaftlichen Fakultät

der

Universität Zürich

von

Dirk Rathlev

aus

Deutschland

Promotionskomitee

PD Dr. Massimiliano Grazzini (Vorsitz und Leitung der Dissertation)
Prof. Dr. Thomas Gehrmann
Prof. Dr. Ben Kilminster
Prof. Dr. Stefano Pozzorini

Zürich, 2015

Abstract

The first run of the Large Hadron Collider can be considered a major success for particle physics. With the discovery of a scalar resonance closely resembling the Standard Model Higgs boson, all particles predicted by the Standard Model now seem to be experimentally accounted for. However, no evidence for beyond-the-Standard-Model physics has been found. One of the main objectives of the second run, which started in spring this year, is to further characterise the newly discovered Higgs boson by studying its properties more precisely. Another main objective is to continue the search for new physics. Both objectives require a detailed understanding of Standard Model physics, based on precise theoretical predictions.

Obtaining accurate predictions is however highly non-trivial. One of the main tools available to perform quantitative computations is perturbation theory. In perturbative calculations the prediction for an observable is obtained by expanding the result in a power series and retaining only finitely many terms. The accuracy of the prediction can be systematically improved by taking into account higher orders in the expansion. In this thesis, we report on progress in developing a numerical code capable of computing next-to-next-to-leading order (NNLO) corrections to a wide class of processes relevant for the physics programme at the Large Hadron Collider.

As an application, we present detailed phenomenological predictions for several diboson production processes at the LHC and, if available, compare with experimental measurements performed by the ATLAS and CMS collaborations.

Zusammenfassung

Der erste Run des Large Hadron Colliders kann als grosser Erfolg für die Teilchenphysik gewertet werden. Mit der Entdeckung eines skalaren Teilchens, das grosse Ähnlichkeit zum Higgs-Boson des Standardmodells aufweist, scheinen jetzt alle durch das Standardmodell vorhergesagten Teilchen experimentell bestätigt zu sein. Allerdings wurden keinerlei Hinweise auf Physik jenseits des Standardmodells gefunden. Eines der Hauptziele des zweiten Runs, der im Frühling dieses Jahres gestartet ist, ist die genaue Untersuchung des neu entdeckten Higgs-Bosons. Ein zweites wichtiges Ziel ist die Fortsetzung der Suche nach neuer Physik. Beide Ziele erfordern ein detailliertes Verständnis von Standardmodell-Physik in Form von genauen theoretischen Vorhersagen.

Im Rahmen des Standardmodells präzise Vorhersagen zu erhalten ist allerdings hochgradig nicht-trivial. Eines der wichtigsten Werkzeuge zum Durchführen quantitativer Rechnungen ist die Störungstheorie. In der Störungstheorie wird die Vorhersage für eine Observable erhalten, indem das Ergebnis als eine nach endlich vielen Termen abgeschnittene Potenzreihe geschrieben wird. Die Genauigkeit der Vorhersage kann durch das Berechnen weiterer Terme in der Entwicklung systematisch verbessert werden. In dieser Arbeit behandeln wir Fortschritte bei der Entwicklung eines numerischen Codes, der in der Lage ist, Korrekturen zweiter Ordnung (NNLO) für eine breite Klasse von für LHC-Messungen relevanten Prozessen zu berechnen.

Als eine Anwendung des numerischen Codes beschreiben wir detaillierte phänomenologische Vorhersagen für verschiedene Vektorboson-Paarprozesse am LHC und vergleichen, wenn möglich, mit experimentellen Daten der ATLAS- und CMS-Kollaborationen.

Contents

1 Introduction

The current understanding of all known fundamental particles and their interactions is based on the Standard Model of particle physics (SM). The SM is a $\mathrm{U}(1)_Y \times \mathrm{SU}(2)_L \times \mathrm{SU}(3)_C$ gauge theory and consistently describes electromagnetic, weak and strong interactions, with only gravity being unaccounted for. The predictions of the SM have been tested in a wide range of high-energy scattering experiments at particle colliders, with LEP, HERA, the Tevatron and the LHC being the most recent ones, and also by several high-precision measurements at lower energies. So far, the SM has withstood every experimental test, making it one of the most successful theoretical descriptions ever devised [1]. In addition, with the discovery of a Higgs boson at the LHC in 2012 [2, 3], all particles predicted by the SM are now experimentally established.

However, besides the absence of gravity from the equations of the SM, which is already an unambiguous sign of its incompleteness as a fundamental theory, the SM in its current formulation suffers from a number of conceptual and phenomenological shortcomings. These shortcomings are often interpreted as indirect evidence for the existence of beyond-the-SM (BSM) physics at energy scales accessible at the LHC, and thus provide a significant part of the motivation for the ongoing LHC physics programme.

On the conceptual side, one of the most pressing issues is the so-called hierarchy problem [4, 5]. At its core, the hierarchy problem is the observation of a large discrepancy between the typical energy scale of electromagnetic and weak interactions, given by the Higgs boson mass $m_H \approx 125\,\mathrm{GeV}$, and the typical energy scale of gravity of around $10^{19}\,\mathrm{GeV}$. Without BSM physics present at energy scales not far above 1 TeV, the Higgs mass is not stable under quantum corrections originating from physics at higher energy scales, and its experimental value thus seems to be unnaturally small. In practice, the Higgs boson mass can be fine-tuned to match the experimentally observed value; however, this requires a fundamental parameter of the theory to be adjusted to an accuracy of dozens of digits, which is conceptually unsatisfying.

Observational evidence hinting at the existence of new physics comes from cosmology and astrophysics. Less than 20% of all gravitationally interacting matter in the universe can be ascribed to known particles, the rest consisting of so called dark matter [6]. The favoured explanation for this discrepancy is the existence of a currently unknown fundamental particle, which interacts only very weakly with any known particle and whose mass could lie in the energy region accessible at the LHC [7].

Though striking signatures of new phenomena can in principle appear whenever new energy scales are probed in a collider experiment, particle physics nowadays has to be considered a precision science, in the sense that new discoveries and in particular their

interpretation will most likely require a detailed understanding of background effects from known physics. An example is the characterisation of the Higgs particle discovered at the LHC. While evidence for its existence first showed up as an excess in the number of photon and Z-boson pairs produced around an invariant mass of 125 GeV above a mostly flat background, confidently identifying the newly discovered resonance as the Higgs boson of the SM requires detailed measurements of its properties, for which in turn precise theory input for both background and signal predictions is crucial.

However, extracting precise predictions from the equations defining the SM is often highly non-trivial, since they cannot be solved in closed form. One of the standard tools to obtain quantitative results in quantum field theory is perturbation theory, i.e. the solution of the underlying equations in terms of a power series expansion in some small parameter, usually taken to be the relevant coupling constant. To obtain predictions for cross sections of scattering processes, the perturbative expansion has to be performed on a process-by-process basis, and the computation of each term in this expansion requires a significant amount of work, with the corresponding complexity growing roughly exponentially. This often makes the order up to which a specific observable can be computed the limiting factor in the accuracy of the theoretical prediction.

Strong interactions are described by the $\mathrm{SU}(3)_C$ sector of the SM, called quantum chromodynamics (QCD), while electromagnetic and weak interactions are described by the electroweak (EW) $\mathrm{SU}(2)_L \times \mathrm{U}(1)_Y$ sector. As the coupling constant of QCD, $\alpha_\mathrm{S} \approx 0.1$, is much larger than the corresponding EW coupling constant $\alpha_e \approx 1/128$, QCD effects are expected to dominate higher-order corrections to most observables at hadron colliders such as the LHC. Often, obtaining a leading order (LO) prediction for a given observable is relatively straightforward. A LO prediction however usually only provides an order-of-magnitude estimate, requiring the computation of at least next-to-leading order (NLO) QCD corrections, which typically provide a theoretical accuracy at the level of $\mathcal{O}(10-20\%)$. For processes with either large perturbative corrections (such as Higgs boson production in gluon fusion) or processes which can be measured very precisely (e.g. vector boson and vector boson pair production) the computation of even higher-order perturbative QCD corrections – at least next-to-next-to-leading order (NNLO) – is necessary to fully exploit the physics potential of the LHC.

One of the main challenges when computing higher-order corrections is the appearance of infrared (IR) singularities. While these singularities are guaranteed to cancel out of predictions for meaningful physical observables, their presence at intermediate stages of the calculation prevents the application of straightforward numerical methods. On the other hand, performing the computation analytically requires the evaluation of complicated phase-space integrals, which often have to be re-evaluated on an observable-by-observable basis.

At NLO, the problem of handling the IR singularities has been overcome by the formulation of process-independent subtraction schemes [8–10]. These subtraction schemes can be used to re-organise the intermediate singularities in such a way that all phase-space integrations can be performed numerically, thus allowing for the computation of higher-order

corrections to arbitrary observables for a given process. Implementations of general NLO subtraction schemes have been combined with codes capable of numerically computing the virtual one-loop amplitude for a given process [11–13], the second main ingredient of a generic NLO computation. The emergence of fully integrated and general programs [12,14] lead to the so-called NLO revolution. A few years ago, many NLO computations used to be cumbersome projects often spanning several years. Nowadays, they can be performed in days, with only minimal manual work required. Furthermore, the available tools have reached a state of maturity that allows them to be used by non-specialists, for example by model builders or by experimental physicists. This has helped to push the standard accuracy in particle physics to NLO.

At NNLO, the situation is much more complicated. The structure of the intermediate IR singularities is significantly more involved compared to the situation at NLO, and – despite significant progress, see for example Refs. [15–18] – currently no fully automated general subtraction scheme is available at NNLO. In addition, the two-loop virtual amplitudes needed in a NNLO computation have to be obtained via very involved analytical calculations, to be performed on a process-by-process basis. However, at least in the class of $2 \to 2$ processes, such as vector boson pair production, many relevant amplitudes have become available in the recent past [19–22], and the bottle-neck in providing phenomenological results now lies with assembling all the separate pieces into a full NNLO computation.

While many important results at NNLO accuracy have been obtained over the last few years, see for example Refs. [23–37], full automation is unlikely to be achieved in the immediate future. It will however be shown in this thesis that it is possible to re-use large parts of the existing NLO technology also in the context of NNLO computations, facilitating the practical implementations and allowing for a partial automation. In fact, the real-emission contribution to any NNLO quantity can be obtained from a pure NLO computation, for which well-tested techniques are available. By restricting to processes with a non-QCD final state, a particular subtraction scheme – q_{T} subtraction [38] – can be used, which makes the separation of the computation into NLO- and genuinely NNLO-like pieces fully explicit.

As we will show, q_{T} subtraction can be automated to essentially the same degree as commonly used subtraction schemes at NLO. In the end, we are able to organise the computation in such a way that the only process-dependent input in addition to quantities already appearing in NLO calculations are the two-loop amplitudes. The outcome of this project is a framework named Matrix[1], built upon the NLO code Munich [39]. Matrix allows for the automation of large parts of the calculation, facilitating both future applications and providing valuable experience for the ongoing efforts to fully automate NNLO computations.

The main application of the framework developed in this thesis is the computation of NNLO corrections to diboson production processes, i.e. to the production of two vector bosons, at the LHC. In particular, we present NNLO predictions for $Z\gamma$, $W\gamma$, W^+W^- and

[1] Matrix is the abbreviation of "Munich Automates qT subtraction and Resummation to Integrate Cross Sections", by M. Grazzini, S. Kallweit, D. Rathlev, M. Wiesemann.

ZZ production. In the case of W^+W^- and ZZ production we also present results beyond fixed-order perturbation theory, in which the logarithmically-enhanced contributions to the low transverse-momentum spectrum are resummed to all orders in perturbation theory.

The phenomenological results collected in this thesis are highly relevant for the interpretation of ongoing LHC measurements. In particular, they help to explain discrepancies between measurements and existing NLO predictions, for example in the ATLAS measurement of $W\gamma$ production [32, 40] and the ATLAS and CMS measurements of W^+W^- production [28, 41–44].

As arbitrary SM processes with non-QCD final states can be included into our framework, we will at some point be able to provide a single code to obtain fully differential NNLO predictions for a wide class of processes. The same code will also be able to perform resummed computations of transverse-momentum spectra up to next-to-next-to-leading logarithmic accuracy.

This thesis is organised as follows. Chapter 2 provides a brief overview of the most important aspects of QCD. In particular, the universal structure of IR singularities is explained in some detail. Chapter 3 starts with an overview of existing strategies on how to handle IR singularities in NLO and NNLO computations and then summarises the formalism of transverse-momentum resummation, which in turn forms the basis for the discussion of q_{T} subtraction. Chapter 4 provides details of our implementation of q_{T} subtraction into a numerical code and also discusses some of the challenges faced when performing NNLO computations in practice. Chapter 5 is the main part of this thesis and contains an overview of the phenomenological results obtained so far with our framework. In particular, we discuss $V\gamma$ production in Section 5.1, ZZ production in Section 5.2 and W^+W^- production in Section 5.3. Section 5.4 contains results for the resummed transverse-momentum spectra of ZZ and W^+W^- pairs. Chapter 6 provides a brief summary and an outlook.

2 Quantum chromodynamics

In this chapter we discuss the most important aspects of QCD, namely its running coupling, asymptotic freedom and ultraviolet and infrared singularities. Infrared singularities are one of the main complications when computing higher-order corrections in QCD, and we use our discussion both to fix terminology and to outline the problems to be addressed in Chapter 3.

2.1 The QCD Lagrangian

Quantum chromodynamics is a non-Abelian gauge theory with gauge group SU(3). The gauge charge is called *colour* and the gauge bosons *gluons*. QCD contains three (up to their masses identical) families of fermionic matter particles, each consisting of one up-type and one down-type quark. The quarks are referred to by their *flavour*. The three up-type quarks are called up, charm and top quark and carry an electrical charge of $+2/3$, the three down-type quarks are called down, strange and bottom quark and carry an electrical charge of $-1/3$. Their left-handed versions are also charged under $\mathrm{SU}(2)_W$.

The top quark is by far the heaviest quark with mass[1] $m_t \approx 172\,\mathrm{GeV}$, while the next-to-heaviest quark, the bottom quark, has a mass of $m_b \approx 4.75\,\mathrm{GeV}$ [1]. For processes at the electroweak scale $\sim 100\,\mathrm{GeV}$ and above, all quarks except for the top quark can be approximately assumed to be massless[2]. In the approximation where the N_f lightest quarks are considered to be massless, QCD exhibits a global $\mathrm{SU}(\mathrm{N_f})$ *flavour symmetry*, which can – and has been – used to classify the possible bound states of quarks: each baryon (a bound state of three quarks) and each meson (a bound state of a quark and an antiquark) can be interpreted as a vector in an irreducible representation of $\mathrm{SU}(\mathrm{N_f})$, related to the other bound states in the same representation by $\mathrm{SU}(\mathrm{N_f})$ flavour rotations.

As QCD is an unbroken gauge theory, its Lagrangian is of standard Yang-Mills SU(N) form and can be written as

$$\mathcal{L} = \mathcal{L}_{\text{quarks}} + \mathcal{L}_{\text{gauge}} + \mathcal{L}_{\text{gauge fix}} + \mathcal{L}_{\text{ghosts}}. \tag{2.1}$$

[1] All quark masses in this thesis are stated in the on-shell scheme.

[2] The bottom quark can be seen as a border case and its mass is sometimes taken into account, in particular if the top quark enters the process non-trivially. We will encounter such an example in Section 5.3.

The first two terms contain the fermion and gauge terms:

$$\mathcal{L}_{\text{quarks}} = \sum_{q=u,d,c,s,t,b} \bar{q}_i \left(\mathrm{i} \not{D}_{ij} - m_q \delta_{ij} \right) q_j, \tag{2.2}$$

$$\mathcal{L}_{\text{gauge}} = -\frac{1}{4} F^a_{\mu\nu} F^{a,\,\mu\nu}, \tag{2.3}$$

where m_q denotes the mass of the quark with flavour q. The covariant derivative and the gauge field strength tensor can be written in terms of the SU(N) gauge field A^a_μ as

$$D^\mu_{ij} = \partial^\mu \delta_{ij} + \mathrm{i} g_s A^\mu_a t^a_{ij}, \tag{2.4}$$

$$F^a_{\mu\nu} = \partial_\mu A^a_\nu - \partial_\nu A^a_\mu - g_s f^{abc} A^b_\mu A^c_\nu. \tag{2.5}$$

Here, $g_s = \sqrt{4\pi\alpha_\text{S}}$ denotes the strong coupling, and the t^a and f^{abc} are the generators and structure constants of SU(N), with $[t^a, t^b] = \mathrm{i} f^{abc} t^c$.

To quantise the theory, the gauge degeneracy has to be removed by a gauge fixing term of the form

$$\mathcal{L}_{\text{gauge fix}} = -\frac{1}{2\xi} G(A), \tag{2.6}$$

where the choice $G(A) = |\partial_\mu A^{a,\,\mu}|^2$ leads to the covariant gauges and $G(A) = |n_\mu A^{a,\,\mu}|^2$ (with some light-like reference vector n_μ) to the axial gauges.

To explicitly carry out the cancellation of gauge redundant degrees of freedom in the general case, a ghost term,

$$\mathcal{L}_{\text{ghosts}} = \bar{c}^a \left(-\partial^2 \delta^{ac} - g_s \partial^\mu f^{abc} A^b_\mu \right) c^c, \tag{2.7}$$

involving anticommuting scalar fields c (the ghosts) has to be introduced. Ghosts only appear as virtual particles in loops, never as physical external states. They decouple completely from the theory if an axial gauge is used.

2.2 Regularisation and renormalisation

When computing virtual (loop) corrections to QCD amplitudes, one typically encounters integrals of the form

$$\int \mathrm{d}^4 k \, \frac{1}{((k+p)^2\, k^2)}, \tag{2.8}$$

where k is the virtual momentum running in the loop and p is some fixed external momentum. These integrals are logarithmically divergent when going to very high virtualities

of the loop momentum, as can be seen by introducing an upper cutoff Λ:

$$\int \mathrm{d}^4k \, \frac{1}{(k+p)^2\, k^2} \sim \lim_{\Lambda\to\infty} \int_1^\Lambda \mathrm{d}k \, k^3 \, \frac{1}{(k^2)^2} \sim \lim_{\Lambda\to\infty} \log\Lambda. \tag{2.9}$$

These singularities, associated with the high-energy behaviour of the integrand, are called *ultraviolet* (UV) singularities. *Infrared* (IR) singularities, i.e. the divergences associated with $k \to 0$, will be discussed below in Section 2.4.

In practical computations, explicit cutoffs as in Eq. (2.9) are problematic as they do not respect the Lorentz invariance and the gauge symmetry of the theory[3] and often complicate calculations significantly. The standard procedure, which does explicitly preserve Lorentz and gauge invariance, is *dimensional regularisation* (DR), in which the number of space-time dimensions is analytically continued from 4 to $d = 4 - 2\varepsilon$. UV and IR singularities then show up as poles in the regularisation parameter ε, corresponding to the divergences in the limit $d \to 4$.

UV divergences can be completely removed from any renormalisable theory – such as QCD – by a finite number of UV counterterms. The presence of UV counterterms effectively corresponds to a redefinition of the free parameters, e.g. masses and couplings, present in the Lagrangian. This procedure can be thought of as absorbing the infinities due to UV divergences into the bare parameters of the theory. However, the renormalisation conditions, i.e. the precise way in which the infinities are absorbed, lead to ambiguities for the renormalised parameters. The details depend on the renormalisation scheme used. In the frequently used $\overline{\mathrm{MS}}$ scheme for instance, the renormalisation conditions have to be fixed at a specific scale, the so called *renormalisation scale*, μ_R. For example, one might set the two-point Green's function at the fixed virtuality $p^2 = -\mu_R^2$ to a fixed value.

This procedure introduces a μ_R dependence, which is unphysical and has to cancel out of any physical observable; however, in perturbative calculations, where the prediction for a given observable is obtained by truncating the perturbative series at a fixed finite order, a non-vanishing μ_R dependence remains. As this dependence has to cancel out once all orders have been taken into account, its size is often used to obtain a rough estimate of missing higher-order contributions in a perturbative computation.

2.3 QCD running coupling and asymptotic freedom

In QCD, one of the most important consequences of the renormalisation procedure is the fact that the coupling constant α_S acquires an explicit renormalisation scale dependence, $\alpha_\mathrm{S} = \alpha_\mathrm{S}(\mu_R)$. The dependence of α_S on μ_R can be computed explicitly in perturbation theory, starting from an unrenormalised Green's function (which has to be μ_R independent)

[3] For example, the regulated integral in Eq. (2.9) is no longer invariant under Lorentz boosts of the external momentum p.

to derive a differential equation of the form

$$\frac{\partial \alpha_{\mathrm{S}}(\mu_R)}{\partial \log \mu_R^2} = -\alpha_{\mathrm{S}}(\mu_R)\, \beta(\alpha_{\mathrm{S}}(\mu_R)), \tag{2.10}$$

where β is the *beta function* of QCD. β can be computed perturbatively:

$$\beta(\alpha_{\mathrm{S}}) = \alpha_{\mathrm{S}}\beta_0 + \alpha_{\mathrm{S}}^2\beta_1 + \ldots, \tag{2.11}$$

where the perturbative coefficients β_i are known up to $i = 3$ [45,46]. Solving Eq. (2.10) to the lowest order, one obtains

$$\alpha_{\mathrm{S}}(\mu_R) = \frac{\alpha_{\mathrm{S}}(\mu_0)}{1 + \alpha_{\mathrm{S}}(\mu_0)\beta_0 \log \frac{\mu_R^2}{\mu_0^2}}, \tag{2.12}$$

where μ_0 is some initial scale at which α_{S} has to be fixed by external input, for example by a direct measurement.

The lowest order contribution to the beta function is given by

$$\beta_0 = \frac{11C_A - 2N_f}{12\pi}, \tag{2.13}$$

where $C_A = 3$. β_0 is positive for $N_f \leq 16$. Eq. (2.12) then implies that $\alpha_{\mathrm{S}}(\mu_R) \to 0$ for $\mu_R \to \infty$. This property of QCD, which is preserved also when higher-order contributions to the beta function in Eq. (2.11) are taken into account, is called *asymptotic freedom*. It implies that perturbation theory in α_{S} works at sufficiently high energies. At low energies however, perturbation theory breaks down. An order of magnitude estimate for the scale Λ_{QCD} at which perturbation theory is no longer valid is given by the scale at which the denominator in Eq. (2.12) vanishes, which happens at

$$\mu_R^2 = \Lambda_{\mathrm{QCD}}^2 = \mu_0^2 \exp\left[\frac{-1}{\alpha_{\mathrm{S}}(\mu_0)\beta_0}\right]. \tag{2.14}$$

Inserting the experimentally measured value for α_{S}, one obtains $\Lambda_{\mathrm{QCD}} \approx 200\,\mathrm{MeV}$.

2.4 Factorisation and perturbative computations

At hadron colliders such as the LHC, the colliding particles are – in contrast to the situation at an electron-positron collider – not elementary, but bound states of quarks and gluons. In the parton model, a proton for example can be thought of as a bound state of two up quarks and one down quark. However, QCD effects modify the effective composition of a proton. In particular, a proton also contains gluons as well as quarks and antiquarks of all flavours. The energy scales relevant for the formation of a QCD bound state are of the order of $\Lambda_{\mathrm{QCD}} \approx 200\,\mathrm{MeV}$, implying that the internal composition of hadrons is governed

by non-perturbative physics. However, the physical processes typically studied at colliders such as the LHC take place at much higher energies. This allows for the separation of soft non-perturbative physics and hard physics, which can be treated with perturbative methods. In practice, this is achieved by *factorisation*, i.e. by expressing the hadronic cross section for the process $AB \to \mathrm{F}$, where A and B are initial state hadrons (e.g. protons) and F is a final-state system, as[4]

$$\sigma_{AB\to\mathrm{F}} = \sum_{a,b} \int \mathrm{d}x_1\, \mathrm{d}x_2\, f_{a/A}(x_1,\mu_F)\, f_{b/B}(x_2,\mu_F)\, \sigma_{ab\to\mathrm{F}}(x_1x_2s,\mu_F). \tag{2.15}$$

Here, $f_{a/A}(x,\mu_F)$ denotes a parton distribution function (PDF), which can be thought of as specifying the probability of finding a parton a with momentum fraction x inside the hadron A[5]. $\sigma_{ab\to\mathrm{F}}$ denotes the cross section for the *partonic* process $ab \to \mathrm{F}$, which takes place at the energy $\sqrt{x_1x_2s}$, where s is the collider centre-of-mass energy squared. μ_F denotes the energy scale at which soft and hard physics are separated. Physical quantities should not depend on μ_F and in fact the μ_F dependence cancels in Eq. (2.15) once all pieces are combined [47]. However, in a fixed-order computation only finitely many terms in the small coupling expansion of $\sigma_{ab\to\mathrm{F}}$ are kept, and a μ_F dependence remains, which, together with the residual dependence on the renormalisation scale μ_R, is often used to obtain an estimate for the neglected higher-order contributions.

The factorisation formula Eq. (2.15) can only be proven rigorously in special cases which are sufficiently inclusive in the final state. For more exclusive observables, its validity is assumed without having been proved yet. In any case, Eq. (2.15) is only correct up to power corrections of the form $1/s^m$, which can arise from hadronisation effects and multiple parton interactions. These effects can partially be modelled with specialised tools (see Ref. [48] for a review), but are mostly assumed to be negligible for the processes studied in this thesis.

As non-perturbative quantities, the PDFs can at the moment not be obtained from first principles, but have to be measured in experiments. Typically, a number of measurements for which clean theoretical predictions exist are combined and fitted to obtain PDFs valid in wide ranges of x and for all flavours a. PDFs obtained from such fits are available from several collaborations, see Refs. [49–54].

The μ_F dependence of the PDFs, on the other hand, arises from perturbative physics at the separation scale and can thus be computed using perturbation theory. It is governed by the so-called DGLAP evolution equations, a coupled system of differential equations in μ_F, first derived in Refs. [55–57]. The existence of these equations implies that the PDFs have

[4] A second factorisation in the final state, in which the hadronisation of QCD partons produced in the collision is separated off from the hard process, has been suppressed in this formula. As will be briefly explained in Section 2.6, neglecting the hadronisation effects in the final state is often justified if suitable observables are used.

[5] Strictly speaking, beyond leading order in perturbation theory PDFs do not have such an intuitive interpretation and are in fact renormalisation scheme dependent objects. In particular, they are not true probability densities and can even become negative at certain values of their arguments.

only to be fitted at one value of μ_F and can then be evolved to any other (perturbative) scale.

The DGLAP equations in the $N_f = 1$ case, i.e. for a single quark species q (and the corresponding antiquark $\bar{q}$), take the form

$$\frac{\partial}{\partial \log \mu_F} \begin{pmatrix} f_g \\ f_q \\ f_{\bar{q}} \end{pmatrix} = \frac{\alpha_\mathrm{S}}{\pi} \begin{pmatrix} P_{g\leftarrow g} & P_{g\leftarrow q} & P_{g\leftarrow q} \\ P_{q\leftarrow g} & P_{q\leftarrow q} & P_{q\leftarrow \bar{q}} \\ P_{q\leftarrow g} & P_{\bar{q}\leftarrow q} & P_{q\leftarrow q} \end{pmatrix} \otimes \begin{pmatrix} f_g \\ f_q \\ f_{\bar{q}} \end{pmatrix}, \tag{2.16}$$

where the symbol $\otimes$ denotes a convolution,

$$[P_{b\leftarrow a} \otimes f](x) = \int_x^1 \frac{\mathrm{d}z}{z} P_{b\leftarrow a}(z) f\left(\frac{x}{z}\right), \tag{2.17}$$

and the functions $P_{b\leftarrow a}$ are the *Altarelli-Parisi splitting functions*. In Eq. (2.16) we already exploited charge conjugation invariance to substitute $P_{g\leftarrow\bar{q}} = P_{g\leftarrow q}$, $P_{\bar{q}\leftarrow g} = P_{q\leftarrow g}$ and $P_{\bar{q}\leftarrow\bar{q}} = P_{q\leftarrow q}$. To leading order in α_S, the remaining splitting functions are given by

$$P_{q\leftarrow q}(z) = C_F \left[\frac{1+z^2}{(1-z)_+} + \frac{3}{2}\delta(1-z)\right] + \mathcal{O}(\alpha_\mathrm{S}), \tag{2.18}$$

$$P_{g\leftarrow q}(z) = C_F \left[\frac{1+(1-z)^2}{z}\right] + \mathcal{O}(\alpha_\mathrm{S}), \tag{2.19}$$

$$P_{q\leftarrow g}(z) = \frac{1}{2}\left[z^2 + (1-z)^2\right] + \mathcal{O}(\alpha_\mathrm{S}), \tag{2.20}$$

$$P_{g\leftarrow g}(z) = 2C_A \left[\frac{1-z}{z} + \frac{z}{(1-z)_+} + z(1-z)\right] + \frac{11C_A - 2N_f}{6}\delta(1-z) + \mathcal{O}(\alpha_\mathrm{S}), \tag{2.21}$$

$$P_{\bar{q}\leftarrow q}(z) = \mathcal{O}(\alpha_\mathrm{S}), \tag{2.22}$$

where $C_F = 4/3$.

The generalisation of Eq. (2.16) to the multi-flavour case is achieved by introducing additional splitting functions $P_{q'\leftarrow q}$, $P_{q'\leftarrow\bar{q}}$ and $P_{\bar{q}'\leftarrow\bar{q}}$ to describe flavour-changing splittings, which only start to contribute at $\mathcal{O}(\alpha_\mathrm{S}^2)$.

The partonic cross section $\sigma_{ab\to\mathrm{F}}$ in Eq. (2.15) describes a high-energy interaction and therefore can be computed perturbatively as an expansion in α_S:

$$\sigma_{ab\to\mathrm{F}} = \sigma^{(0)}_{ab\to\mathrm{F}} + \left(\frac{\alpha_\mathrm{S}}{2\pi}\right)\sigma^{(1)}_{ab\to\mathrm{F}} + \sum_{m=2}^{\infty}\left(\frac{\alpha_\mathrm{S}}{2\pi}\right)^m \sigma^{(m)}_{ab\to\mathrm{F}}. \tag{2.23}$$

In practice, only a finite number of terms of this expansion can be computed and the series is truncated at a fixed order. If only the first term is kept, one obtains a leading order (LO) prediction for $\sigma_{ab\to\mathrm{F}}$, keeping the first two terms results in a next-to-leading order (NLO) prediction, keeping the first three terms in a next-to-next-to-leading oder (NNLO) prediction and so on.

The LO cross section for a process where the final state F contains n particles is simply given by the phase-space integral over the leading order Born-level amplitude:

$$\sigma^{(0)}_{ab\to\mathrm{F}} = \int_n \mathrm{d}\sigma^{(0)}_{ab\to\mathrm{F}}. \tag{2.24}$$

Here, $\mathrm{d}\sigma^{(0)}_{ab\to\mathrm{F}}$ is shorthand notation for

$$\mathrm{d}\sigma^{(0)}_{ab\to\mathrm{F}} = \mathrm{d}\Phi^{(n)} \left|\mathcal{M}^{(0)}_{ab\to\mathrm{F}}\right|^2 \mathcal{J}^{(n)}(\{p_i\}), \tag{2.25}$$

where

$$\mathrm{d}\Phi^{(n)} = \frac{(2\pi)^4}{2\sqrt{(k_1+k_2)^2}}\,\mathrm{d}\varphi^{(n)}, \tag{2.26}$$

$$\mathrm{d}\varphi^{(n)} = \left[\prod_{i=1}^{n} \frac{\mathrm{d}^4 p_i}{(2\pi)^3}\,\delta(p_i^2)\,\Theta(p_i^0)\right] \delta^{(4)}(k_1+k_2-\sum_{j=1}^{n} p_j) \tag{2.27}$$

denotes the n-particle phase space with initial-state momenta k_1 and k_2 and final-state momenta p_i.

$\mathcal{M}^{(0)}_{ab\to\mathrm{F}}$ in Eq. (2.25) is the leading order Born matrix element. Note that $\mathcal{M}^{(0)}_{ab\to\mathrm{F}}$ is not necessarily a tree-level amplitude (e.g. Higgs production in gluon fusion starts at the one-loop level), but has to be free of ultraviolet and infrared singularities. $\mathcal{J}^{(n)}(\{p_i\})$ is the n-particle measurement function encoding the physical observable one is interested in.

Starting from the next-to-leading order, loop corrections to the Born-level amplitude have to be included. However, after removing ultraviolet divergences by renormalisation, $\mathcal{M}^{(m)}_{ab\to\mathrm{F}}$ (for $m \geq 1$) still contains poles, which are of infrared origin, i.e. they result from the lower integration boundary in Eq. (2.9). By the KLN theorem [58–60], IR singularities are guaranteed to cancel from sensible observables (in the sense defined in Section 2.6 below) after summing over all possible reactions yielding an undistinguishable final state. In the case of scattering reactions, this necessarily includes real correction contributions, in which besides the Born-level final state F a number of additional QCD partons, i.e. quarks and gluons, are produced which are either very soft or collinear to initial- or other final-state QCD partons and thus cannot be detected in an experiment. These soft and collinear configurations give rise to IR singularities in the real-emission contribution, which in the end cancel the IR singularities from the virtual contribution.

2.5 Structure of infrared singularities

Infrared singularities originating from soft or collinear radiation can be studied explicitly and turn out to be universal in the sense that their structure does not depend on the accompanying hard process. As an illustrative example, we consider a scattering process of the form $q(k_1)\bar{q}(k_2) \to \mathrm{F}(p_1)$, where a quark with momentum k_1 and an antiquark

with momentum k_2 interact to produce a system F with momentum p_1 (F itself can be composed of an arbitrary number of individual particles). One of the initial-state particles, for example the quark, can emit an additional gluon with momentum p_2 (this subprocess would be part of the real correction to the process $pp \to \mathrm{F}$). The propagator of the initial-state quark after emitting the additional gluon contains the denominator

$$\frac{1}{(k_1 - p_2)^2 - m_q^2} = \frac{-1}{2E_g(E_q - \sqrt{E_q^2 - m_q^2}\cos\theta_{qg})}, \tag{2.28}$$

where m_q and E_q are the quark mass and energy, E_g is the gluon energy and θ_{qg} is the angle between the three-momenta of the initial-state quark and the final-state gluon. If the emitted gluon becomes soft, i.e. $E_g \to 0$, the denominator vanishes and the matrix element develops a non-integrable divergence. If one works in massless QCD, $m_q = 0$, what is usually done for either the four or the five lightest quarks, the propagator becomes

$$\frac{-1}{2E_g E_q(1 - \cos\theta_{qg})}. \tag{2.29}$$

Now, also the collinear limit $\theta_{qg} \to 0$ is divergent. The limit of a soft quark, $E_q \to 0$, however turns out to be integrable once the quark spinors are also taken into account, as we will see in the next section.

In Abelian gauge theories such as quantum electrodynamics (QED), amplitudes factorise in the limit of soft gauge boson radiation. QCD amplitudes exhibit a similar property in the soft and collinear limits of external quarks and gluons. This property is crucial for an understanding of the infrared singularities encountered in NLO and NNLO computations, and the techniques developed to handle these singularities (which are discussed to some extent in Chapter 3) rely on an explicit knowledge of the corresponding factorisation formulae. In the following, we will outline how to derive such formulae for the soft and for the collinear limits of n-particle tree-level amplitudes to leading order in α_S[6]. Generalisations, both to one-loop amplitudes and to higher orders in α_S for tree-level amplitudes, are known, see Refs. [61–64].

2.5.1 Factorisation in the soft limit

We consider a tree-level amplitude $\mathcal{M}_n$ with n external, massless QCD particles. To streamline the notation, it is useful to introduce a basis in colour space. Let $c_1, \ldots, c_n$ denote the colour indices of the n external particles, where $c_i \in \{1, \ldots, 3\}$ if the i-th particle is a quark or antiquark and $c_i \in \{1, \ldots, 8\}$ if the i-th particle is a gluon. We introduce a set of basis vectors $\{|c_1, \ldots, c_n\rangle\}$ in colour space and write the amplitude

[6] More precisely, the expressions will be valid for all leading order diagrams, even if the corresponding process is loop-induced.

$\mathcal{M}_n^{c_1,\ldots,c_n}$ as

$$\mathcal{M}_n^{c_1,\ldots,c_n} = \langle c_1,\ldots,c_n|\mathcal{M}_n\rangle. \tag{2.30}$$

We begin by studying the emission of a soft gluon from the i-th external (final-state) quark of some arbitrary n-particle amplitude $\mathcal{M}_n^\alpha = \bar{u}(p_i)\widetilde{\mathcal{M}}_n^\alpha$, where $\bar{u}(p_i)$ is the Dirac spinor corresponding to the quark i and α is its SU(3) colour index. The subamplitude $\mathcal{M}_{n+1}^{a,\alpha}$, where a gluon with momentum p_j, colour index a and polarisation vector $\varepsilon_\mu(p_j)$ has been emitted by the quark i, is then given by

$$\mathcal{M}_{n+1}^{\alpha,a} = \mathrm{i}g_s\mu^\varepsilon\bar{u}(p_i)(t^a)_{\alpha\beta}\varepsilon_\mu(p_j)\gamma^\mu\frac{\not{p}_i+\not{p}_j}{s_{ij}}\widetilde{\mathcal{M}}_n^\beta, \tag{2.31}$$

where the colour matrices t^a are the generators of the fundamental representation of SU(3), the factor μ^ε comes from dimensional regularisation and $s_{ij}\equiv(p_i+p_j)^2$.

To write Eq. (2.31) in colour space, we define a colour-charge operator $\mathbf{T}_i$ such that

$$\langle b_1,\ldots,b_i,\ldots,b_n,a|\mathbf{T}_i|\mathcal{M}_n\rangle = \sum_c (t^a)_{b_ic}\mathcal{M}_n^{b_1,\ldots,b_{i-1},c,b_{i+1},\ldots,b_n}, \tag{2.32}$$

i.e. acting on the basis vectors, $\mathbf{T}_i$ is defined by

$$\langle b_1,\ldots,b_i,\ldots,b_n,a|\mathbf{T}_i|c_1,\ldots,c_i,\ldots,c_n\rangle = \delta_{b_1c_1}\ldots(t^a)_{b_ic_i}\ldots\delta_{b_nc_n}, \tag{2.33}$$

with all other matrix elements of $\mathbf{T}_i$ vanishing.

Eq. (2.31) can now be written more economically as

$$|\mathcal{M}_{n+1}\rangle = \mathrm{i}g_s\mu^\varepsilon\bar{u}(p_i)\varepsilon_\mu(p_j)\gamma^\mu\frac{\not{p}_i+\not{p}_j}{s_{ij}}\mathbf{T}_i|\widetilde{\mathcal{M}}_n\rangle. \tag{2.34}$$

In the soft limit, $p_j\to 0$, the expression simplifies to

$$\begin{aligned}|\mathcal{M}_{n+1}\rangle &\overset{p_j\to 0}{\to} \mathrm{i}g_s\mu^\varepsilon\bar{u}(p_i)\varepsilon_\mu(p_j)\gamma^\mu\frac{\not{p}_i}{s_{ij}}\mathbf{T}_i|\widetilde{\mathcal{M}}_n\rangle\\ &= \mathrm{i}g_s\mu^\varepsilon\bar{u}(p_i)\varepsilon_\mu(p_j)\frac{2p_i^\mu}{s_{ij}}\mathbf{T}_i|\widetilde{\mathcal{M}}_n\rangle\\ &= \mathrm{i}g_s\mu^\varepsilon\varepsilon_\mu(p_j)\left[\frac{p_i^\mu}{p_i\cdot p_j}\right]\mathbf{T}_i|\mathcal{M}_n\rangle,\end{aligned} \tag{2.35}$$

where in the second line we first used the anticommutation relation for the gamma matrices and then the Dirac equation $\bar{u}(p_i)\not{p}_i = 0$. In the last line the Dirac spinor has been reabsorbed into the n-particle matrix element. The same formula holds for a soft gluon emission from an initial-state antiquark. An emission from a final-state antiquark or an initial-state quark is described by the same formula after making the replacement

$t^a \to -(t^a)^t$ in the definition of the colour-charge operator in Eq. (2.33).

In contrast to the situation in QED, where soft photon radiation factorises exactly, Eq. (2.35) shows that in QCD the amplitude does only factorise up to *colour correlations* in the soft limit. This is a consequence of the non-Abelian nature of QCD.

The other possible soft configurations can be studied analogously. Because

$$\bar{u}(p_i) = \mathcal{O}\left(\sqrt{E_i}\right) \tag{2.36}$$

as $p_i \to 0$, it follows that a soft quark does only lead to an integrable singularity. An analogous computation as the one in Eq. (2.31) and Eq. (2.35) shows that the emission of a soft gluon from a final- or initial-state gluon is also described by Eq. (2.35) if the colour-charge operator associated with the emission from a gluon is defined as

$$\langle b_1, \ldots, b_i, \ldots, b_n, a|\mathbf{T}_i|c_1, \ldots, c_i, \ldots, c_n\rangle = \delta_{b_1 c_1} \ldots \mathrm{i}f^{b_i a c_i} \ldots \delta_{b_n c_n}. \tag{2.37}$$

To cover all relevant cases, we define the general colour-charge operator by

$$\langle b_1, \ldots, b_i, \ldots, b_n, a|\mathbf{T}_i|c_1, \ldots, c_i, \ldots, c_n\rangle = \delta_{b_1 c_1} \ldots T^a_{b_i c_i} \ldots \delta_{b_n c_n}, \tag{2.38}$$

where $(T^a)_{\alpha\beta} = (t^a)_{\alpha\beta}$ if i is a final-state quark or an initial-state antiquark, $(T^a)_{\alpha\beta} = -(t^a)_{\beta\alpha}$ if i is a final-state antiquark or an initial-state quark and $(T^a)_{bc} = \mathrm{i}f^{bac}$ if i is a final- or initial-state gluon.

Since it cannot be distringuished which external leg the gluon was radiated from, we have to sum over all possibilities to correctly describe the $p_j \to 0$ limit of the full amplitude:

$$\begin{aligned} |\mathcal{M}_{n+1}\rangle &\overset{p_j \to 0}{\to} \mathrm{i}g_s \mu^\varepsilon \varepsilon_\mu(p_j) \sum_{i=1}^{n} \left[\frac{p_i^\mu}{p_i \cdot p_j}\right] \mathbf{T}_i |\mathcal{M}_n\rangle \\ &\equiv \mathrm{i}g_s \mu^\varepsilon \varepsilon_\mu(p_j) \sum_{i=1}^{n} \mathbf{J}^\mu(p_j)|\mathcal{M}_n\rangle, \end{aligned} \tag{2.39}$$

where

$$\mathbf{J}^\mu(p_j) \equiv \sum_{i=1}^{n} \left[\frac{p_i^\mu}{p_i \cdot p_j}\right] \mathbf{T}_i \tag{2.40}$$

is called the *eikonal current*.

An interesting feature of the eikonal current is that it does not depend on the spins of the external particles. In fact, it is a purely classical quantity. This observation can be interpreted as soft (long wave length) radiation not being able to resolve the hard (short distance) quantum process encoded in $\mathcal{M}_n$, and the structure of $\mathbf{J}^\mu$ is thus completely agnostic w.r.t. any underlying quantum field theory description.

2.5.2 Factorisation in the collinear limit

We now discuss the collinear limit of the n-particle amplitude $\mathcal{M}_{a_1,\ldots,a_n}$, where $a_i \in \{q, \bar{q}, g\}$ denotes the flavour of the i-th particle. Without loss of generality, we assume that the first two partons become collinear to each other and that both are final-state particles[7], i.e. $p_1 \to \lambda p_2$, where λ is a real number. More explicitly, the collinear limit can be parametrised as

$$\begin{aligned} p_1^\mu &= z p^\mu + k_\perp^\mu - \frac{k_\perp^2}{z}\frac{n^\mu}{2p\cdot n}, \\ p_2^\mu &= (1-z)p^\mu - k_\perp^\mu - \frac{k_\perp^2}{1-z}\frac{n^\mu}{2p\cdot n}, \end{aligned} \tag{2.41}$$

where

$$s_{12} \equiv 2p_1 \cdot p_2 = -\frac{k_\perp^2}{z(1-z)}, \tag{2.42}$$

p^μ is a light-like vector denoting the collinear direction, n^μ is a light-like vector parameterising how the collinear limit is approached, and the collinear limit itself corresponds to $k_\perp^\mu \to 0$.

The collinear limit is most easily described on the level of squared amplitudes. We start by considering the case $a_1 = q$ and $a_2 = g$. After squaring the amplitude (and summing over spins and colours), inserting Eq. (2.41) and performing the collinear limit, one finds

$$\left|\overline{\mathcal{M}}_{q,g,\ldots,a_n}\right|^2 \overset{k_\perp \to 0}{\to} \frac{2}{s_{12}} 4\pi\mu^{2\varepsilon}\alpha_{\mathrm{S}}\hat{P}_{q\leftarrow q}(z)\left|\overline{\mathcal{M}}_{q,a_3,\ldots,a_n}\right|^2 + \mathcal{O}\left(k_\perp^\mu\right), \tag{2.43}$$

where $\hat{P}_{q\leftarrow q}$ is the finite part of the $q \to qg$ Altarelli-Parisi splitting function in Eq. (2.18):

$$\hat{P}_{q\leftarrow q}(z) = C_F\left[\frac{1+z^2}{1-z} - \varepsilon(1-z)\right]. \tag{2.44}$$

Interchanging a_1 and a_2 simply amounts to $z \to 1-z$, and thus the corresponding factorisation formula is identical to Eq. (2.43) except for the replacement

$$\hat{P}_{q\leftarrow q}(z) \to \hat{P}_{g\leftarrow q}(z) = C_F\left[\frac{1+(1-z)^2}{z} - \varepsilon z\right]. \tag{2.45}$$

Similarly, factorisation formulae can also be obtained for the remaining collinear limits. If a_1 and a_2 are a quark-antiquark pair (corresponding to a $g \to q\bar{q}$ splitting) or both gluons (corresponding to a $g \to gg$ splitting), a slight complication arises due to spin correlations in the factorised matrix element. To obtain a unified notation, we denote the spin indices

[7] The formulae for the situation in which one final- and one initial-state parton become collinear can be obtained by crossing.

of the (final-state) partons by $s_1, s_2, \ldots, s_n$ in the following, where $s_i = \pm 1$ if the i-th parton is a (anti) quark and s_i is a Lorentz index if the i-th parton is a gluon. We can then write the generalisation of Eq. (2.43) as

$$\left|\overline{\mathcal{M}}_{a_1,\ldots,a_n}\right|^2 \overset{k_\perp \to 0}{\to} \frac{2}{s_{12}} 4\pi\mu^{2\varepsilon}\alpha_{\mathrm{S}} \hat{P}^{s_1 s_1'}_{a_1 a_2}(z, k_\perp) \mathcal{T}^{s_1 s_1'}_{a_1+a_2, a_3, \ldots, a_n} + \mathcal{O}\left(k_\perp^\mu\right), \tag{2.46}$$

where the spin-polarisation tensor $\mathcal{T}^{s_1 s_1'}_{a, a_3, \ldots, a_n}$ denotes the squared $(n-1)$-parton amplitude with flavours $a, a_3, \ldots, a_n$ summed over all spins except s_1 and summed over all colours,

$$\mathcal{T}^{s_1 s_1'}_{a, a_3, \ldots, a_n} \equiv \sum_{\text{spins} \neq s_1, s_1'} \sum_{\text{colours}} \mathcal{M}^{s_1, s_2, \ldots, s_n}_{a, a_3, \ldots, a_n} \left[\mathcal{M}^{s_1', s_2, \ldots, s_n}_{a, a_3, \ldots, a_n}\right]^\dagger. \tag{2.47}$$

The flavour $a_1 + a_2$ is obtained according to $g + a = a + g = a$ and $q + \bar{q} = g$. The spin-dependent splitting functions $\hat{P}^{s_1 s_1'}_{a_1 a_2}$ are given by

$$\hat{P}^{ss'}_{qg}(z) = \delta_{ss'} C_F \left[\frac{1+z^2}{1-z} - \varepsilon(1-z)\right] \tag{2.48}$$

$$\hat{P}^{ss'}_{gq}(z) = \delta_{ss'} C_F \left[\frac{1+(1-z)^2}{z} - \varepsilon z\right] \tag{2.49}$$

$$\hat{P}^{\mu\nu}_{q\bar{q}}(z, k_\perp) = \frac{1}{2}\left[-g^{\mu\nu} + 4z(1-z)\frac{k_\perp^\mu k_\perp^\nu}{k_\perp^2}\right] \tag{2.50}$$

$$\hat{P}^{\mu\nu}_{gg}(z, k_\perp) = 2C_A \left[-g^{\mu\nu}\left(\frac{z}{1-z} + \frac{1-z}{z}\right) - 2(1-\varepsilon)z(1-z)\frac{k_\perp^\mu k_\perp^\nu}{k_\perp^2}\right]. \tag{2.51}$$

2.6 Jet algorithms and infrared safety

In QED, final-state elementary particles such as photons and electrons can be detected directly in an experiment. However, due to confinement this is not possible in QCD: the gluons and quarks in the final state will hadronise until only colourless particles remain. To allow for a comparison of theoretical computations with experimental data, collision events are usually characterised by the number and momenta of *jets* in the final state. At parton level, final-state gluons and quarks which are "close enough" to each other are grouped together into a jet. The details of this grouping procedure are specified by a jet algorithm; see Refs. [65–68] for the commonly used ones. At the detector level, analogous algorithms are used to group measured energy deposits together. The usual assumption is that jets at parton level and jets at detector level are equivalent. The precise relation between parton-level and detector-level jets involves non-perturbative physics and can be studied using phenomenological hadronisation models (see for example Ref. [69]). Usually, hadronisation effects are small[8] and can be partially taken into account by correction factors.

[8] Though we will encounter a counterexample in Section 5.1.4.

As outlined above, infrared singularities cancel order-by-order in perturbation theory between real and virtual contributions for inclusive observables. For less inclusive observables, this cancellation is more subtle and constrains the classes of observables which can be sensibly predicted in perturbation theory to so-called *infrared-safe observables*. A well-known example for a non-IR safe observable from QED would be the production cross section of some final-state particle without any additional photon radiation: this requirement would remove all real contributions from the theoretical prediction, spoiling the cancellation of IR poles from the virtual contributions. In practice, such an observable however cannot be measured, as it would require the identification of arbitrarily soft photons in the detector.

An example in QCD would be the cross section for the production of some heavy particle F, with momentum p_1, with no accompanying jets inside a cone of opening angle θ_0 around p_1. A jet very close to (but outside of) the cone might move inside the cone by the emission of a soft or collinear parton, and the corresponding event would then be cut away. This would remove part of the IR divergent cross section from the real-emission contributions and thus spoil the cancellation of IR singularities.

A sufficient criterion for an observable to be infrared safe is due to Sterman and Weinberg [70] and is formulated in terms of the measurement functions introduced in Eq. (2.25). The idea is that whenever a parton becomes soft or two partons become collinear to each other, the n-particle measurement function should smoothly approach the $(n-1)$-particle measurement function, in which the soft parton has been removed or the two collinear partons have been combined:

$$\mathcal{J}^{(n)}(p_1, p_2, \ldots, p_n) \to \mathcal{J}^{(n-1)}(p_2, \ldots, p_n) \quad \text{if} \quad E_1 \to 0, \tag{2.52}$$

$$\mathcal{J}^{(n)}(p_1, p_2, \ldots, p_n) \to \mathcal{J}^{(n-1)}(p_1 + p_2, \ldots, p_n) \quad \text{if} \quad p_1 \to \lambda p_2, \lambda \in \mathbb{R}. \tag{2.53}$$

3 Perturbative computations

In this chapter we discuss subtraction methods for NLO and NNLO computations. We start with an overview of existing NLO subtraction techniques in Section 3.1. After summarising some of the established options for subtraction at NNLO in Section 3.2, we focus on the q_{T} subtraction method, which underlies all phenomenological results contained in this thesis. As q_{T} subtraction is based on q_{T} resummation, we first review transverse-momentum resummation in Section 3.3 before giving a formal proof of the q_{T} subtraction master formula in Section 3.4.

3.1 Next-to-leading order

For the sake of clarity, we restrict the discussion in this section to the case of e^+e^- collisions. The generalisation to hadron-hadron collisions requires a convolution over the PDFs, see Eq. (2.15). With hadronic initial states, additional initial-state IR singularities appear, which cancel against the collinear counterterm coming from the PDFs.

Computing the next-to-leading order corrections to any observable requires the computation of both real (involving diagrams with an additional QCD emission) and virtual (involving Born-level diagrams with an additional closed loop) corrections:

$$\sigma^{\mathrm{NLO}} = \int_n \mathrm{d}\sigma^{\mathrm{LO}} + \int_{n+1} \mathrm{d}\sigma^{\mathrm{R}} + \int_n \mathrm{d}\sigma^{\mathrm{V}}, \tag{3.1}$$

where $\mathrm{d}\sigma^{\mathrm{LO}}$ is the leading order Born cross section, $\mathrm{d}\sigma^{\mathrm{R}}$ is the real correction and $\mathrm{d}\sigma^{\mathrm{V}}$ is the virtual correction. Written out, the integrands are given by

$$\mathrm{d}\sigma^{\mathrm{LO}} = \mathrm{d}\Phi^{(n)} \left|\mathcal{M}_n^{(0)}\right|^2 \mathcal{J}^{(n)}(\{p_i\}), \tag{3.2}$$

$$\mathrm{d}\sigma^{\mathrm{R}} = \mathrm{d}\Phi^{(n+1)} \left|\mathcal{M}_{n+1}^{(0)}\right|^2 \mathcal{J}^{(n+1)}(\{p_i\}), \tag{3.3}$$

$$\mathrm{d}\sigma^{\mathrm{V}} = \mathrm{d}\Phi^{(n)} \left[\mathcal{M}_n^{(1)}\mathcal{M}_n^{(0)\dagger} + \mathcal{M}_n^{(1)\dagger}\mathcal{M}_n^{(0)}\right] \mathcal{J}^{(n)}(\{p_i\}), \tag{3.4}$$

where the phase-space measures are defined in Eqs. (2.26) and (2.27). $\mathcal{M}_n^{(m)}$ denotes the relevant m-loop matrix element with n partons in the final state.

While the sum of real and virtual contributions in Eq. (3.1) is guaranteed to be finite by the KLN theorem as long as the observable encoded in $\mathcal{J}$ is infrared safe in the sense defined in Section 2.6, they are separately infrared divergent: the virtual correction contains

explicit poles in the regularisation parameter, and the real correction is divergent when integrated over the phase space of the additional final-state parton, due to the soft and collinear QCD singularities discussed in Section 2.4. If the phase-space integration over the real emission is carried out analytically, it yields exactly the same poles as the virtual contribution, but with an opposite sign, leading to a finite cross section.

However, in the presence of non-trivial selection cuts, performing the real phase-space integral becomes increasingly cumbersome or even impossible. On the other hand, a straight forward numerical implementation of the integration is also not possible, as it would simply result in a divergent integral. In the past, different methods have been proposed to regulate QCD singularities in the real contribution. These methods can be classified into slicing [71, 72] and subtraction [8–10, 73, 74] methods. They can be used to regulate the phase-space integral in a process-independent way such that a numerical integration leads to a finite result. The divergent part of the phase-space integral, which due to the universality of QCD IR singularities is process independent, has to be computed only once and is used to cancel the explicit IR poles in the virtual correction contribution.

In local subtraction schemes, the NLO cross section in Eq. (3.1) is rewritten as

$$\sigma^{\mathrm{NLO}} = \int_n \mathrm{d}\sigma^{\mathrm{LO}} + \int_{n+1} \left[\mathrm{d}\sigma^{\mathrm{R}} - \mathrm{d}\sigma^{\mathrm{CT}}\right] + \int_n \left[\mathrm{d}\sigma^{\mathrm{V}} + \int_1 \mathrm{d}\sigma^{\mathrm{CT}}\right]_{\varepsilon=0}, \tag{3.5}$$

where the $\mathrm{d}\sigma^{\mathrm{CT}}$ denotes (a set of) local counterterms, $\int_1$ is the integration over the one-emission phase space and ε is the regularisation parameter, for example from dimensional regularisation. Both the real cross section $\mathrm{d}\sigma^{\mathrm{R}}$ and the corresponding counterterms in $\mathrm{d}\sigma^{\mathrm{CT}}$ can be computed in $d = 4$ dimensions.

More precisely, the idea is to supplement the real phase-space weight with local counterterms subtracting all non-integrable singularities. Schematically, this can be expressed as

$$\mathrm{d}\sigma^{\mathrm{R}} \to \mathrm{d}\sigma^{\mathrm{R}} - \sum_{ij} \mathrm{d}\sigma_{ij}^{\mathrm{CT}}, \tag{3.6}$$

where the $\mathrm{d}\sigma_{ij}^{\mathrm{CT}}$ denote local counterterms regulating all soft ($E_j \to 0$) and collinear ($p_i \to \lambda p_j$ with $\lambda \in \mathbb{R}$) singularities in $\mathrm{d}\sigma^{\mathrm{R}}$. The counterterms should be chosen in a way which allows the integration over the phase space of the additional emission to be performed in a process-independent way, i.e. they should be of the form

$$\mathrm{d}\sigma_{ij}^{\mathrm{CT}}(\{p_k\}) = \mathrm{d}\Phi^{(n+1)}\, \mathbf{V}_{ij}(\{\tilde{p}_k\}) \otimes \left|\mathcal{M}_n^{(0)}\right|^2 (\{\tilde{p}_k\})\, \mathcal{J}^{(n)}(\{\tilde{p}_k\}), \tag{3.7}$$

where $\mathrm{d}\Phi^{(n+1)}$ is the real phase-space measure, $\{p_k\}$ are the original particle momenta, $\{\tilde{p}_k\}$ are Born-level momenta obtained by some mapping from $\{p_k\}$, $\mathcal{M}_n^{(0)}$ is the leading order Born matrix element[1] and $\mathcal{J}^{(n)}(\{\tilde{p}_k\})$ is the n-particle measurement function. Due

[1] From the discussion in Section 2.4 it is clear that what is needed here are actually the colour and spin projections of the Born matrix element to correctly account for colour and spin correlations in the soft

to the requirement of IR safety, $\mathcal{J}^{(n+1)}$ will smoothly approach $\mathcal{J}^{(n)}$ in the singular limit, and therefore the cancellation works independently of the observable.

The mapping of the original momenta $\{p_k\}$ onto the modified momenta $\{\tilde{p}_k\}$ takes the form

$$\{p_1, \ldots, p_{n+1}\} \leftrightarrow \{\tilde{p}_1, \ldots, \tilde{p}_n, p_i + p_j\}. \tag{3.8}$$

It can be chosen in such a way that the (n+1)-particle phase space $\mathrm{d}\Phi^{(n+1)}$ exactly factorises into an n-particle (Born-level) phase space and a one-particle phase space corresponding to the real emission:

$$\mathrm{d}\Phi^{(n+1)}(\{p_k\}) = \mathrm{d}\Phi^{(n)}(\{\tilde{p}_k\})\, \mathrm{d}\varphi_{\{\tilde{p}_k\}}(p_i + p_j), \tag{3.9}$$

where $\mathrm{d}\varphi_{\{\tilde{p}_k\}}$ denotes the one-particle phase space which, as long as $\tilde{p}_1, \ldots, \tilde{p}_n$ are fixed, only depends on $(p_i + p_j)$.

Using this, the (divergent) integration over the one-particle emission phase space can be (up to spin and colour correlations) completely factorised off:

$$\begin{aligned}\sum_{ij} \int_{n+1} \mathrm{d}\sigma_{ij}^{\mathrm{CT}} &= \int_n \mathrm{d}\Phi^{(n)}(\{\tilde{p}_k\}) \left|\mathcal{M}^{(0)}\right|^2 (\{\tilde{p}_k\})\, \mathcal{J}^{(n)}(\{\tilde{p}_k\}) \\ &\qquad \otimes \sum_{ij} \int_1 \mathrm{d}\varphi_{\{\tilde{p}_k\}}(p_i + p_j)\, \mathbf{V}_{ij} \\ &= \int_m \mathrm{d}\sigma_{ij}^{\mathrm{LO}} \otimes \mathbf{I}(\{\tilde{p}_k\}),\end{aligned} \tag{3.10}$$

where

$$\mathbf{I}(\{\tilde{p}_k\}) = \sum_{ij} \int_1 \mathrm{d}\varphi_{\{\tilde{p}_k\}}(p_i + p_j)\, \mathbf{V}_{ij} \tag{3.11}$$

denotes the integrated subtraction terms. The integrals in Eq. (3.11) are IR divergent and have to be performed analytically. They yield exactly the poles needed to cancel the corresponding IR poles in the virtual contribution, rendering the total result IR finite.

The Catani-Seymour (CS) dipole subtraction formalism [9, 10] provides explicit and process-independent functions $\mathbf{V}_{ij}$ covering all possible soft and collinear singularities in terms of dipoles $\mathcal{D}_{ij,k}$. The dipole terms depend, besides the partons i and j directly involved in the soft or collinear limit, on an additional parton k (the spectator). The spectator is used to make the mapping in Eq. (3.8) momentum preserving. As all the integrated dipoles are known and process independent, and the singularity structure of the real-emission amplitude is completely determined by its QCD flavour structure, the CS dipole formalism allows for a completely process-independent implementation of the NLO

and collinear limits respectively. The symbol $\otimes$ denotes the corresponding contractions.

subtraction formalism. Combined with numerical codes to compute one-loop amplitudes, this makes it possible to provide tools which are able to compute NLO QCD corrections to arbitrary SM processes in a fully automated way.

It should however be noted that CS subtraction is not the only viable subtraction procedure at NLO. A completely independent formulation of the subtraction technique, FKS subtraction [74], is based on a decomposition of the real phase space into different sectors in which all but one soft or collinear IR singularity is damped out. The remaining singularity can then be subtracted in a process-independent way and in the end the analytically integrated subtraction terms can be added back to cancel the IR poles in the virtual contribution.

Nowadays, several fully automated tools are available which implement either CS subtraction (Sherpa [14, 75, 76], Munich [39, 77, 78] (see also Section 4.2.1.)) or FKS subtraction (MadGraph5_aMC@NLO [12, 79]).

3.2 Next-to-next-to-leading order

At NNLO, the problem of cancelling the infrared singularities becomes significantly more involved compared to the situation at NLO. At $\mathcal{O}(\alpha_S^2)$, three separately divergent types of contributions enter the cross section: double-real (RR), real-virtual (RV) and double-virtual (VV) contributions. The double-real contribution involves two additional QCD partons in the final state compared to the Born process, the real-virtual contribution involves one additional QCD parton and one additional closed loop compared to the Born process, and the double-virtual contribution consists of the two-loop corrections to the Born process:

$$\sigma^{\mathrm{NNLO}} = \sigma^{\mathrm{NLO}} + \int_{n+2} \mathrm{d}\sigma^{\mathrm{RR}} + \int_{n+1} \mathrm{d}\sigma^{\mathrm{RV}} + \int_{n} \mathrm{d}\sigma^{\mathrm{VV}}. \tag{3.12}$$

Written out, the integrands read

$$\mathrm{d}\sigma^{\mathrm{RR}} = \mathrm{d}\varphi^{(n+2)} \left|\mathcal{M}_{n+2}^{(0)}\right|^2 \mathcal{J}^{(n+2)}(\{p_i\}), \tag{3.13}$$

$$\mathrm{d}\sigma^{\mathrm{RV}} = \mathrm{d}\varphi^{(n+1)} \left[\mathcal{M}_{n+1}^{(1)}\mathcal{M}_{n+1}^{(0)\dagger} + \mathcal{M}_{n+1}^{(1)\dagger}\mathcal{M}_{n+1}^{(0)}\right] \mathcal{J}^{(n+1)}(\{p_i\}), \tag{3.14}$$

$$\mathrm{d}\sigma^{\mathrm{VV}} = \mathrm{d}\varphi^{(n)} \left[\left|\mathcal{M}_{n}^{(1)}\right|^2 + \mathcal{M}_{n}^{(2)}\mathcal{M}_{n}^{(0)\dagger} + \mathcal{M}_{n}^{(2)\dagger}\mathcal{M}_{n}^{(0)}\right] \mathcal{J}^{(n)}(\{p_i\}). \tag{3.15}$$

Both the double-real and the real-virtual amplitudes are IR divergent when integrated over the phase space of the additional emissions and both the real-virtual and the double-virtual amplitudes exhibit explicit poles in the regularisation parameter. Again, all explicit and implicit singularities have to cancel for every infrared-safe observable. In analogy to NLO, a subtraction has to be performed to compute NNLO cross sections numerically and fully differentially.

Examples of general NNLO subtraction schemes are antenna subtraction [15] and Strip-

PER [16,17]. Additional subtraction methods are COLORFUL subtraction [80,81], which so far has been established in the case of e^+e^- collisions, and N-jettiness subtraction [18,82], which can currently be used for processes with up to one final-state jet at Born level.

Both antenna subtraction and COLORFUL subtraction are very similar in spirit to the dipole subtraction method at NLO in the sense that they construct (in the case of antenna subtraction almost) local counterterms for each possible IR divergence. These counterterms can be analytically integrated over the single or double real-emission phase space, yielding the poles needed to cancel the corresponding poles in the real-virtual and double-virtual amplitudes. Antenna subtraction has been used to compute NNLO QCD corrections to three-jet production in e^+e^- collisions in Refs. [83–85], to dijet production in Ref. [26], to Higgs+jet production in Ref. [29] and to Z+jet production in Ref. [36]. It is currently being extended to also deal with computations in massive QCD, and first results for $t\bar{t}$ production have appeared recently in Refs. [30, 35]. Colourful subtraction has been applied to compute the $h \to b\bar{b}$ decay rate at NNLO in Ref. [86].

STRIPPER is more similar to FKS subtraction as it decomposes the real phase spaces into sectors such that each real-emission singularity is isolated. It then exploits a suitable parameterisation in each sector to numerically perform the phase-space integration, yielding the coefficients of the Laurent series one would have obtained by performing the phase-space integrals analytically in dimensional regularisation. The advantage of this approach is that it avoids the need to perform cumbersome analytical integrations to obtain the finite parts of the integrated subtraction terms. STRIPPER has been used in the computation of NNLO corrections to Higgs+jet production in Ref. [23] and $t\bar{t}$ production in Refs. [24, 31].

The latest addition to the list of NNLO subtraction schemes, N-jettiness subtraction, is in some sense an extension of q_{T} subtraction. In its formulation as a pure slicing method[2], it differs from q_{T} subtraction by its use of a different resolution variable – the N-jettiness of the final state instead of its transverse momentum – for the slicing parameter, which allows the method to be used also for processes with jets in the Born-level final state. N-jettiness subtraction has so far been applied to compute the NNLO corrections to W+jet production in Ref. [33] and Higgs+jet production in Ref. [34].

When restricting the class of processes to the production of a non-QCD final state, for example a Higgs boson or a pair of vector bosons, the issue of IR singularities simplifies substantially. The reason is that the first emission of an additional QCD parton can only come from the initial-state particles, and hence the singularity structure of the process simplifies. For this restricted – but highly relevant – subclass of processes, alternative subtraction schemes are available. One prominent example is q_{T} subtraction [38], which has been used for all computations presented in this thesis. q_{T} subtraction has its origin in q_{T} resummation, that is in resumming the logarithmically-enhanced contributions to transverse-momentum spectra to all orders. In the following, we will briefly review the q_{T} resummation formalism (closely following the discussion in Ref. [87]) and then give a

[2]Both q_{T} subtraction and N-jettiness subtraction can in principle be formulated more locally, either by introducing additional slicing parameters or by performing the non-local subtraction more differentially in the Born kinematics.

formal derivation of the q_T subtraction master formula.

3.3 q_T resummation

In multiscale problems, the convergence of the perturbative series in Eq. (2.23) might be spoiled by the presence of large logarithms multiplying the expansion parameter – the strong coupling constant α_S in the case of QCD. To obtain a reliable prediction in these situations, the large logarithms need to be resummed to all orders. An example for such a situation is the computation of transverse-momentum spectra of a final-state system F, where, in the low transverse-momentum region, logarithms of the form

$$L = \log \frac{q_\mathrm{T}^2}{Q^2} \tag{3.16}$$

will appear. Here and in the following, $q_\mathrm{T} \equiv q_\mathrm{T}^\mathrm{F}$ is the total transverse momentum of the final-state system F, and Q denotes the *resummation scale*. Q should be of the same order as the hard scale of the process. In fact, for all purposes of this thesis – with the exception of Section 5.4, where we study resummation effects – we can identify Q with the invariant mass of the final-state system[3]:

$$Q \equiv M_F. \tag{3.17}$$

Furthermore, we will only consider quark-induced production processes of non-QCD final states, i.e. processes which are of the form $q\bar{q} \to \mathrm{F}$ at Born level, where F is a system of particles which are not strongly interacting. In the Standard Model, F can be an arbitrary combination of leptons, neutrinos, Higgs bosons and electroweak vector bosons. Gluon-induced processes, $gg \to \mathrm{F}$, can be handled with the same formalism. They are slightly more complicated as they involve additional spin correlations; see Ref. [88] for a detailed discussion.

We work on the level of the partonic cross section $\mathrm{d}\sigma_{ab\to\mathrm{F}}$, which has to be convoluted with the PDFs to obtain the final result. The first step in the resummation of the large logarithms in Eq. (3.16) is to split the transverse-momentum spectrum into a *resummed* and a *finite* component:

$$\frac{\mathrm{d}\sigma_{ab\to\mathrm{F}}}{\mathrm{d}q_\mathrm{T}^2} = \frac{\mathrm{d}\sigma_{ab\to\mathrm{F}}^{(\mathrm{res.})}}{\mathrm{d}q_\mathrm{T}^2} + \frac{\mathrm{d}\sigma_{ab\to\mathrm{F}}^{(\mathrm{fin.})}}{\mathrm{d}q_\mathrm{T}^2}. \tag{3.18}$$

The resummed component $\mathrm{d}\sigma_{ab\to\mathrm{F}}^{(\mathrm{res.})}/\mathrm{d}q_\mathrm{T}^2$ contains all terms enhanced by large logarithms, while in the finite component $\mathrm{d}\sigma_{ab\to\mathrm{F}}^{(\mathrm{fin.})}/\mathrm{d}q_\mathrm{T}^2$ large logarithms are absent, and it can thus

[3] This is because Q will exactly cancel out order-by-order from the fixed-order formulaes obtained from q_T resummation and used in q_T subtraction.

be computed using standard (fixed-order) perturbation theory. In practice, $\mathrm{d}\sigma^{(\mathrm{res.})}_{ab\to\mathrm{F}}/\mathrm{d}q_{\mathrm{T}}^2$ is expanded to a certain *logarithmic accuracy* (l.a.), that is to leading log (LL), next-to-leading log (NLL), next-to-next-to-leading log (NNLL) accuracy and so on, while $\mathrm{d}\sigma^{(\mathrm{fin.})}_{ab\to\mathrm{F}}/\mathrm{d}q_{\mathrm{T}}^2$ is expanded to a certain fixed order (f.o.), i.e. to LO, NLO, NNLO and so on:

$$\frac{\mathrm{d}\sigma_{ab\to\mathrm{F}}}{\mathrm{d}q_{\mathrm{T}}^2} \to \left[\frac{\mathrm{d}\sigma_{ab\to\mathrm{F}}}{\mathrm{d}q_{\mathrm{T}}^2}\right]_{\text{l.a.+f.o.}} = \left[\frac{\mathrm{d}\sigma^{(\mathrm{res.})}_{ab\to\mathrm{F}}}{\mathrm{d}q_{\mathrm{T}}^2}\right]_{\text{l.a.}} + \left[\frac{\mathrm{d}\sigma^{(\mathrm{fin.})}_{ab\to\mathrm{F}}}{\mathrm{d}q_{\mathrm{T}}^2}\right]_{\text{f.o.}}. \tag{3.19}$$

The low transverse-momentum region corresponds to the emission of soft and collinear partons, and the resummation procedure is based on the factorisation of the cross section in these limits. On the matrix element level, factorisation always occurs in the infrared limit, but to achieve factorisation of the phase space, the resummed component has to be computed in impact-parameter space (b-space), which is obtained by a Fourier transformation in q_{T}. After performing the integral over the azimuth, the transformation can be written as a Bessel transform,

$$\frac{\mathrm{d}\sigma^{(\mathrm{res.})}_{ab\to\mathrm{F}}}{\mathrm{d}q_{\mathrm{T}}^2} = \frac{M_F^2}{\hat{s}} \int_0^\infty \mathrm{d}b\, \frac{b}{2}\, J_0(bq_{\mathrm{T}})\, \mathcal{W}^F_{ab}(y, b, M_F^2, \hat{s}, \mu_R^2, \mu_F^2), \tag{3.20}$$

where $\hat{s}$ and y are the partonic centre-of-mass energy and rapidity, and J_0 is the zeroth-order Bessel function. $\mathrm{d}\sigma^{(\mathrm{res.})}_{ab\to\mathrm{F}}/\mathrm{d}q_{\mathrm{T}}^2$ and thus $\mathcal{W}^F_{ab}$ will also depend on additional phase-space variables parametrising the system F. These are however not affected by the resummation formalism and their presence is implicitly understood in the following.

In b-space, the large logarithms in Eq. (3.16) are transformed into logarithms of the form

$$L = \log \frac{Q^2 b^2}{b_0^2}, \tag{3.21}$$

where $b_0 = 2\exp(-\gamma_E)$. These logarithms become large when $b \to \infty$, which corresponds to $q_{\mathrm{T}} \to 0$ in q_{T}-space. To avoid the singularity at $b \to 0$, the argument of L in Eq. (3.21) is typically replaced by $Q^2b^2/b_0^2 + 1$, i.e.

$$L \to \widetilde{L} = \log\left(\frac{Q^2 b^2}{b_0^2} + 1\right), \tag{3.22}$$

which does not affect the large b (small q_{T}) behaviour, but leads to a damping of the resummed component in the large q_{T} region, where the cross section should be computed in fixed-order perturbation theory.

In the following, it is more convenient to work in Mellin space (N-space). The Mellin transform f_N of some function f in the variable z is defined as

$$f_N = \int_0^1 \mathrm{d}z\, z^{N-1}\, f(z). \tag{3.23}$$

The Mellin transform turns convolutions in z-space into products in N-space:

$$[f \otimes g]_N = \int_0^1 \mathrm{d}z\, z^{N-1} \left[\int_z^1 \frac{\mathrm{d}x}{x} f\left(\frac{z}{x}\right) g(x) \right] = f_N\, g_N \tag{3.24}$$

for sufficiently well-behaved functions (and distributions) f and g.

To keep the full rapidity dependence at Born level, double Mellin moments (N_1, N_2) corresponding to (z_1, z_2) have to be used. z_1 and z_2 retain the information about the Born-level rapidity y and are defined as

$$z_1 = \exp(+y)\frac{M_F}{\sqrt{\hat{s}}}, \tag{3.25}$$

$$z_2 = \exp(-y)\frac{M_F}{\sqrt{\hat{s}}}. \tag{3.26}$$

The double Mellin transform of $\mathcal{W}_{ab}^{\mathrm{F}}$,

$$\begin{aligned}
&\mathcal{W}_{ab}^{\mathrm{F},(N_1,N_2)}(b, M_F^2, \mu_R^2, \mu_F^2) \\
&\quad = \int_0^1 \mathrm{d}z_1\, z_1^{N_1-1} \int_0^1 \mathrm{d}z_2\, z_2^{N_2-1}\, \mathcal{W}^F(y = \frac{1}{2}\log\frac{z_1}{z_2}, b, M_F^2, \hat{s} = M_F^2/(z_1 z_2), \mu_R^2, \mu_F^2),
\end{aligned} \tag{3.27}$$

can be factorised as

$$\begin{aligned}
\mathcal{W}_{ab}^{\mathrm{F},(N_1,N_2)}(b, M_F^2, \mu_R^2, \mu_F^2) = \sum_q \sigma_{\mathrm{q\bar{q}}}^{\mathrm{F}(0)} \times \mathcal{H}_{q\bar{q}\leftarrow ab}^{\mathrm{F},(N_1,N_2)}(M_F^2, \mu_R^2, \mu_F^2) \\
\times \exp\{\mathcal{G}^{(N_1,N_2)}(\widetilde{L}, M_F^2, \mu_R^2)\},
\end{aligned} \tag{3.28}$$

where $\sigma_{q\bar{q}}^{\mathrm{F}(0)}$ is the leading order cross section.

The hard-collinear function $\mathcal{H}_{q\bar{q}\leftarrow ab}^{\mathrm{F}}$ in Eq. (3.28) does not depend on b and thus does not contain any large logarithms. It can be expanded in α_{S} and computed perturbatively:

$$\mathcal{H}_{q\bar{q}\leftarrow ab}^{\mathrm{F}} = \delta_{aq}\delta_{\bar{q}b} + \frac{\alpha_{\mathrm{S}}}{2\pi}\mathcal{H}_{q\bar{q}\leftarrow ab}^{\mathrm{F}(1)} + \left(\frac{\alpha_{\mathrm{S}}}{2\pi}\right)^2 \mathcal{H}_{q\bar{q}\leftarrow ab}^{\mathrm{F}(2)} + \dots. \tag{3.29}$$

$\mathcal{H}_{q\bar{q}\leftarrow ab}^{\mathrm{F}}$ depends on the hard process and in particular its perturbative coefficients will depend on the loop-corrections to the underlying Born process.

The function $\mathcal{G}$ on the other hand collects the large logarithms $\widetilde{L}$, but does not depend on the hard process.

$\mathcal{G}$ cannot be naively expanded in α_{S}. It can, however, be systematically expanded to a given logarithmic accuracy:

$$\mathcal{G}(\widetilde{L}, M_F^2, \mu_R^2) = \widetilde{L} g^{(1)}(\alpha_S \widetilde{L}) + g^{(2)}(\alpha_S \widetilde{L}) + \left(\frac{\alpha_S}{\pi}\right) g^{(3)}(\alpha_S \widetilde{L}) + \dots, \tag{3.30}$$

where the functions $g^{(n)}$ satisfy $g^{(n)}(0) = 0$. Keeping only $g^{(1)}$ would result in a leading-log resummation, keeping $g^{(2)}$ resums the next-to-leading logarithms, $g^{(3)}$ the next-to-next-to-leading logarithms and so on. As $\exp\{\mathcal{G}\}$ is multiplied by $\mathcal{H}^{\mathrm{F}}$ in Eq. (3.28), NLL logarithmic accuracy on the level of the cross section in addition requires that the expansion of $\mathcal{H}^{\mathrm{F}}$ in Eq. (3.29) retains the NLO coefficient $\mathcal{H}^{\mathrm{F}(1)}$, and NNLL logarithmic accuracy requires also the NNLO coefficient $\mathcal{H}^{\mathrm{F}(2)}$.

$\mathcal{G}$ can be rewritten in terms of the universal functions $A(\alpha_{\mathrm{S}})$ and $\widetilde{B}(\alpha_{\mathrm{S}})$ as

$$\mathcal{G}(\widetilde{L}, M_F^2, \mu_R^2) = -\int_{b^2/b_0^2}^{M_F^2} \frac{\mathrm{d}q^2}{q^2} \left[A(\alpha_{\mathrm{S}}(q^2)) \log \frac{M_F^2}{q^2} + \widetilde{B}(\alpha_{\mathrm{S}}(q^2)) \right], \tag{3.31}$$

where both A and $\widetilde{B}$ are perturbative functions:

$$A(\alpha_{\mathrm{S}}) = \frac{\alpha_{\mathrm{S}}}{\pi} A^{(1)} + \left(\frac{\alpha_{\mathrm{S}}}{\pi}\right)^2 A^{(2)} + \sum_{n=3}^{\infty} \left(\frac{\alpha_{\mathrm{S}}}{\pi}\right)^n A^{(n)}, \tag{3.32}$$

$$\widetilde{B}(\alpha_{\mathrm{S}}) = \frac{\alpha_{\mathrm{S}}}{\pi} \widetilde{B}^{(1)} + \left(\frac{\alpha_{\mathrm{S}}}{\pi}\right)^2 \widetilde{B}^{(2)} + \sum_{n=3}^{\infty} \left(\frac{\alpha_{\mathrm{S}}}{\pi}\right)^n \widetilde{B}^{(n)}. \tag{3.33}$$

By explicitly evaluating the integral in Eq. (3.31) and comparing the result with Eq. (3.30), the relations between the $g^{(n)}$ and the $A^{(n)}$ and $\widetilde{B}^{(n)}$ can be obtained order-by-order [87].

The perturbative function $\mathcal{H}^{\mathrm{F}}$ can be further factorised into the *hard function* H^{F} and one *collinear function* C for each leg:

$$\mathcal{H}^{\mathrm{F},(N_1,N_2)}_{q\bar{q}\leftarrow ab} = \sum_{a_1,b_1} C^{N_1}_{qa_1} \times C^{N_2}_{\bar{q}b_1} \times U^{N_1}_{a_1 a} \times U^{N_2}_{b_1 b} \times H^{\mathrm{F}}, \tag{3.34}$$

where

$$U^N_{ab} = \exp\left\{ \int_{\mu_F^2}^{M_F^2} \frac{\mathrm{d}q^2}{q^2} \gamma^N_{ab}(\alpha_{\mathrm{S}}(q^2)) \right\} \tag{3.35}$$

restores the correct factorisation scale dependence. The γ_{ab} are the parton anomalous dimensions, i.e. the Mellin transforms of the Altarelli-Parisi splitting functions P_{ab}:

$$\gamma_{ab,\,N} = \int_0^1 \mathrm{d}z\, z^{N-1} P_{ab}(z). \tag{3.36}$$

Both the collinear and the hard function are perturbative functions and can be expanded

in α_S,

$$H^F = 1 + \left(\frac{\alpha_S}{2\pi}\right) H^{F(1)} + \left(\frac{\alpha_S}{2\pi}\right)^2 H^{F(2)} + \sum_{n=3}^{\infty} \left(\frac{\alpha_S}{2\pi}\right)^n H^{F(n)}, \tag{3.37}$$

$$C_{ab} = 1 + \left(\frac{\alpha_S}{2\pi}\right) C_{ab}^{(1)} + \left(\frac{\alpha_S}{2\pi}\right)^2 C_{ab}^{(2)} + \sum_{n=3}^{\infty} \left(\frac{\alpha_S}{2\pi}\right)^n C_{ab}^{(n)}. \tag{3.38}$$

The factorisation in Eq. (3.34) is not unique; it depends on the so-called *resummation scheme* [87]. Only after the resummation scheme has been specified, the individual factors H^F and C are unambiguously defined. The traditional choice is to fix the resummation scheme by the condition $H^F = 1$, which in particular implies that all process-dependent information is encoded in the collinear functions. An alternative is the so-called *hard scheme*. The hard scheme is defined by requiring that all constant terms in N-space – which correspond to the $\delta(1 - z_1 z_2)$ terms in z-space – are contained in H^F. The only process-dependent information entering $\mathcal{H}^F$ are the finite parts of the loop corrections to the Born process, and these necessarily come with a factor of $\delta(1 - z_1 z_2)$. Together, this implies that in the hard scheme all process dependence is collected in H^F and the collinear functions C_{ab} are completely process independent.

The first-order perturbative coefficients of the collinear functions in the hard scheme read

$$C_{qq}^{(1)}(z) = \frac{1}{2} C_F (1 - z), \tag{3.39}$$

$$C_{gq}^{(1)}(z) = \frac{1}{2} C_F z, \tag{3.40}$$

$$C_{qg}^{(1)}(z) = \frac{1}{2} z(1 - z), \tag{3.41}$$

$$C_{gg}^{(1)}(z) = C_{q\bar{q}}^{(1)}(z) = C_{qq'}^{(1)}(z) = C_{q\bar{q}'}^{(1)}(z) = 0, \tag{3.42}$$

where we stated the results in z-space, which is more suitable for practical implementations of the q_T subtraction method. The second order coefficients $C_{ab}^{(2)}$ are also known explicitly in the hard scheme and can be found in Ref. [88].

The only process-dependent information comes from the Born-level loop amplitudes, and these have to enter H^F linearly, as they enter the fixed-order cross section linearly. This observation has been used do derive a general (process-independent) relation between the renormalised loop amplitudes and H^F in Ref. [88]. To state the result, let $\mathcal{M}^F$ denote the renormalised all-loop amplitude of $q\bar{q} \to F$. It can be expanded in terms of n-loop amplitudes as

$$\mathcal{M}^F = \alpha_S^k \left[\mathcal{M}^{F(0)} + \left(\frac{\alpha_S}{2\pi}\right) \mathcal{M}^{F(1)} + \left(\frac{\alpha_S}{2\pi}\right)^2 \mathcal{M}^{F(2)} + \sum_{n=3}^{\infty} \left(\frac{\alpha_S}{2\pi}\right)^n \mathcal{M}^{F(n)} \right], \tag{3.43}$$

where k is the power of α_{S} in the leading order contribution (e.g. $k = 0$ for electroweak processes and $k = 1$ for Higgs production in gluon fusion).

Each renormalised loop amplitude $\mathcal{M}^{\mathrm{F}(n)}$ still contains infrared poles. The poles exhibit a universal structure, which is explicitly known at one and two loops for the processes under consideration [89]. They can be subtracted by the (modified) Catani-I-operators to obtain finite one- and two-loop amplitudes $\widetilde{\mathcal{M}}^{\mathrm{F}(1)}$ and $\widetilde{\mathcal{M}}^{\mathrm{F}(2)}$:

$$\widetilde{\mathcal{M}}^{\mathrm{F}(1)} = \mathcal{M}^{\mathrm{F}(1)} - \widetilde{I}_q^{(1)}(\varepsilon)\mathcal{M}^{\mathrm{F}(0)}, \tag{3.44}$$

$$\widetilde{\mathcal{M}}^{\mathrm{F}(2)} = \mathcal{M}^{\mathrm{F}(2)} - \widetilde{I}_q^{(1)}(\varepsilon)\mathcal{M}^{\mathrm{F}(1)} - \widetilde{I}_q^{(2)}(\varepsilon)\mathcal{M}^{\mathrm{F}(0)}. \tag{3.45}$$

The one-loop I-operator reads

$$\widetilde{I}_q^{(1)}(\varepsilon) = \widetilde{I}_q^{(1)\mathrm{soft}}(\varepsilon) + \widetilde{I}_q^{(1)\mathrm{coll}}(\varepsilon) \tag{3.46}$$

with

$$\widetilde{I}_q^{(1)\mathrm{soft}}(\varepsilon) = -\frac{e^{\varepsilon\gamma_E}}{\Gamma(1-\varepsilon)}\left(\frac{1}{\varepsilon^2} + \mathrm{i}\pi\frac{1}{\varepsilon} + \delta^{q_{\mathrm{T}}}\right) C_F \left(\frac{M_F^2}{\mu_R^2}\right)^{-\varepsilon}, \tag{3.47}$$

$$\widetilde{I}_q^{(1)\mathrm{coll}}(\varepsilon) = -\frac{1}{\varepsilon}\gamma_q \left(\frac{M_F^2}{\mu_R^2}\right)^{-\varepsilon}, \tag{3.48}$$

and

$$\gamma_q = \frac{3}{2}C_F. \tag{3.49}$$

The constant $\delta^{q_{\mathrm{T}}}$ will be fixed later; it only affects the finite part of the I-operator. The two-loop I-operator reads

$$\widetilde{I}_q^{(2)} = -\frac{1}{2}\left[I_q^{(1)}(\varepsilon)\right]^2 + \left\{\frac{2\pi\beta_0}{\varepsilon}\left[I_q^{(1)}(2\varepsilon) - I_q^{(1)}(\varepsilon)\right] + K I_q^{(1)\mathrm{soft}}(2\varepsilon) + \widetilde{H}_q^{(2)}(\varepsilon)\right\}, \tag{3.50}$$

with

$$I_q^{(1)}(\varepsilon) \equiv \widetilde{I}_q^{(1)}(\varepsilon, \delta^{q_{\mathrm{T}}} = 0), \tag{3.51}$$

$$\widetilde{H}_q^{(2)}(\varepsilon) = \frac{1}{4\varepsilon}\left(\frac{M_F^2}{\mu_R^2}\right)^{-2\varepsilon}\left(\frac{1}{4}\gamma_{q(1)} + C_F d_{(1)} + \varepsilon C_F \delta_{(1)}^{q_{\mathrm{T}}}\right). \tag{3.52}$$

The constants K and $d_{(1)}$ in Eq. (3.52) are given by

$$K = \left(\frac{67}{18} - \frac{\pi^2}{6}\right) C_A - \frac{5}{9}N_f, \tag{3.53}$$

$$d_{(1)} = \left(\frac{28}{27} - \frac{1}{3}\zeta_2\right) N_f + \left(-\frac{202}{27} + \frac{11}{6}\zeta_2 + 7\zeta_3\right) C_A, \tag{3.54}$$

and $\gamma_{q(1)}$ is the coefficient of the $\delta(1-z)$ term in the NLO quark splitting function,

$$\gamma_{q(1)} = (-3 + 24\zeta_2 - 48\zeta_3)C_F^2 + \left(-\frac{17}{3} - \frac{88}{3}\zeta_2 + 24\zeta_3\right) C_A C_F + \left(\frac{2}{3} + \frac{16}{3}\zeta_2\right) C_F N_f. \tag{3.55}$$

$\delta^{q_\mathrm{T}}_{(1)}$ in Eq. (3.52) is another at this point unspecified constant only affecting the finite part of $\widetilde{I}^{(2)}_q$ and will be fixed later.

The constant contribution to $\mathcal{H}^\mathrm{F}$ and thus, in the hard scheme, the constant contribution to H^F depends linearly on the (finite part of) the squared renormalised loop amplitude, implying that

$$H^{\mathrm{F}(1)} = \frac{\widetilde{\mathcal{M}}^{\mathrm{F}(1)}\mathcal{M}^{\mathrm{F}(0)\dagger} + \widetilde{\mathcal{M}}^{\mathrm{F}(1)\dagger}\mathcal{M}^{\mathrm{F}(0)}}{|\mathcal{M}^{\mathrm{F}(0)}|^2}, \tag{3.56}$$

$$H^{\mathrm{F}(2)} = \frac{|\widetilde{\mathcal{M}}^{\mathrm{F}(1)}|^2 + \widetilde{\mathcal{M}}^{\mathrm{F}(2)}\mathcal{M}^{\mathrm{F}(0)\dagger} + \widetilde{\mathcal{M}}^{\mathrm{F}(2)\dagger}\mathcal{M}^{\mathrm{F}(0)}}{|\mathcal{M}^{\mathrm{F}(0)}|^2} \tag{3.57}$$

for some value of δ^{q_T} and $\delta^{q_\mathrm{T}}_{(1)}$. Furthermore, as $\mathcal{H}^\mathrm{F}$ does not depend on any additional process-dependent input, the constants δ^{q_T} and $\delta^{q_\mathrm{T}}_{(1)}$ are also process independent and can be fixed once and for all. Exploiting the explicit computations of $\mathcal{H}^{\mathrm{F}(1)}$ and $\mathcal{H}^{\mathrm{F}(2)}$ for Higgs boson [90] and vector boson production [91], one finds [88]

$$\delta^{q_\mathrm{T}} = 0, \tag{3.58}$$

$$\delta^{q_\mathrm{T}}_{(1)} = \frac{20}{3}\zeta_3\pi\beta_0 + \left(-\frac{1214}{81} + \frac{67}{18}\zeta_2\right) C_A + \left(\frac{164}{81} - \frac{5}{9}\zeta_2\right) N_f. \tag{3.59}$$

In summary, once the renormalised one- and two-loop amplitudes to the process $q\bar{q} \to \mathrm{F}$ are known, process-independent relations can be used to fix $H^{\mathrm{F}(1)}$ and $H^{\mathrm{F}(2)}$ and thus H^F up to NNLO. As all other ingredients entering the resummed component are process independent, no additional process-dependent input is required to compute $\mathrm{d}\sigma^{(\mathrm{res.})}_\mathrm{F}/\mathrm{d}q^2_\mathrm{T}$.

The finite component $\mathrm{d}\sigma^{(\mathrm{fin.})}_\mathrm{F}/\mathrm{d}q^2_\mathrm{T}$ in Eq. (3.18) is uniquely defined by the requirement of uniform perturbative accuracy over the full range of q_T:

$$\left[\frac{\mathrm{d}\sigma_\mathrm{F}}{\mathrm{d}q^2_\mathrm{T}}\right]_{\mathrm{f.o.}} = \left[\frac{\mathrm{d}\sigma^{(\mathrm{res.})}_\mathrm{F}}{\mathrm{d}q^2_\mathrm{T}}\right]_{\mathrm{f.o.}} + \left[\frac{\mathrm{d}\sigma^{(\mathrm{fin.})}_\mathrm{F}}{\mathrm{d}q^2_\mathrm{T}}\right]_{\mathrm{f.o.}}. \tag{3.60}$$

The matching condition in Eq. (3.60) automatically implements a unitarity constraint on the level of the total cross section. To see this, note that

$$\int_0^\infty \mathrm{d}q^2_\mathrm{T}\, \frac{b}{2}\, J_0(bq_\mathrm{T}) = \delta(b), \tag{3.61}$$

and thus we find from Eq. (3.28)

$$\int_0^\infty \mathrm{d}q_{\mathrm{T}}^2 \frac{\mathrm{d}\sigma_{\mathrm{F}}^{(\mathrm{res.})}}{\mathrm{d}q_{\mathrm{T}}^2} = \mathcal{H}^{\mathrm{F}} \otimes \sigma_{\mathrm{q\bar{q}}}^{\mathrm{F}(0)}, \tag{3.62}$$

i.e. all terms involving large logarithms disappear from $\mathrm{d}\sigma_{\mathrm{F}}^{(\mathrm{res.})}$ upon integration over the transverse momentum. This implies that

$$\int \mathrm{d}q_{\mathrm{T}}^2 \left[\frac{\mathrm{d}\sigma_{ab\to\mathrm{F}}^{(\mathrm{res.})}}{\mathrm{d}q_{\mathrm{T}}^2}\right]_{\mathrm{N^nLL}} = \int \mathrm{d}q_{\mathrm{T}}^2 \left[\frac{\mathrm{d}\sigma_{ab\to\mathrm{F}}^{(\mathrm{res.})}}{\mathrm{d}q_{\mathrm{T}}^2}\right]_{\mathrm{N^nLO}}, \tag{3.63}$$

and we have

$$\begin{aligned}\int \mathrm{d}q_{\mathrm{T}}^2 \left[\frac{\mathrm{d}\sigma_{ab\to\mathrm{F}}}{\mathrm{d}q_{\mathrm{T}}^2}\right]_{\mathrm{l.a.+f.o.}} &= \int \mathrm{d}q_{\mathrm{T}}^2 \left\{\left[\frac{\mathrm{d}\sigma_{ab\to\mathrm{F}}^{(\mathrm{res.})}}{\mathrm{d}q_{\mathrm{T}}^2}\right]_{\mathrm{l.a.}} + \left[\frac{\mathrm{d}\sigma_{ab\to\mathrm{F}}^{(\mathrm{fin.})}}{\mathrm{d}q_{\mathrm{T}}^2}\right]_{\mathrm{f.o.}}\right\} \\ &= \int \mathrm{d}q_{\mathrm{T}}^2 \left[\frac{\mathrm{d}\sigma_{\mathrm{F}}}{\mathrm{d}q_{\mathrm{T}}^2}\right]_{\mathrm{f.o.}} \\ &= \left[\sigma_{ab\to\mathrm{F}}\right]_{\mathrm{f.o.}}. \end{aligned} \tag{3.64}$$

Hence, the total cross section, which is reliably predicted by fixed-order perturbation theory, is not changed by resummation.

To compute $\mathrm{d}\sigma_{\mathrm{F}}^{(\mathrm{fin.})}/\mathrm{d}q_{\mathrm{T}}^2$, we have to expand $\mathrm{d}\sigma_{\mathrm{F}}^{(\mathrm{res.})}/\mathrm{d}q_{\mathrm{T}}^2$ in $\alpha_{\mathrm{S}}(\mu_R^2)$ up to the required order and then subtract the result from the fixed-order truncation of $\mathrm{d}\sigma_{\mathrm{F}}/\mathrm{d}q_{\mathrm{T}}^2$. For this, we write the fixed-order expansion of $\mathcal{W}_{ab}^{\mathrm{F},(N_1,N_2)}$ in Eq. (3.28) as

$$\mathcal{W}_{ab}^{\mathrm{F},(N_1,N_2)} = \sigma_{q\bar{q},\mathrm{F}}^{(0)} \left\{\delta_{qa}\delta_{\bar{q}b} \sum_{n=1}^{\infty} \left(\frac{\alpha_{\mathrm{S}}}{\pi}\right)^n \left[\Sigma_{q\bar{q}\leftarrow ab,\,(N_1,N_2)}^{\mathrm{F}(n)}(\widetilde{L}) + \mathcal{H}_{q\bar{q}\leftarrow ab,\,(N_1,N_2)}^{\mathrm{F}(n)}\right]\right\}, \tag{3.65}$$

where

$$\Sigma_{q\bar{q}\leftarrow ab,\,(N_1,N_2)}^{\mathrm{F}(1)}(\widetilde{L}) = \sum_{n=1}^{2} \Sigma_{q\bar{q}\leftarrow ab,\,(N_1,N_2)}^{\mathrm{F}(1;n)}\, \widetilde{L}^n \tag{3.66}$$

$$\Sigma_{q\bar{q}\leftarrow ab,\,(N_1,N_2)}^{\mathrm{F}(2)}(\widetilde{L}) = \sum_{n=1}^{4} \Sigma_{q\bar{q}\leftarrow ab,\,(N_1,N_2)}^{\mathrm{F}(2;n)}\, \widetilde{L}^n. \tag{3.67}$$

The b integral in Eq. (3.20) can now be performed explicitly. The Bessel transform acts only on the factors of $\widetilde{L}^n$ and yields

$$M_F^2 \int_0^\infty \mathrm{d}b\, \frac{b}{2}\, J_0(bq_{\mathrm{T}})\, \widetilde{L}^n = \widetilde{I}_n(q_{\mathrm{T}}^2/M_F^2). \tag{3.68}$$

Analytical expressions for the $\widetilde{I}_n(q_\mathrm{T}^2/M_F^2)$ were computed in Ref. [87]. They contain contact terms at $q_\mathrm{T} = 0$, which will however drop out of the relevant formulae, as will be seen later. At NNLO, the expressions for $n \leq 4$ are needed. For finite values of their argument q_T^2/M_F^2 they read

$$\widetilde{I}_1(x) = -\frac{b_0}{x} K_1(b_0 x), \tag{3.69}$$

$$\widetilde{I}_2(x) = \frac{2b_0}{x} \left[K_1(b_0 x) \log x - K_1^{(1)}(b_0 x) \right], \tag{3.70}$$

$$\widetilde{I}_3(x) = -\frac{3b_0}{x} \left[K_1(b_0 x) \left(\log^2 x - \zeta_2 \right) - 2K_1^{(1)}(b_0 x) \log x + K_1^{(2)}(b_0 x) \right], \tag{3.71}$$

$$\begin{aligned} \widetilde{I}_4(x) = \frac{4b_0}{x} \Big[& K_1(b_0 x)(\log^3 x - 3\zeta_2 \log x + 2\zeta_3) - 3K_1^{(1)}(b_0 x)(\log^2 x - \zeta_2) \\ & + 3K_1^{(2)}(b_0 x) \log x - K_1^{(3)}(b_0 x) \Big], \end{aligned} \tag{3.72}$$

where $K_1^{(n)}$ denotes the n-th derivative of the Bessel function K_ν w.r.t. to its index ν,

$$K_1^{(n)}(x) \equiv \left[\frac{\partial^n K_\nu(x)}{\partial \nu^n} \right]_{\nu=1}. \tag{3.73}$$

For later reference, we give the explicit expressions for the functions entering in Eq. (3.65) at NLO and NNLO in Eqs. (3.74) to (3.76) and Eqs. (3.77) to (3.81) respectively [87]:

$$\Sigma^{\mathrm{F}\,(1;2)}_{q\bar{q}\leftarrow ab,\,(N_1,N_2)} = -\frac{1}{2} A_q^{(1)} \delta_{qa} \delta_{\bar{q}b}, \tag{3.74}$$

$$\Sigma^{\mathrm{F}\,(1;1)}_{q\bar{q}\leftarrow ab,\,(N_1,N_2)} = -\left[\delta_{qa}\delta_{\bar{q}b}\, B_q^{(1)} + A_q^{(1)} + \delta_{qa} \gamma^{(1)}_{\bar{q}b,\,N_2} + \delta_{\bar{q}b} \gamma^{(1)}_{qa,\,N_1} \right], \tag{3.75}$$

$$\begin{aligned} \mathcal{H}^{\mathrm{F}\,(1)}_{q\bar{q}\leftarrow ab,\,(N_1,N_2)} \left(\frac{M_F^2}{\mu_R^2}, \frac{M_F^2}{\mu_F^2} \right) = {} & \delta_{qa}\delta_{\bar{q}b} \left[H^{\mathrm{F}\,(1)} - k\beta_0 \ell_R \right] \\ & + \delta_{qa} C^{(1)}_{\bar{q}b,\,N_2} + \delta_{\bar{q}b} C^{(1)}_{qa,\,N_1} + \left(\delta_{qa} \gamma^{(1)}_{\bar{q}b,\,N_2} + \delta_{\bar{q}b} \gamma^{(1)}_{qa,\,N_1} \right) \ell_F, \end{aligned} \tag{3.76}$$

$$\Sigma^{\mathrm{F}\,(2;4)}_{q\bar{q}\leftarrow ab,\,(N_1,N_2)} = \frac{1}{8} \left(A_q^{(1)} \right)^2 \delta_{qa}\delta_{\bar{q}b}, \tag{3.77}$$

$$\Sigma^{\rm F\,(2;3)}_{q\bar{q}\leftarrow ab,\,(N_1,N_2)} = -\,A_q^{(1)}\left[\frac{1}{3}\,\beta_0\;\delta_{qa}\delta_{\bar{q}b} + \frac{1}{2}\,\Sigma^{\rm F\,(1;1)}_{q\bar{q}\leftarrow ab,\,(N_1,N_2)}\right], \tag{3.78}$$

$$\begin{aligned}\Sigma^{\rm F\,(2;2)}_{q\bar{q}\leftarrow ab,\,(N_1,N_2)}\left(\frac{M_F^2}{\mu_R^2},\frac{M_F^2}{\mu_F^2}\right) &= -\,\frac{1}{2}\,A_q^{(1)}\left[\mathcal{H}^{\rm F\,(1)}_{q\bar{q}\leftarrow ab,\,(N_1,N_2)}\left(\frac{M_F^2}{\mu_R^2},\frac{M_F^2}{\mu_F^2}\right) - \beta_0\;\delta_{qa}\delta_{\bar{q}b}\ell_R\right]\\ &-\,\frac{1}{2}\sum_{a_1,b_1}\Sigma^{\rm F\,(1;1)}_{q\bar{q}\leftarrow a_1b_1,\,(N_1,N_2)}\left[\delta_{a_1a}\gamma^{(1)}_{b_1b,\,N_2} + \delta_{b_1b}\gamma^{(1)}_{a_1a,\,N_1}\right]\\ &-\,\frac{1}{2}\left[A_q^{(2)}\;\delta_{qa}\delta_{\bar{q}b} + \left(B_q^{(1)} - \beta_0\right)\;\Sigma^{\rm F\,(1;1)}_{q\bar{q}\leftarrow ab,\,(N_1,N_2)}\right],\end{aligned} \tag{3.79}$$

$$\begin{aligned}\Sigma^{\rm F\,(2;1)}_{q\bar{q}\leftarrow ab,\,(N_1,N_2)}\left(\frac{M_F^2}{\mu_R^2},\frac{M_F^2}{\mu_F^2}\right) &= -\Sigma^{\rm F\,(1;1)}_{q\bar{q}\leftarrow ab,\,(N_1,N_2)}\,\beta_0\,\ell_R\\ &-\sum_{a_1,b_1}\mathcal{H}^{\rm F\,(1)}_{q\bar{q}\leftarrow a_1b_1,\,(N_1,N_2)}\left(\frac{M_F^2}{\mu_R^2},\frac{M_F^2}{\mu_F^2}\right)\left[\delta_{a_1a}\delta_{b_1b}B_q^{(1)} + \delta_{a_1a}\gamma^{(1)}_{b_1b,\,N_2} + \delta_{b_1b}\gamma^{(1)}_{a_1a,\,N_1}\right]\\ &-\left[\delta_{qa}\delta_{\bar{q}b}\,B_q^{(2)} - \beta_0\left(\delta_{qa}C^{(1)}_{\bar{q}b,\,N_2} + \delta_{\bar{q}b}C^{(1)}_{qa,\,N_1}\right) + \delta_{qa}\gamma^{(2)}_{\bar{q}b,\,N_2} + \delta_{\bar{q}b}\gamma^{(2)}_{qa,\,N_1}\right],\end{aligned} \tag{3.80}$$

$$\begin{aligned}\mathcal{H}^{\rm F\,(2)}_{q\bar{q}\leftarrow ab,\,(N_1,N_2)}\left(\frac{M_F^2}{\mu_R^2},\frac{M_F^2}{\mu_F^2}\right) &= \delta_{qa}\delta_{\bar{q}b}\,H^{\rm F\,(2)} + \delta_{qa}\,C^{(2)}_{\bar{q}b,\,N_2} + \delta_{\bar{q}b}\,C^{(2)}_{qa,\,N_1} + C^{(1)}_{qa,\,N_1}\,C^{(1)}_{\bar{q}b,\,N_2}\\ &+H^{\rm F\,(1)}\left(\delta_{qa}\,C^{(1)}_{\bar{q}b,\,N_2} + \delta_{\bar{q}b}\,C^{(1)}_{qa,\,N_1}\right) + \frac{1}{2}\,\beta_0\,\left(\delta_{qa}\gamma^{(1)}_{\bar{q}b,\,N_2} + \delta_{\bar{q}b}\gamma^{(1)}_{qa,\,N_1}\right)\ell_F^2\\ &+\left(\delta_{qa}\gamma^{(2)}_{\bar{q}b,\,N_2} + \delta_{\bar{q}b}\gamma^{(2)}_{qa,\,N_1}\right)\ell_F - \mathcal{H}^{\rm F\,(1)}_{q\bar{q}\leftarrow ab,\,(N_1,N_2)}\left(\frac{M_F^2}{\mu_R^2},\frac{M_F^2}{\mu_F^2}\right)\beta_0\ell_R\\ &+\frac{1}{2}\sum_{a_1,b_1}\left[\mathcal{H}^{\rm F\,(1)}_{q\bar{q}\leftarrow a_1b_1,\,(N_1,N_2)}\left(\frac{M_F^2}{\mu_R^2},\frac{M_F^2}{\mu_F^2}\right) + \delta_{qa_1}\delta_{\bar{q}b_1}\,H^{\rm F\,(1)} + \delta_{qa_1}\,C^{(1)}_{\bar{q}b_1,\,N_2} + \delta_{\bar{q}b_1}\,C^{(1)}_{qa_1,\,N_1}\right]\\ &\times\left[\left(\delta_{a_1a}\gamma^{(1)}_{b_1b,\,N_2} + \delta_{b_1b}\gamma^{(1)}_{a_1a,\,N_1}\right)\ell_F - \delta_{a_1a}\delta_{b_1b}k\,\beta_0\,\ell_R\right]\\ &-\delta_{qa}\delta_{\bar{q}b}\,k\left(\frac{1}{2}\,\beta_0^2\,\ell_R^2 + \beta_1\,\ell_R\right),\end{aligned} \tag{3.81}$$

where

$$\ell_R = \log\left(\frac{M_F^2}{\mu_R^2}\right), \quad \ell_F = \log\left(\frac{M_F^2}{\mu_F^2}\right). \tag{3.82}$$

The coefficients $A_q^{(1)}$ and $A_q^{(2)}$ are the same as the ones appearing in Eq. (3.32) and are

given by

$$A_q^{(1)} = C_F, \qquad A_q^{(2)} = \frac{1}{2} C_F \left[\left(\frac{67}{18} - \frac{\pi^2}{6} \right) C_A - \frac{5}{9} N_f \right]. \tag{3.83}$$

The coefficients $B_q^{(1)}$ and $B_q^{(2)}$ are related to the $\widetilde{B}_q^{(n)}$ in Eq. (3.33) by

$$\widetilde{B}_{q)}^{(1)} = B_{q,(N_1,N_2)}^{(1)} + 2\gamma_{qq,(N_1,N_2)}^{(1)}, \tag{3.84}$$

$$\widetilde{B}_q^{(2)} = B_{q,(N_1,N_2)}^{(2)} - 2\beta_0 C_{qq,(N_1,N_2)}^{(1)} + 2\gamma_{qq,(N_1,N_2)}^{(2)}. \tag{3.85}$$

$B_q^{(1)}$ is resummation scheme independent and given by

$$B_q^{(1)} = -\frac{3}{2} C_F. \tag{3.86}$$

$B_q^{(2)}$ is resummation scheme dependent. However, as $\widetilde{B}_{q,(N_1,N_2)}^{(2)}$ is process independent, the process dependence has to cancel out of Eq. (3.85). In the hard scheme, $B_q^{(2)}$ itself is process independent, as all process-dependent information is collected in H^{F}, and reads

$$B_q^{(2)} = \frac{\gamma_{q(1)}}{16} + \pi\beta_0 C_F \zeta_2, \tag{3.87}$$

where $\gamma_{q(1)}$ is the coefficient of the $\delta(1-z)$ term in the NLO quark splitting function in Eq. (3.55).

Using Eq. (3.60), we find for the finite component

$$\left[\frac{\mathrm{d}\sigma_{ab\to\mathrm{F}}^{(\mathrm{fin.})}}{\mathrm{d}q_{\mathrm{T}}^2} \right]_{\mathrm{f.o.}} = \left[\frac{\mathrm{d}\sigma_{ab\to\mathrm{F}}}{\mathrm{d}q_{\mathrm{T}}^2} \right]_{\mathrm{f.o.}} - \Sigma_{q\bar{q}\leftarrow ab}^{\mathrm{F}} \left(q_{\mathrm{T}}^2/M_F^2 \right) \otimes \sigma_{q\bar{q}}^{\mathrm{F}(0)} - \left[\mathcal{H}_{q\bar{q}\leftarrow ab}^{\mathrm{F}} \otimes \sigma_{q\bar{q}}^{\mathrm{F}(0)} \right] \delta(q_{\mathrm{T}}^2), \tag{3.88}$$

where $\Sigma_{q\bar{q}\leftarrow ab}\left(q_{\mathrm{T}}^2/M_F^2\right)$ is obtained from $\Sigma_{q\bar{q}\leftarrow ab}$ by performing the b-integral:

$$\Sigma_{q\bar{q}\leftarrow ab}^{\mathrm{F}} \left(q_{\mathrm{T}}^2/M_F^2 \right) = \int \mathrm{d}b \, \frac{b}{2} \, \Sigma_{q\bar{q}\leftarrow ab}^{\mathrm{F}}(\widetilde{L}). \tag{3.89}$$

All $q_{\mathrm{T}} = 0$ contributions have to cancel in the right-hand side of Eq. (3.88), and we therefore obtain

$$\left[\frac{\mathrm{d}\sigma_{ab\to\mathrm{F}}^{(\mathrm{fin.})}}{\mathrm{d}q_{\mathrm{T}}^2} \right]_{\mathrm{f.o.}} = \left[\frac{\mathrm{d}\sigma_{ab\to\mathrm{F+jet}}}{\mathrm{d}q_{\mathrm{T}}^2} \right]_{\mathrm{f.o.}} - \Sigma_{q\bar{q}\leftarrow ab}^{\mathrm{F}} \left(q_{\mathrm{T}}^2/M_F^2 \right) |_{\text{no contact terms}} \otimes \sigma_{q\bar{q}}^{\mathrm{F}(0)}, \tag{3.90}$$

where $\Sigma_{q\bar{q}\leftarrow ab}^{\mathrm{F}}\left(q_{\mathrm{T}}^2/M_F^2\right)|_{\text{no contact terms}}$ only contains contributions regular in q_{T}, i.e. it can be written in terms of the explicit expressions for the $\widetilde{I}_n$ functions in Eqs. (3.69) to (3.72).

3.4 q_T subtraction

The formalism of q_T resummation as discussed in the previous section can now be used to derive the q_T subtraction method. q_T subtraction can be used to perform fixed-order NNLO computations, which are fully exclusive over the QCD jet activity in the final state. We will derive q_T subtraction in its formulation as a pure slicing method and will only briefly comment on how to make the subtraction more local at the end of this section.

q_T subtraction explicitly exploits the fact that a significant part of a NNLO cross section computation consists of computations which are only of NLO complexity. As an illustrative example, we first consider the computation of the 0-jet cross section at NLO accuracy, which can be written as

$$\sigma^{\mathrm{F}}_{\mathrm{NLO}}|_{0-\mathrm{jet}} = \sigma^{\mathrm{F}}_{\mathrm{NLO}}|_{\mathrm{total}} - \sigma^{\mathrm{F+jet}}_{\mathrm{LO}}, \tag{3.91}$$

where $\sigma^{\mathrm{F}}_{\mathrm{NLO}}|_{\mathrm{total}}$ denotes the total cross section for the process $q\bar{q} \to \mathrm{F}$, and $\sigma^{\mathrm{F+jet}}_{\mathrm{LO}}$ is the *leading order* prediction for the production of F plus one additional jet. The analogous relation holds at NNLO,

$$\sigma^{\mathrm{F}}_{\mathrm{NNLO}}|_{0-\mathrm{jet}} = \sigma^{\mathrm{F}}_{\mathrm{NNLO}}|_{\mathrm{total}} - \sigma^{\mathrm{F+jet}}_{\mathrm{NLO}}. \tag{3.92}$$

This implies that in addition to an exclusive (N)LO computation of $q\bar{q} \to \mathrm{F} + \mathrm{jet}$, the computation of the *exclusive* (N)NLO quantity $\sigma^{\mathrm{F}}_{\mathrm{NNLO}}|_{0-\mathrm{jet}}$ only requires an *inclusive* (N)NLO computation of $q\bar{q} \to \mathrm{F}$.

A similar statement is true for *any* infrared-safe observable. To make this precise, we consider the production of an arbitrary non-QCD final state F in quark-antiquark annihilation, i.e. the process $q\bar{q} \to \mathrm{F}$. The crucial observation is that as long as the total transverse momentum q_T of F is non-vanishing, at least one additional QCD emission must be present, and we thus have

$$\mathrm{d}\sigma^{\mathrm{F}}_{\mathrm{N^nLO}}|_{q_T>0} = \sigma^{\mathrm{F+jet}}_{\mathrm{N^{n-1}LO}}. \tag{3.93}$$

We can split the full cross section using some finite cut $q_T^{\mathrm{cut}} > 0$ on the transverse momentum q_T:

$$\mathrm{d}\sigma^{\mathrm{F}}_{\mathrm{N^nLO}} = \mathrm{d}\sigma^{\mathrm{F}}_{\mathrm{N^nNLO}}\,\Theta(q_T^{\mathrm{cut}} - q_T) + \mathrm{d}\sigma^{\mathrm{F+jet}}_{\mathrm{N^{n-1}LO}}\,\Theta(q_T - q_T^{\mathrm{cut}}). \tag{3.94}$$

In a NNLO computation, the second term is a pure NLO quantity and can be computed using standard techniques. The first term is localised at small q_T if q_T^{cut} is chosen small. The idea of q_T subtraction is to replace the contribution to the cross section below q_T^{cut} with the analytically known singular limit. As all subleading contributions in this limit are power suppressed in q_T, a sufficiently small q_T^{cut} allows for an arbitrarily good approximation of the full cross section.

In the limit $q_\mathrm{T} \to 0$, $\mathrm{d}\sigma^\mathrm{F}_{\mathrm{N^nLO}}$ behaves as

$$\frac{\mathrm{d}\sigma^\mathrm{F}_{\mathrm{N^nLO}}}{\mathrm{d}q_\mathrm{T}} \sim \frac{\mathrm{d}\sigma^{\mathrm{F,sing}}_{\mathrm{N^nLO}}}{\mathrm{d}q_\mathrm{T}} \equiv A\,\delta(q_\mathrm{T}) + \sum_{i=0}^{2n-1} B_i \left[\frac{\log^i q_\mathrm{T}}{q_\mathrm{T}}\right]_+ . \tag{3.95}$$

Here, the coefficients A and B_i depend on the Born kinematics, but not on the real-emission kinematics. In particular, to leading order in α_S, A is given by the leading order cross section:

$$A = \sigma^\mathrm{F}_\mathrm{LO} + \mathcal{O}\left(\alpha_\mathrm{S}\right). \tag{3.96}$$

The dominant subleading correction to Eq. (3.95) is proportional to $\log^{2n-1} q_\mathrm{T}$. With Eq. (3.94), this implies that

$$\mathrm{d}\sigma^\mathrm{F}_{\mathrm{N^nLO}} = \mathrm{d}\sigma^{\mathrm{F,sing}}_{\mathrm{N^nLO}}\,\Theta(q_\mathrm{T}^\mathrm{cut} - q_\mathrm{T}) + \mathrm{d}\sigma^{\mathrm{F+jet}}_{\mathrm{N^{n-1}LO}}\,\Theta(q_\mathrm{T} - q_\mathrm{T}^\mathrm{cut}) + \mathcal{O}\left(\log^{2n-1} q_\mathrm{T}^\mathrm{cut}\right). \tag{3.97}$$

To proceed, let $\mathcal{J}$ denote an arbitrary IR-safe measurement function. Due to infrared safety, all real-emission measurement functions have to reduce to the Born measurement function $\mathcal{J}_\mathrm{Born}$ in the low transverse-momentum region, $\mathcal{J} \to \mathcal{J}_\mathrm{Born}$ as $q_\mathrm{T} \to 0$.[4] The corresponding cross section can then be written as

$$\begin{aligned}
\int_0^\infty \mathrm{d}q_\mathrm{T}\,\frac{\mathrm{d}\sigma^\mathrm{F}_{\mathrm{N^nLO}}}{\mathrm{d}q_\mathrm{T}} \times \mathcal{J} &= \int_0^{q_\mathrm{T}^\mathrm{cut}} \mathrm{d}q_\mathrm{T}\,\frac{\mathrm{d}\sigma^{\mathrm{F,sing}}_{\mathrm{N^nLO}}}{\mathrm{d}q_\mathrm{T}} \times \mathcal{J}_\mathrm{Born} + \int_{q_\mathrm{T}^\mathrm{cut}}^\infty \mathrm{d}q_\mathrm{T}\,\frac{\mathrm{d}\sigma^{\mathrm{F+jet}}_{\mathrm{N^{n-1}LO}}}{\mathrm{d}q_\mathrm{T}} \times \mathcal{J} + \mathcal{O}\left(q_\mathrm{T}^\mathrm{cut} \log^{2n} q_\mathrm{T}^\mathrm{cut}\right) \\
&= \int_0^\infty \mathrm{d}q_\mathrm{T}\,\frac{\mathrm{d}\sigma^{\mathrm{F,sing}}_{\mathrm{N^nLO}}}{\mathrm{d}q_\mathrm{T}} \times \mathcal{J}_\mathrm{Born} + \int_{q_\mathrm{T}^\mathrm{cut}}^\infty \mathrm{d}q_\mathrm{T}\,\left[\frac{\mathrm{d}\sigma^{\mathrm{F+jet}}_{\mathrm{N^{n-1}LO}}}{\mathrm{d}q_\mathrm{T}} \times \mathcal{J} - \frac{\mathrm{d}\sigma^{\mathrm{F,sing}}_{\mathrm{N^nLO}}}{\mathrm{d}q_\mathrm{T}} \times \mathcal{J}_\mathrm{Born}\right] \\
&\quad + \mathcal{O}\left(q_\mathrm{T}^\mathrm{cut} \log^{2n} q_\mathrm{T}^\mathrm{cut}\right),
\end{aligned} \tag{3.98}$$

where the integration over the remaining phase space is implicitly understood. Eq. (3.98) shows that $\mathrm{d}\sigma^{\mathrm{F,sing}}_{\mathrm{N^nLO}}/\mathrm{d}q_\mathrm{T}$ can be interpreted as a non-local counterterm cancelling the IR divergence in the real contribution $\mathrm{d}\sigma^{\mathrm{F+jet}}_{\mathrm{N^{n-1}LO}}/\mathrm{d}q_\mathrm{T}$ as $q_\mathrm{T} \to 0$.

An analytic expression for $\mathrm{d}\sigma^{\mathrm{F,sing}}_{\mathrm{N^nLO}}$ is (up to subleading terms) given by the N$^\mathrm{n}$LO truncation of the fixed-order expansion of the resummed component $\mathrm{d}\sigma^{(\mathrm{res.})}_\mathrm{F}/\mathrm{d}q_\mathrm{T}$ in Eq. (3.20)[5]:

$$\frac{\mathrm{d}\sigma^{\mathrm{F,sing}}_{\mathrm{N^nLO}}}{\mathrm{d}q_\mathrm{T}} = \left[\frac{\mathrm{d}\sigma^{(\mathrm{res.})}_\mathrm{F}}{\mathrm{d}q_\mathrm{T}}\right]_{\mathrm{N^nLO}} + \ldots, \tag{3.99}$$

where the ellipsis denote terms which are integrable when $q_\mathrm{T} \to 0$ and thus will only

[4] This is only true up to volume suppressed contributions. For example, two hard back-to-back jets can produce an event with a very small transverse momentum, which however does not correspond to the infrared limit. These contributions are of $\mathcal{O}(1)$ in the limit $q_\mathrm{T} \to 0$ and can thus be collected in the $\mathcal{O}\left(\log^{2n-1} q_\mathrm{T}^\mathrm{cut}\right)$ terms.

[5] The finite component is by definition finite in the limit $q_\mathrm{T} \to 0$.

contribute to $\mathcal{O}\left(q_{\mathrm{T}}^{\mathrm{cut}} \log^{2n} q_{\mathrm{T}}^{\mathrm{cut}}\right)$ in Eq. (3.98).

The first term in Eq. (3.98) can be computed by first performing the q_{T} integral over Eq. (3.20) and then expanding to fixed order. From Eq. (3.62) we have

$$\int_0^\infty \mathrm{d}q_{\mathrm{T}} \frac{\mathrm{d}\sigma_{\mathrm{F}}^{(\mathrm{res.})}}{\mathrm{d}q_{\mathrm{T}}} = \mathcal{H}^{\mathrm{F}} \otimes \sigma_{\mathrm{LO}}^{\mathrm{F}}, \tag{3.100}$$

where $\mathcal{H}^{\mathrm{F}}$ is defined in Eq. (3.34). Expanding Eq. (3.100) to the n-th order gives

$$\int_0^\infty \mathrm{d}q_{\mathrm{T}} \frac{\mathrm{d}\sigma_{\mathrm{N^nLO}}^{\mathrm{F,sing}}}{\mathrm{d}q_{\mathrm{T}}} = \mathcal{H}_{\mathrm{N^nLO}}^{\mathrm{F}} \otimes \sigma_{\mathrm{LO}}^{\mathrm{F}}. \tag{3.101}$$

According to Eq. (3.65), the fixed-order expansion of the second term in the square bracket in Eq. (3.98) reads

$$\frac{\mathrm{d}\sigma_{\mathrm{N^nLO}}^{\mathrm{F,sing}}}{\mathrm{d}q_{\mathrm{T}}} = \left[\mathcal{H}_{\mathrm{N^nLO}}^{\mathrm{F}} \otimes \sigma_{\mathrm{LO}}^{\mathrm{F}}\right] \delta(q_{\mathrm{T}}) + \Sigma_{\mathrm{N^nLO}}^{\mathrm{F}}\left(q_{\mathrm{T}}/M_F\right) \otimes \sigma_{\mathrm{LO}}^{\mathrm{F}} + \ldots, \tag{3.102}$$

where $\Sigma_{\mathrm{N^nLO}}^{\mathrm{F}}$ is the $\mathrm{N^nLO}$ truncation of the function defined in Eq. (3.89). As Eq. (3.102) has to be evaluated at finite q_{T}, we can drop the $\mathcal{H}^{\mathrm{F}}$ term, which is localised at $q_{\mathrm{T}} = 0$, and all contact contributions to the second term:

$$\left.\frac{\mathrm{d}\sigma_{\mathrm{N^nLO}}^{\mathrm{F,sing}}}{\mathrm{d}q_{\mathrm{T}}}\right|_{q_{\mathrm{T}}>0} = \Sigma_{\mathrm{N^nLO}}^{\mathrm{F}}\left(q_{\mathrm{T}}/M_F\right)|_{\text{no contact terms}} \otimes \sigma_{\mathrm{LO}}^{\mathrm{F}} + \ldots. \tag{3.103}$$

Substituting Eqs. (3.101) and (3.103) back into Eq. (3.98) gives

$$\int \mathrm{d}q_{\mathrm{T}} \frac{\mathrm{d}\sigma_{\mathrm{N^nLO}}^{\mathrm{F}}}{\mathrm{d}q_{\mathrm{T}}} \times \mathcal{J} = \mathcal{H}^{\mathrm{F}} \otimes \sigma_{\mathrm{LO}}^{\mathrm{F}} \times \mathcal{J}_{\mathrm{Born}} + \left[\int_{q_{\mathrm{T}}^{\mathrm{cut}}}^\infty \mathrm{d}q_{\mathrm{T}} \frac{\mathrm{d}\sigma_{\mathrm{N^{n-1}LO}}^{\mathrm{F+jet}}}{\mathrm{d}q_{\mathrm{T}}} \times \mathcal{J} - \sigma_{\mathrm{N^nLO}}^{\mathrm{CT}}(q_{\mathrm{T}}^{\mathrm{cut}})\right] + \mathcal{O}\left(q_{\mathrm{T}}^{\mathrm{cut}} \log^{2n} q_{\mathrm{T}}^{\mathrm{cut}}\right), \tag{3.104}$$

where

$$\sigma_{\mathrm{N^nLO}}^{\mathrm{CT}}(q_{\mathrm{T}}^{\mathrm{cut}}) = \left[\int_{q_{\mathrm{T}}^{\mathrm{cut}}}^\infty \mathrm{d}q_{\mathrm{T}}\, \Sigma_{\mathrm{N^nLO}}^{\mathrm{F}}\left(q_{\mathrm{T}}/M_F\right)\right] \otimes \sigma_{\mathrm{LO}}^{\mathrm{F}} \times \mathcal{J}_{\mathrm{Born}}. \tag{3.105}$$

Rewriting Eq. (3.104) yields the q_{T} subtraction master formula at NLO and NNLO in its more familiar form:

$$\mathrm{d}\sigma_{\mathrm{(N)NLO}}^{\mathrm{F}} = \mathcal{H}_{\mathrm{(N)NLO}}^{\mathrm{F}} \otimes \mathrm{d}\sigma_{\mathrm{LO}}^{\mathrm{F}} + \left[\mathrm{d}\sigma_{\mathrm{(N)LO}}^{\mathrm{F+jet}} - \mathrm{d}\sigma_{\mathrm{(N)NLO}}^{\mathrm{CT}}\right]. \tag{3.106}$$

In the form of Eq. (3.104), q_{T} subtraction is a pure slicing method w.r.t. the subtraction of

the genuine NNLO singularities[6]. q_{T} subtraction can however be made more differentially. One obvious potential improvement would be to perform the subtraction differentially in the Born kinematics. This could be done via a mapping from the double-real phase space to the single-real and Born phase spaces. In practice, naive implementations of this procedure do not lead to an improvement in efficiency, mainly because the mapping interferes with the adaptive Monte Carlo optimisation of the phase-space integration.

If the resummation could be extended to additional variables, for example to 0-jettiness $\mathcal{T}_0$ as suggested in Ref. [18], the subtraction could be performed differentially also in these additional variables. Progress on obtaining the relevant factorisation formulae [92, 93] and collinear functions [94] in the case of double-differential resummation in q_{T} and $\mathcal{T}_0$ has been achieved recently in the context of Soft Collinear Effective Theory.

[6]The NLO-like singularities are subtracted completely independently and in practice will always be handled by a local subtraction method.

4 The implementation

In this chapter we outline our implementation of the q_{T} subtraction formalism in a numerical code. We first briefly review adaptive Monte Carlo integration techniques in Section 4.1, as these play a crucial role in obtaining numerically stable results. Different aspects of our implementation of the full NNLO computations into the new framework Matrix are explained in Section 4.2, where we also discuss some of the particular challenges of performing NNLO computations in practice, in particular issues related to numerical stability. Section 4.3 describes the extension of Matrix to the resummation of logarithmically-enhanced contributions to transverse-momentum spectra.

4.1 Monte Carlo integration

The main theorem of Monte Carlo integration states that the integral of any bounded, integrable function f over the d-dimensional volume V can be approximated by

$$I(f) \equiv \int_V \mathrm{d}^d p\, f(\vec{p}) = \int_{[0,1]^d} \mathrm{d}^d x\, f(\phi(\vec{x})) \left|\frac{\partial \phi}{\partial x}\right| \approx \left\langle \frac{f}{g} \right\rangle \equiv \frac{1}{N} \sum_{i=1}^{N} \frac{f(\phi(\vec{x}_i))}{g(\vec{x}_i)}, \tag{4.1}$$

where the invertible function ϕ pulls back the volume V to the d-dimensional hypercube $[0,1]^d$. $\{\vec{x}_i\}$ is a sequence of N random numbers in $[0,1]^d$, distributed according to some probability density h, and g is the probability density according to which $\phi(\{\vec{x}_i\})$ is distributed, i.e. $g = h \times |\partial\phi|^{-1}$. In the limit $N \to \infty$, Eq. (4.1) is exact. An estimate for the statistical accuracy of the Monte Carlo integration is given by the square root of the variance $V(f)$,

$$\sigma_{I(f)} = \sqrt{V(f)}, \tag{4.2}$$

with

$$V(f) = \frac{1}{N-1} \left(\left\langle \left(\frac{f}{g}\right)^2 \right\rangle - \left\langle \frac{f}{g} \right\rangle^2 \right). \tag{4.3}$$

Eq. (4.3) demonstrates the main advantage of Monte Carlo integration over deterministic methods: the integration error estimate is proportional to $1/\sqrt{N}$ and thus independent of the number of dimensions d. The error estimate of deterministic methods depends exponentially on d, rendering their application to phase-space integrals, which can easily

reach a dimensionality of $d \sim 10$ and more, impractical or even impossible. The main disadvantage of Monte Carlo integration is its non-deterministic nature. In particular, it is important to note that Eq. (4.3) gives only an estimate of the integration error, and the true integration error can easily be underestimated, in particular if N is small or if the integrand has a complicated singularity structure.

In the following, we will discuss strategies to improve on naive Monte Carlo integration. These more sophisticated techniques are important both to achieve sufficient performance and a numerically stable integration of phase-space integrals over complicated integrands.

4.1.1 Importance sampling

The basic idea of importance sampling is to optimise the probability density g such that the total variance is minimised. As the suitability of the parameterisation will depend on the process and subprocess under consideration and can even vary significantly with the cuts applied in an analysis, manual optimisation is usually too cumbersome in practice. Several ideas have been proposed to optimise g automatically "on the fly": after a certain amount of generated events, the Monte Carlo estimates of the integral in Eq. (4.1) and its variance in Eq. (4.3) are used to modify g such that the integration becomes more efficient. This procedure can be iterated until no further improvement occurs.

The optimal choice would be $g \propto f$, as this would flatten out the integrand completely. However, this would require the knowledge of the integral one wants to compute in the first place, and in practical implementations of an adaptive algorithm one can only hope to find a better g than the initial choice, not an optimal one.

One possibility is based on a factorisable ansatz for g:

$$g(\vec{x}) = \prod_{i=1}^{d} g_i(x_i). \tag{4.4}$$

This ansatz avoids the exponential rise in complexity with the number of dimensions d: if, for example, each probability density g_i is sampled with K bins, only $d \times K$ numbers have to be stored instead of K^d, as would be the case if one wanted to allow for a fully general g.

Taking the functional derivative of Eq. (4.3) w.r.t. g_i and setting the result to zero shows that the optimal choice is equivalent to

$$g_i(x_i) \propto \sqrt{\int_0^1 \left(\prod_{j \neq i} \frac{\mathrm{d}x_j}{g_j(x_j)} \right) f^2(\vec{x})}. \tag{4.5}$$

Implementing an adaptive strategy to optimise the g_i's is now straightforward: after a certain number of events, the Monte Carlo estimate of the right-hand side of Eq. (4.5) is used to improve the probability density functions g_i, and this procedure can be iterated until no further improvement is found. This approach forms the basis of the well-known

VEGAS algorithm [95].

4.1.2 Multichannel parameterisation

The main advantage of the VEGAS ansatz in Eq. (4.4) is its general applicability. However, its effectiveness in improving the convergence of the Monte Carlo integration requires the integrand to be approximately factorisable along the coordinate axes, which is a feature not only dependent on the physical problem at hand, but also on the parameterisation of the integral.

On the other hand, if the class of integrands is restricted to phase-space integrals, a priori knowledge of the integrand becomes available. This knowledge can be used to improve the parameterisation of the integral, both to flatten out the integrand and also to find a parameterisation which might be more suitable for an additional VEGAS-like optimisation.

In the case of leading-order cross sections, the integrand is essentially given by the square of the Born-level matrix element. The resonance structure of a tree-level matrix element is in turn fully determined by the knowledge of all propagators appearing in the diagram and thus known once the partonic process has been specified.

However, even tree-level matrix elements often have a complicated and intricate resonance structure, for example, when both s- and t-channel diagrams contribute. While a phase-space parameterisation for a single resonance is easy to construct, combining several resonances inside the same parameterisation is usually not feasible. A possible way out is to consider a family of parameterisations – a so-called multichannel Monte Carlo [96] –, each one flattening out one of the resonances of the integrand.

A typical strategy for the generation of a set of phase-space parameterisations is to enumerate all tree-level diagrams contributing to the relevant amplitude and then to choose for each of them a parameterisation which flattens out the resonances of this (squared) diagram. It is clear that this procedure can only partially flatten out the integrand, as interference terms mix up different resonance structures. Furthermore, for virtual contributions, the resonance structure of the tree-level diagrams can only be considered an approximation of the true resonance structure. Nonetheless, for the integrals appearing in fixed-order computations, a multichannel parameterisation turns out to be very efficient in flattening out the integrands.

During the integration phase, the paramerisation (or channel) to be used for each single event is determined randomly. In practical computations, the relative importance of the different channels will however not be uniform. To speed up the computation, the probabilities for each channel to be used should be adjusted at runtime.

To make this precise, consider a set of M parameterisations ϕ_i, one for each channel. Each channel is chosen with a probability α_i, which satisfy

$$\sum_{i=1}^{M} \alpha_i = 1, \qquad 0 \leq \alpha_i \leq 1. \tag{4.6}$$

The total probability density appearing in Eq. (4.1) and Eq. (4.3) is then given by

$$g(\vec{x}, j) = \sum_{i=1}^{M} \alpha_i \left| \frac{\partial \phi_i}{\partial \vec{x}} (\phi_i^{-1}(\phi_j(\vec{x}))) \right|^{-1}, \tag{4.7}$$

where j is the channel used to generate the event. Alternatively, Eq. (4.7) can be written as

$$g(\vec{p}) = \sum_{i=1}^{M} \alpha_i \left| \frac{\partial \phi_i}{\partial \vec{x}} (\phi_i^{-1}(\vec{p})) \right|^{-1}, \tag{4.8}$$

where $\vec{p} = \phi_j(\vec{x})$.

The relative size of the α_i's can now be adjusted at runtime to minimise the variance of the Monte Carlo estimate. This is the case if, up to a normalisation,

$$\alpha_i^{\text{new}} = \alpha_i \sqrt{\left\langle \frac{g_i}{g} \left(\frac{f}{g} \right)^2 \right\rangle}, \tag{4.9}$$

as can be see by taking derivatives with respect to α_i of the first term on the left-hand side of Eq. (4.3).

4.1.3 Multichannel parameterisation with importance sampling

In standard NLO applications, a suitably generated multichannel parameterisation is generally very efficient in sampling the phase space. In applications of q_{T} subtraction, however, the deep infrared region of the real-emission phase space needs to be probed. It turns out that – in particular if photons are present in the final state – a multichannel parameterisation is not enough to reliably capture all relevant contributions to the phase-space integral.

This breakdown already occurs when evaluating the single-real emission contribution. VEGAS on the other hand turns out to be able to compute at least the single-emission contribution reliably. This suggests a merging of the two adaptation strategies outlined above: a full multichannel parameterisation which allows for an additional adaptive optimisation of the parameterisations in each channel separately. Introducing M non-uniform probability densities g_i, one for each channel, Eq. (4.8) becomes

$$g(\vec{p}) = \sum_{i=1}^{M} \alpha_i \, g_i(\phi_i^{-1}(\vec{p})) \left| \frac{\partial \phi_i}{\partial \vec{x}} (\phi_i^{-1}(\vec{p})) \right|^{-1}. \tag{4.10}$$

Adaptive weight optimisation both for the g_i's and for the α_i's can be performed according to Eq. (4.5) and Eq. (4.9) respectively, where the g_i optimisation now has to be done on a channel-by-channel basis. The main complication comes from the necessity of knowing

the inverse of each phasespace mapping ϕ_i analytically, which was not necessary in a pure multichannel, where $\partial\phi_i$ is easy to evaluate at $\phi_i^{-1}(\vec{p})$. However, the mappings suggested in Ref. [97] and implemented in the MUNICH multichannel can in fact be inverted analytically.

For high-dimensional phase-space integrals and many channels, the evaluation of Eq. (4.10) can become computationally expensive. To work around this problem, one can replace Eq. (4.10) by

$$g(\vec{p}) = g_j(\phi_j^{-1}(\vec{p})) \sum_{i=1}^{M} \alpha_i \left| \frac{\partial\phi_i}{\partial\vec{x}}(\phi_i^{-1}(\vec{p})) \right|^{-1} \tag{4.11}$$

when the j-th channel has been used to generate the event. This amounts to performing the importance sampling optimisation separately for each parameterisation, without interplay between the separate channels. The disadvantage is that the phase-space weight of an event generated in channel j might not get sufficiently damped when hitting a resonance belonging to a different channel i. However, this can only occur if the corresponding probability density g_i is strongly non-uniform.

A second possible variant of the strategy outlined above consists in identifying some of the (factors) of the g_i's with each other. This makes sense as many channels differ from each other only by subdiagrams and thus all factors in g_i corresponding to a common subdiagram can be expected to be very similar after the weight optimisation has finished. In practice, this approach turned out to be the most efficient one and is the default used in all computations presented in this thesis.

4.2 Technical details of the implementation

4.2.1 The Munich NLO framework

We based our NNLO implementation on the MUNICH NLO framework [39]. MUNICH is a automated tool written in C++ to compute NLO QCD and EW corrections to arbitrary SM processes. It was originally developed for the computations in Ref. [77], where only massless QCD particles were involved, using the Catani-Seymour dipole formalism to cancel the infrared singularities. It was extended to deal with massive QCD particles in Ref. [78], and electroweak corrections were added in Ref. [98].

MUNICH is able to generate the necessary dipole subtraction terms automatically from the flavour structure of the underlying process. It comes with an interface to the one-loop generator OPENLOOPS [11], which can also be used to obtain the colour and spin correlated tree-level matrix elements needed for the dipole terms. MUNICH provides a complete automation at NLO, requiring the user only to specify the hadronic process under consideration. MUNICH's phase-space generation is based on the multichannel approach outlined in Section 4.1.2.

Additonal features include the automatic computation of scale uncertainties both for total cross sections and for distributions, the computation of arbitrarily many single-

differential distributions in a single run, and a natural parallelisation of the computation into partonic channels.

We implemented the various pieces in Eq. (3.106) directly into MUNICH and relied on the existing NLO infrastructure as much as possible. We will give details of the implementation in the following. To deal with the special requirements of an NNLO computation, some additional modifications had to be made to MUNICH, which will also be discussed in the following.

4.2.2 The counterterm

The counterterm $\mathrm{d}\sigma^{\mathrm{CT}}_{(\mathrm{N})\mathrm{NLO}}$, defined in Eq. (3.105), lives on the Born phasespace, but contains an explicit dependence on q_{T}. Up to the Born-level cross section, the counterterm at NLO and NNLO is given by the q_{T} integral of the functions (see also Eq. (3.67))

$$\Sigma^{(1)}(q_{\mathrm{T}}/M_F, \ell_R, \ell_F) = \frac{1}{M_F^2} \sum_{n=1}^{2} \Sigma^{(1;n)}\,(\ell_R, \ell_F)\ \tilde{I}^n(q_{\mathrm{T}}/M_F), \tag{4.12}$$

$$\Sigma^{(2)}(q_{\mathrm{T}}/M_F, \ell_R, \ell_F) = \frac{1}{M_F^2} \sum_{n=1}^{4} \Sigma^{(2;n)}\,(\ell_R, \ell_F)\ \tilde{I}^n(q_{\mathrm{T}}/M_F) \tag{4.13}$$

respectively, where ℓ_R and ℓ_F are the logarithms of the scale ratios defined in Eq. (3.82).

q_{T} subtraction is a non-local subtraction method, and to compute the terms in the square bracket in Eq. (3.106) a technical cut needs to be applied to exclude the $q_{\mathrm{T}} \to 0$ region and render the real contribution and the counterterm separately finite. The technical cut can be applied directly on q_{T}. However, the quantity controlling the divergence of the real phase-space integral is the dimensionless ratio $r \equiv q_{\mathrm{T}}/M_F$, and it thus makes sense to instead implement the technical cut as a cut $r_{\mathrm{cut}} \equiv q_{\mathrm{T}}^{\mathrm{cut}}/M_F$ on this ratio. The q_{T} integral in Eq. (3.105) can then be written as

$$\int_{(r_{\mathrm{cut}} M_F)}^{\infty} \frac{\mathrm{d}q_{\mathrm{T}}^2}{M_F^2}\, \tilde{I}(q_{\mathrm{T}}/M_F) = 2 \int_{r_{\mathrm{cut}}}^{\infty} \mathrm{d}r\, r\, \tilde{I}(r), \tag{4.14}$$

i.e. using a technical cut on r instead of a cut on q_{T} itself eliminates the M_F dependence from the $\tilde{I}$ integrals. They can thus be numerically integrated once and for all at the beginning of each run for the set of desired r cuts, rendering the evaluation of $\mathrm{d}\sigma^{\mathrm{CT}}_{(\mathrm{N})\mathrm{NLO}}$ very efficient.

Inspection of the explicit expressions for $\Sigma^{(1;n)}$ and $\Sigma^{(2;n)}$ in Eqs. (3.74) and (3.75) shows that $\Sigma^{(1;n)}$ is completely process-independent. The functions $\Sigma^{(2;n)}$ entering the NNLO counterterm do contain an explicit process dependence in the form of the hard-collinear coefficient $H^{\mathrm{F}(1)}$, which, according to Eq. (3.56), is directly related to the suitably IR subtracted one-loop amplitude $|\widetilde{\mathcal{M}}^{\mathrm{F}(1)}|^2$ of the Born-level process. The one-loop amplitude is needed in the virtual corrections of NLO computations and can be obtained from OPENLOOPS. This implies that the implementation of the counterterm contribution can be

organised in such a way that its computation is automated to the same degree as a NLO computation.

4.2.3 $\mathcal{H}^{\mathrm{F}}$ and the double-virtual contribution

The explicit expressions for the NLO and NNLO truncations of $\mathcal{H}^{\mathrm{F}(n)}$ were given in Eq. (3.76) and Eq. (3.81). In the hard scheme, i.e. when setting the delta terms in $C^{(1)}$ and $C^{(2)}$ to zero, the only process dependence in $\mathcal{H}^{\mathrm{F}}$ comes from its explicit delta term $H^{\mathrm{F}(n)}$, which can be obtained from the one- and two-loop corrections to the Born amplitude according to Eqs. (3.56) and (3.57). The process-independent part of $\mathcal{H}^{\mathrm{F}}$ can be implemented once and for all.

As explained above, $H^{\mathrm{F}(1)}$ can be computed from the one-loop amplitude obtained from OpenLoops, and it thus does not have to be supplied manually. The same holds true for the one-loop squared contribution entering $H^{\mathrm{F}(2)}$. However, $H^{\mathrm{F}(2)}$ also depends on the two-loop amplitude, which is the only process-dependent ingredient which has to be provided on a process-by-process basis in our implementation.

For $Z\gamma$ and $W\gamma$, we implemented the two-loop amplitudes ourselves, starting from the expressions in Ref. [99] and Ref. [19] and performing the IR subtraction according to Eq. (3.45). The analytic expressions of the amplitude are given in terms of (generalised) harmonic polylogarithms with weight at most four and can thus be evaluated using the `tdhpl` library [100]. Our C++ implementation of the amplitudes turns out to be extremely efficient and stable, allowing for several thousand evaluations per minute.

Matrix also contains implementations of the two-loop amplitudes for on-shell ZZ and on-shell W^+W^- production. The amplitudes cannot be expressed in terms of simple harmonic polylogarithms, and their numerical evaluation thus requires more work. We obtained an implementation of the two-loop amplitudes directly from the authors of Ref. [20], which uses the CLN library from Ref. [101] together with GiNaC [102] to evaluate the multiple polylogarithms appearing in the amplitude. The time needed for one amplitude evaluation is of the order of one second, i.e. still fast enough for all practical purposes.

Finally, also the off-shell helicity amplitudes have become available recently [21, 22]. The authors of Ref. [22] provide a numerical implementation of the two-loop form factors, from which the full off-shell VV' helicity amplitudes can be reconstructed. These need to be supplemented with singly-resonant diagrams of the type $q\bar{q} \to V \to VV'$, which are however of Drell-Yan type and thus can be written using the two-loop quark form factors of Ref. [99]. Matrix already contains a preliminary implementation of the full amplitudes, and a first application was published very recently in Ref. [37].

4.2.4 The real-emission contribution

The real-emission contribution $\mathrm{d}\sigma_{\mathrm{NLO}}^{\mathrm{F+jet}}$ in Eq. (3.106) is in principle a NLO quantity and can be computed using the NLO technology already implemented in Munich, i.e. by using Catani-Seymour dipole subtraction to handle the infrared singularities and OpenLoops to obtain the virtual (one-loop) amplitude. In practice however, the fact that $\mathrm{d}\sigma_{\mathrm{NLO}}^{\mathrm{F+jet}}$ has

to be integrated into the deep infrared-divergent region where $q_\mathrm{T} \gtrsim 0$ makes its evaluation highly nontrivial.

In the dipole formalism, $\mathrm{d}\sigma_\mathrm{NLO}^{\mathrm{F+jet}}$ can be split into a real-virtual (RV), a real-collinear (RC) and a double-real (RR) contribution,

$$\mathrm{d}\sigma_\mathrm{NLO}^{\mathrm{F+jet}} = \mathrm{d}\sigma_\mathrm{RV}^{\mathrm{F}} + \mathrm{d}\sigma_\mathrm{RC}^{\mathrm{F}} + \mathrm{d}\sigma_\mathrm{RR}^{\mathrm{F}}. \tag{4.15}$$

The dipole counterterms in the double-real contribution are implicitly understood, and the explicit poles in the real-virtual contribution have been cancelled with the poles contained in the I-operator, see Eq. (3.11). Hence, each of the three contributions is finite once the technical r cut has been introduced and can be computed separately.

The real-collinear contribution contains all finite terms from the integrated dipoles and the collinear counterterm. Its evaluation is not particularly problematic[1]. In contrast, the real-virtual and the double-real contribution pose significant, but different, challenges when integrated into the deep IR ($q_\mathrm{T} \gtrsim 0$) region.

The real-virtual contribution

The real-virtual contribution requires the evaluation of one-loop matrix elements to F + jet production. Though nowadays a standard task in the context of NLO computations, when evaluating the matrix elements in the deep IR region, i.e. far away from the phase-space region OpenLoops has originally been designed for, numerical instabilities in the amplitude evaluation might be a concern.

OpenLoops re-evaluates potentially problematic phase-space points with different (implementations of) reduction techniques to spot numerical issues. It also comes with a built-in rescue system to "save" unstable points. If problematic points were simply discarded, i.e. their weight set to zero, a significant bias on the cross section prediction could be introduced, since mainly phase-space points in the deep IR region would be affected. This could easily spoil the cancellation of the $q_\mathrm{T} \to 0$ singularity in a NNLO computation.

To perform the reduction from tensor to scalar integrals, we make use of the Collier library [103] that contains two independent implementations of the Denner–Dittmaier reduction algorithm [104]. Moreover, as the rescue library to treat exceptionally problematic phase-space points, we use the quadruple-precision implementation of the OPP method [105] in CutTools [106], which is employed in combination with OneLOop [107] and is directly provided by OpenLoops.

The OpenLoops rescue system can be configured by the user, and a variety of different options is available. For the computations in this thesis, a conservative setting has been used: every phase-space point is evaluated twice, once with each independent implementation in Collier. If the difference exceeds a relative difference of 2%, the point is re-evaluated in quadruple precision. The quadruple-precision result is then checked by a scaling test, i.e. the matrix element is re-evaluated with all dimensionful parameters res-

[1] It is of the same difficulty as the integration of the single real-emission contribution, needed when computing the NLO cross section with q_T subtraction.

caled by a common factor ξ and the result is compared with the appropriately rescaled original result. If the scaling test fails, the phase-space point is discarded. In practice, this only happens for extremely low values of the technical r cut, much below the cut values used for producing the phenomenological results in this thesis.

While for some processes, e.g. $Z\gamma$ and $W\gamma$ production, the Denner-Dittmaier reduction works very reliably and the quadruple-precision implementation is not needed in practice, other processes, for example W^+W^- production, are more problematic. However, the OpenLoops rescue system works reliably in all situations we have encountered so far and in general can be trusted to provide stable amplitudes.

The double-real contribution

The double-real contribution only involves tree-level amplitudes, but contains an additional unresolved parton in the final state. Moreover, it involves several dipole terms located on different $(n+1)$-particle phase spaces. Like any other phase-space cut, the restriction $r > r_{\text{cut}}$ has to be applied on the respective phase space. This can lead to miscancellation issues, where some of the dipole terms are cut away, but the $(n+2)$-particle event remains (or vice versa). These problems are well-known from NLO calculations, but their effect can be amplified in the IR divergent region of the phase space.

These complications render the numerical phase-space integration in the deep IR region more challenging compared to the integration of the single-emission phase space. By varying technical parameters of the integration[2], using different combinations of Monte Carlo techniques as explained in Section 4.1.3 and by monitoring the χ^2 of parallel runs of the same subcontribution, the correctness of the integration can be tested. It turns out that the hybrid Monte Carlo technique outlined in Section 4.1.3 is able to reliably integrate the double-real emission contribution for all processes considered in this thesis.

In any case, a sufficiently stable $r_{\text{cut}} \to 0$ behaviour provides the final and strongest check on the correctness of both the real-virtual and the double-real emission contribution.

4.2.5 Monitoring the r_{cut} dependence

Our implementation automatically computes the cross section at a set of predetermined values of the slicing parameter $r_{\text{cut}} \equiv q_{\text{T}}/M_F$, which allows one to monitor the stability of the result. In addition, the NLO computation can be performed either with q_{T} subtraction or with Catani-Seymour subtraction.

The $r_{\text{cut}} \to 0$ behaviour strongly depends on the process under consideration. The generic situation for the production of massive vector bosons and vector boson pairs is shown in Fig. 4.1 (left) for the example of $ZZ(\to e^+e^-\mu^+\mu^-)$ production. Computing the NLO cross section with q_{T} subtraction and comparing with the NLO cross section obtained using CS subtraction shows that even for relatively large values of r_{cut} of around 2%, the agreement is already at the level of one permille. At NNLO, we can compare the r_{cut}

[2]Examples include the technical cutoff near NLO-like IR singularities and parameters affecting the mapping of resonances in the phase-space parameterisation.

dependent cross section with the cross section obtained at $r_{\text{cut}} = 0.2\%$, and find that its relative variation over the entire considered range is well below one permille.

The situation is different if an isolated photon is present in the final state. Fig. 4.1 (right) shows the situation for $W^-\gamma(\to \ell^-\bar{\nu}\gamma)$ production. It can be seen that at $r_{\text{cut}} = 1\%$, the NLO cross section obtained with q_{T} subtraction is still about two percent away from the correct result. Accuracy at the permille level is only reached for very small cut values of $r_{\text{cut}} \approx 0.1\%$. The NNLO cross section shows a similar behaviour as the NLO cross section.

The difference comes from the photon isolation, which is needed to obtain a finite cross section beyond LO, but which interferes with the q_{T} subtraction. The photon isolation has to remove events where the photon in the final state becomes collinear to a final-state quark. To not spoil the cancellation of IR singularities, we typically rely on the smooth cone isolation proposed in Ref. [108]. This prescription vetoes events in which the total hadronic energy $E_T(r)$ in any cone with radius $r < R$ around a photon is larger than $E_T^{\max}(r)$. $E_T^{\max}(r)$ is of the form

$$E_T^{\max}(r) \equiv \epsilon_\gamma \, p_{\text{T}}^\gamma \chi(r), \tag{4.16}$$

where ϵ_γ is an arbitrary constant, p_{T}^γ is the transverse momentum of the photon, and χ is a function which satisfies $\chi(r) \to 0$ as $r \to 0$. In particular, completely collinear QCD activitity is always vetoed. The interplay with q_{T} subtraction comes from additional logarithms of q_{T}, which arise when integrating the cross section inside the cone around a final-state photon [108]. These logarithms are integrable, but require a significantly lower technical cut on q_{T} to become numerically negligible.

4.3 From q_{T} subtraction to q_{T} resummation

As explained in Chapter 3, the derivation of the q_{T} subtraction master formula Eq. (3.106) is based on transverse-momentum resummation. Conceptually, the main difference between a fixed-order computation using q_{T} subtraction and a resummed computation of the transverse-momentum spectrum is the fact that in the former the resummed component of the cross section in Eq. (3.28) has been integrated over the whole q_{T} range, see Eq. (3.100). Turning this observation around, it becomes apparent that once q_{T} subtraction has been implemented at NNLO for a given process, it is relatively straightforward to also resum the large logarithms affecting the transverse-momentum spectrum for the same process up to next-to-next-to-leading logarithmic accuracy.

Comparing the components entering the transverse-momentum resummed cross section in Eq. (3.28) and Eq. (3.90) with the q_{T} subtraction master formula Eq. (3.104) shows that two steps are necessary to assemble the former from the contributions entering the latter:

- The virtual contribution $\mathcal{H}^{\text{F}} \otimes \sigma_{\text{LO}}^{\text{F}}$ has to be replaced by the full resummed cross section.

- The binning has to be adjusted: in a fixed-order computation, both the virtual and

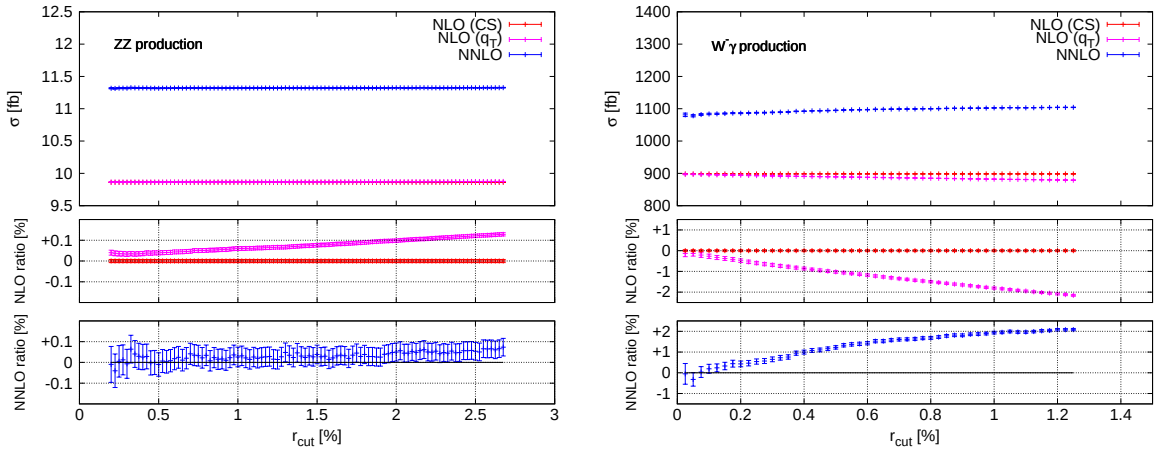

(a) ZZ production. (b) $W^-\gamma$ production.

Figure 4.1: r_{cut} dependence of the NLO (magenta) and NNLO (blue) cross section for ZZ and $W^-\gamma$ production. The r_{cut} independent NLO cross section computed with CS subtraction is also shown (red). The lower panels show the ratio of the NLO cross section computed with q_T subtraction over the same NLO cross section computed with CS subtraction, and the ratio of the NNLO cross section over the NNLO cross section evaluated at the smallest considered value of r_{cut}.

the counterterm contribution are multiplied by the Born-level measurement function $\mathcal{J}_{\text{Born}}$ and thus are binned at $q_T = 0$. In a resummed computation all contributions are binned at a finite transverse momentum.

The resummed component of the cross section is, up to a dependence on $H^{F(1)}$ and $H^{F(2)}$, process independent, i.e. it does exhibit exactly the same process dependence as the virtual contribution in the corresponding NNLO computation, encoded in the same functions. We interfaced our fixed-order implementation with the MoRe library, which, taking $H^{F(1)}$ and $H^{F(2)}$ as inputs, computes the resummed component of the cross section. MoRe itself is based on the computations in Refs. [109, 110].

To achieve the correct binning, one has to first boost the whole final state to the correct transverse momentum; equivalently, the final state has to absorb the transverse-momentum recoil. Afterwards, the binning and the application of cuts can be performed as in a fixed-order computation. The absorption of the recoil necessarily introduces some arbitrariness into the generation of the phase space, which is however an intrinsic feature of the resummation formalism: while the total transverse momentum of the final-state system is fixed, the corresponding azimuthal angle φ does not enter the resummation formula. φ can thus be chosen arbitrarily. In the following, we adopt the standard procedure [111, 112] of generating φ uniformly in $[0, 2\pi]$. However, many observables (such as the total transverse momentum of F) are independent of this arbitariness. In fact, all observables studied in resummed computations in this thesis do only depend on the total transverse momentum and the Born-level rapidity y, rendering the binning straightforward and unambiguous.

5 LHC phenomenology

This chapter contains the phenomenological results obtained with our newly developed NNLO framework so far. We present results for $Z\gamma$ and $W\gamma$ production in Section 5.1, for ZZ production in Section 5.2 and for W^+W^- production in Section 5.3. The first application of MATRIX to the resummation of transverse-momentum spectra is presented in Section 5.4.

5.1 $Z\gamma$ and $W\gamma$ production

The first application of our implementation of q_{T} subtraction we will discuss is the computation of NNLO corrections to $Z\gamma$ and $W\gamma$ production at the LHC. These results were first presented in Refs. [25, 32, 113]. As the full two-loop helicity amplitudes have been implemented, we can consistently include the decay of the heavy vector boson, i.e. $Z \to \ell^+\ell^-$ or $Z \to \nu_\ell\bar{\nu}_\ell$, $W^+ \to \ell^+\nu_\ell$ and $W^- \to \ell^-\bar{\nu}_\ell$, including spin correlations and off-shell effects. Final state radiation (FSR) contributions, where the photon is radiated from a final-state lepton, are also consistently included. The relevant tree-level Feynman diagrams for $Z\gamma$ and for $W^\pm\gamma$ production can be found in Fig. 5.1 and Fig. 5.2 respectively.

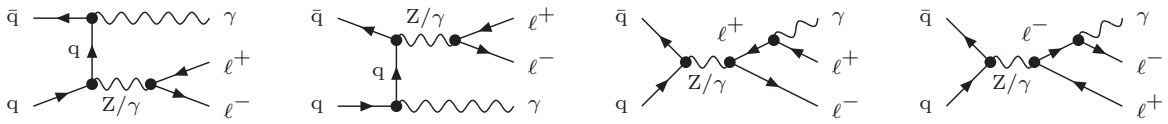

(a) Topology Ia (b) Topology Ib (c) Topology IIa (d) Topology IIb

Figure 5.1: Feynman diagrams contributing to $Z\gamma$ production at Born level.

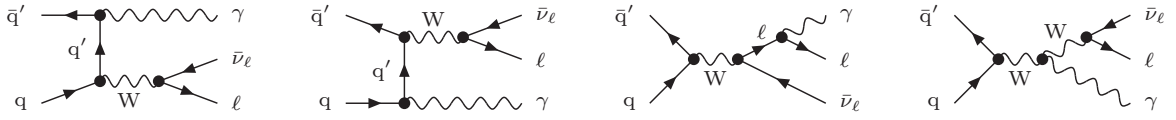

(a) Topology Ia (b) Topology Ib (c) Topology IIa (d) Topology III

Figure 5.2: Feynman diagrams contributing to $W\gamma$ production at Born level.

The NLO $V\gamma$ cross section was first computed in Ref. [114, 115], and the leptonic decay of the vector boson was included in Ref. [116]. In the case of $Z\gamma$, the loop-induced gluon-fusion contribution, which is formally of next-to-next-to-leading order, was computed in Ref. [117, 118], and the leptonic decay of the Z boson, together with the gluon-induced tree-level NNLO contributions from $gg \to Z\gamma\, q\bar{q}$, were added in Ref. [119]. The NLO calculation for $V\gamma$ production, including photon radiation from the final-state leptons, the loop-induced gluon contribution and the photon fragmentation at LO are available in the general purpose numerical program MCFM [120]. Electroweak corrections to $V\gamma$ production were computed in Refs. [121, 122]. The full NLO EW corrections to $W\gamma$ production with leptonically decaying W bosons, taking into account all off-shell effects in the complex-mass scheme and all effects originating from initial-state photons, were computed in Ref. [123]. For $W\gamma$ production, the NLO computation was matched to a parton shower according to the MiNLO prescription [124] in Ref. [125].

5.1.1 Setup

For the electroweak couplings we use the so-called G_μ scheme, where the input parameters are G_F, m_W, m_Z. In particular we use the values $G_F = 1.16639 \times 10^{-5}$ GeV^{-2}, $m_W = 80.399$ GeV, $m_Z = 91.1876$ GeV, $\Gamma_Z = 2.4952$ GeV and $\Gamma_W = 2.1054$ GeV. We set the CKM matrix to unity. We use the MMHT 2014 [54] sets of parton distribution functions, with densities and α_S evaluated at each corresponding order (i.e., we use $(n+1)$-loop α_S at N^{n}LO, with $n = 0, 1, 2$), and we consider $N_f = 5$ massless quarks/antiquarks and gluons in the initial state.

The default renormalisation and factorisation scales are set to $\mu_R = \mu_F = \mu_0 \equiv \sqrt{m_V^2 + (p_T^\gamma)^2}$. An estimate of missing higher-order contributions is obtained by performing μ_F and μ_R variations by a factor of two around the central value. We find substantial cancellations between renormalisation and factorisation scale variations in some of the calculations we are going to present if the restriction $\mu_R = \mu_F$ is imposed. These cancellations are assumed to be purely accidental. To accommodate for this well-known feature, we consider also antipodal variations of the two scales [120], i.e. setting $\mu_R = \xi\mu_0$, $\mu_F = \mu_0/\xi$ and varying ξ between $\frac{1}{2}$ and 2. In summary, we estimate scale uncertainties by varying μ_F and μ_R simultaneously and independently in the range $0.5\mu_0$ and $2\mu_0$ with no constraint on the ratio μ_F/μ_R.

The present formulation of the q_T subtraction formalism [38] is limited to the production of colourless systems F and, hence, it does not allow us to deal with the parton fragmentation subprocesses. Therefore, we consider only direct photons, and we rely on the smooth cone isolation criterion [108]. Considering a cone of radius $r = \sqrt{(\Delta\eta)^2 + (\Delta\phi)^2}$ around the photon, we require that the total amount of hadronic (partonic) transverse energy E_T inside the cone is smaller than $E_T^{\max}(r)$,

$$E_T^{\max}(r) \equiv \epsilon_\gamma\, p_T^\gamma \left(\frac{1-\cos r}{1-\cos R}\right)^n , \tag{5.1}$$

where p_{T}^{γ} is the photon transverse momentum; the isolation criterion $E_T < E_T^{\max}(r)$ has to be fulfilled for all cones with $r \leq R$. All results presented in this section are obtained with $\epsilon_\gamma = 0.5$, $n = 1$ and $R = 0.4$.

5.1.2 Comparison to experimental data

The smooth cone isolation prescription adopted in our calculation is not yet implemented in experimental analyses. Measurements are usually performed by using a fixed cone isolation prescription, given by Eq. (5.1) with $n = 0$, and thus our isolation prescription does not exactly correspond to what is done in the experiment. However, the parameters ϵ_γ and R needed to specify the smooth cone have natural counterparts in the definition of the fixed cone, while the precise choice of the smoothing function (in our case parametrised by n) does only have a mild impact on the final result. Furthermore, recent studies carried out in diphoton production [126] show that for sufficiently tight isolation parameters, smooth and hard cone isolation yield very similar results. For the processes in this section, we verified at NLO that the difference between using smooth and hard cone isolation is at the $1 - 2\%$ level[1], i.e. well below the current experimental uncertainties and still smaller than the remaining theoretical uncertainties. We can thus safely compare our theoretical predictions with experimental data.

Since the first results of our work have appeared [25, 113], we have provided numerical predictions for $Z\gamma$ production to the CMS collaboration [127], and for $W\gamma$ production to the ATLAS collaboration [128]. These predictions were obtained by using the experimental cuts adopted in the corresponding analyses. In this section, we limit ourselves to the comparison of our predictions to the ATLAS results for $W\gamma$ and $Z\gamma$ at 7 TeV [40].

5.1.3 $pp \to \ell^+\ell^-\gamma$

In our calculation of $pp \to \ell^+\ell^-\gamma$ at $\sqrt{s} = 7$ and 8 TeV we adopt the selection cuts used by the ATLAS collaboration [40], summarised in Table 5.1. We require the photon to have a transverse momentum of $p_{\mathrm{T}}^{\gamma} > 15\,\mathrm{GeV}$ (soft p_{T}^{γ} cut) or $p_{\mathrm{T}}^{\gamma} > 40\,\mathrm{GeV}$ (hard p_{T}^{γ} cut) and pseudorapidity $|\eta^{\gamma}| < 2.37$. Each of the charged leptons is required to have $p_{\mathrm{T}}^{\ell} > 25$ GeV and $|\eta^{\ell}| < 2.47$, and the invariant mass of the lepton pair must fulfil $m_{\ell^+\ell^-} > 40$ GeV. We require the separation in rapidity and azimuth ΔR between the leptons and the photon to be $\Delta R(\ell, \gamma) > 0.7$. Jets are reconstructed with the anti-k_T algorithm [68] with radius parameter $D = 0.4$. A jet must have $p_{\mathrm{T}}^{\mathrm{jet}} > 30$ GeV and $|\eta^{\mathrm{jet}}| < 4.4$. We require the separation ΔR between the leptons (photon) and the jets to be $\Delta R(\ell/\gamma, \mathrm{jet}) > 0.3$. At $\sqrt{s} = 8\,\mathrm{TeV}$, the jet definition is slightly adjusted by using $|\eta^{\mathrm{jet}}| < 4.5$ instead of $|\eta^{\mathrm{jet}}| < 4.4$, adapting to the ATLAS Run II standard. With respect to resolved jets in the final states, we consider both the inclusive ($N_{\mathrm{jet}} \geq 0$) and the exclusive ($N_{\mathrm{jet}} = 0$) case.

The predicted cross sections with the soft p_{T}^{γ} cut, including the theoretical uncertainties from scale variations obtained as described at the beginning of Section 5.1.1, can be found

[1]The agreement also significantly depends on the fragmentation function used when employing the hard cone isolation, which typically has large uncertainties.

	$\sqrt{s} = 7\,\text{TeV}$	$\sqrt{s} = 8\,\text{TeV}$
Leptons	$p_\text{T}^\ell > 25\,\text{GeV}$	
	$\lvert\eta\rvert < 2.47$	
Photon	$p_\text{T}^\gamma > 15\,\text{GeV}$ (soft p_T^γ cut) or $p_\text{T}^\gamma > 40\,\text{GeV}$ (hard p_T^γ cut)	
	$\lvert\eta^\gamma\rvert < 2.37$	
	Frixione isolation with $\varepsilon_\gamma = 0.5$, $R = 0.4$, $n = 1$	
Jets	anti-k_T algorithm with $D = 0.4$	
	$p_\text{T}^\text{jet} > 30\,\text{GeV}$	
	$\lvert\eta^\text{jet}\rvert < 4.4$	$\lvert\eta^\text{jet}\rvert < 4.5$
	$N_\text{jet} \geq 0$ (inclusive) or $N_\text{jet} = 0$ (exclusive)	
Separation	$m_{\ell^+\ell^-} > 40\,\text{GeV}$	
	$\Delta R(\ell, \gamma) > 0.7$	
	$\Delta R(\ell/\gamma, \text{jet}) > 0.3$	

Table 5.1: Event selection criteria used in the $pp \to \ell^+\ell^-\gamma$ analysis.

in Table 5.2. When going from NLO to NNLO the cross section increases by 8% (3%) in the inclusive (exclusive) case, respectively. The fiducial cross sections measured by ATLAS at 7 TeV [40] are also reported in Table 5.2. Both the NLO and NNLO predictions are in agreement with the experimental result, and the NNLO corrections improve the agreement, especially in the inclusive case.

The reduced impact of QCD radiative corrections when going from the inclusive ($N_\text{jet} \geq 0$) to the exclusive ($N_\text{jet} = 0$) case is a well known feature in perturbative QCD calculations [129]. A stringent veto on the radiation recoiling against the $Z\gamma$ system tends to unbalance the cancellation between positive real and negative virtual contributions, possibly leading to large logarithmic terms. The resummation of these logarithmic contributions has been the subject of intense theoretical studies [130–132], especially in the important case of Higgs boson production. The reduced impact of radiative effects in the presence of a jet veto is often accompanied by a reduction of scale uncertainties. In the present case, since we are considering a process initiated by quark-antiquark scattering, the impact of radiative corrections is smaller than in Higgs boson production. However, a reduction of scale uncertainties from the $N_\text{jet} \geq 0$ to the $N_\text{jet} = 0$ case is already visible in Table 5.2, and may signal the need of more sophisticated (conservative) methods to estimate perturbative uncertainties [130, 133].

Beyond the cross section in the fiducial region, ATLAS has also provided the measured cross section differential in the photon transverse momentum. A comparison of the resulting distribution with our theoretical NLO and NNLO predictions is displayed in Fig. 5.3 for

$\sqrt{s}$ [TeV]		σ_{LO} [pb]	σ_{NLO} [pb]	σ_{NNLO} [pb]	σ_{ATLAS} [pb]
7	$N_{\text{jet}} \geq 0$	$0.8149^{+8.0\%}_{-9.3\%}$	$1.222^{+4.2\%}_{-5.3\%}$	$1.320^{+1.3\%}_{-2.3\%}$	1.31 ± 0.02 (stat) ± 0.11 (syst) ± 0.05 (lumi)
	$N_{\text{jet}} = 0$		$1.031^{+2.7\%}_{-4.3\%}$	$1.059^{+0.7\%}_{-1.4\%}$	1.05 ± 0.02 (stat) ± 0.10 (syst) ± 0.04 (lumi)
8	$N_{\text{jet}} \geq 0$	$0.9244^{+9.0\%}_{-10.2\%}$	$1.387^{+4.3\%}_{-5.7\%}$	$1.504^{+1.3\%}_{-2.5\%}$	
	$N_{\text{jet}} = 0$		$1.157^{+2.6\%}_{-4.5\%}$	$1.188^{+0.8\%}_{-1.5\%}$	

Table 5.2: $pp \to \ell^+\ell^-\gamma$ cross sections with the soft p_{T}^{γ} cut ($p_{\text{T}}^{\gamma} > 15\,\text{GeV}$). Scale uncertainties are obtained from independent variations of μ_R and μ_F around the central scale μ_0, as described in Section 5.1.1. The numerical uncertainty of the NNLO prediction from statistical error and finite r_{cut} are conservatively estimated to be about 0.3%. The last column provides the corresponding results by ATLAS.

$\sqrt{s}$ [TeV]		σ_{LO} [fb]	σ_{NLO} [fb]	σ_{NNLO} [fb]
7	$N_{\text{jet}} \geq 0$	$73.61^{+3.4\%}_{-4.5\%}$	$132.0^{+4.2\%}_{-4.0\%}$	$154.3^{+3.1\%}_{-2.8\%}$
8	$N_{\text{jet}} \geq 0$	$84.09^{+4.3\%}_{-5.5\%}$	$153.1^{+4.6\%}_{-4.5\%}$	$180.1^{+3.1\%}_{-3.0\%}$

Table 5.3: $pp \to \ell^+\ell^-\gamma$ cross sections with the hard p_{T}^{γ} cut ($p_{\text{T}}^{\gamma} > 40\,\text{GeV}$). Scale uncertainties are computed as in Table 5.2. The numerical uncertainty of the NNLO prediction from statistical error and finite r_{cut} is conservatively estimated to be about 0.6%.

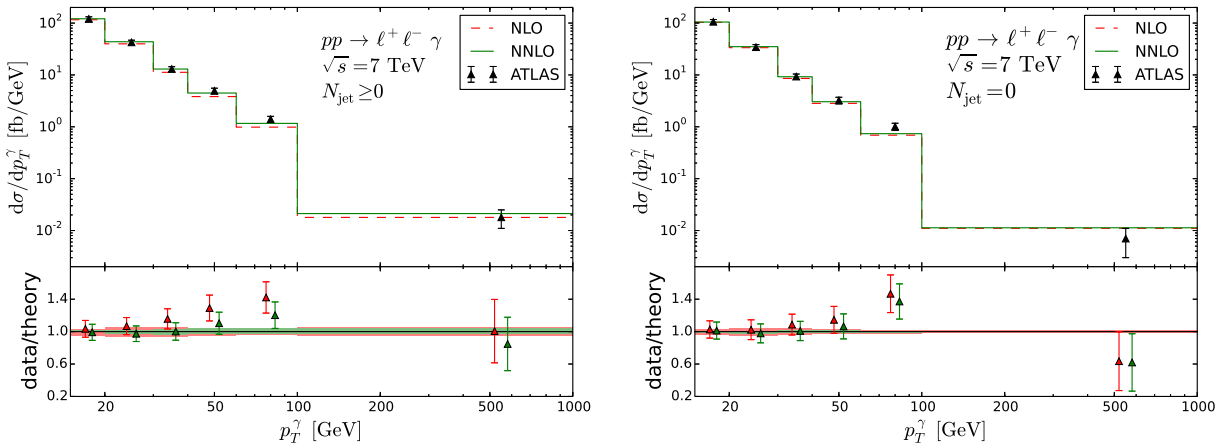

Figure 5.3: Photon transverse-momentum distribution in the inclusive (left) and exclusive case (right) at NLO (red, dashed) and NNLO (green, solid) compared to ATLAS data. In the upper panel, only experimental uncertainties are shown. The lower panel shows the data/theory ratio for both theory predictions, and the bands indicate theoretical uncertainty estimates from scale variations.

both the inclusive and the exclusive case. In particular at transverse momenta $p_{\text{T}}^\gamma \leq 100$ GeV, the inclusion of NNLO corrections tends to improve the agreement between data and theory. The comparison of the theoretical predictions to the data in the high transverse-momentum region $p_{\text{T}}^\gamma > 100$ GeV is quite delicate. First, the experimental uncertainty in this region is quite large. In addition, EW corrections are expected to become sizeable and negative due to large Sudakov logarithmic contributions [121, 122].

In Fig. 5.4 we compare the NLO and NNLO predictions for the invariant-mass distribution of the $\ell^+\ell^-\gamma$ system with the distribution provided by ATLAS in Ref. [40]. For this measurement, ATLAS increases the transverse-momentum cut on the photon from $p_{\text{T}}^\gamma > 15\,\text{GeV}$ to $p_{\text{T}}^\gamma > 40\,\text{GeV}$: the corresponding cross sections are reported in Table 5.3. The relative impact of radiative corrections is 79% and 17% when going from LO to NLO and from NLO to NNLO, respectively. We conclude that the corrections are significantly larger compared to the case in which the soft p_{T}^γ cut ($p_{\text{T}}^\gamma > 15\,\text{GeV}$) is applied. As the $m_{\ell^+\ell^-\gamma}$ differential cross section in Fig. 5.4 is normalised by the fiducial cross section, sizeable NNLO corrections are visible only in the first bin, where the agreement with data is slightly improved. This implies that the NNLO/NLO ratio is almost constant for larger invariant masses.

The more pronounced higher-order corrections in the case in which a hard p_{T}^γ cut is applied can be understood by studying the $\ell^+\ell^-\gamma$ invariant-mass distribution in a finer binning, which is shown in Fig. 5.5 for both the soft and the hard p_{T}^γ cuts. When the soft p_{T}^γ cut is applied, the relative impact of the NNLO corrections is small in the region around the $Z \to \ell^+\ell^-\gamma$ peak, where the fiducial cross section receives its dominant contribution, and then slowly increases with the invariant mass. When the hard p_{T}^γ cut is applied, the $Z \to \ell^+\ell^-\gamma$ peak is not populated at all at LO as the applied cuts produce a lower

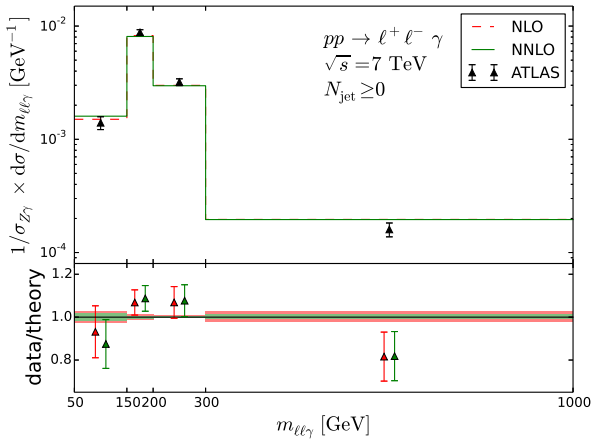

Figure 5.4: The invariant-mass distribution of the $\ell^+\ell^-\gamma$ system at NLO (red, dashed) and NNLO (green, solid), normalised to the fiducial cross section calculated at the respective order, is compared to ATLAS data. The lower panel shows the data/theory ratio, and the bands indicate theoretical uncertainty estimates from scale variations.

bound at $m_{\ell^+\ell^-\gamma} \approx 97\,\text{GeV}$ in LO kinematics. The region below the boundary contributes sizeably to the cross section, but is only populated beyond LO, i.e. in this region the NLO computation provides actually only a LO prediction. Hence the NNLO predictions effectively correspond to the first perturbative correction, with a comparably large K factor of about 1.4. The lower bound on $m_{\ell^+\ell^-\gamma}$ for LO kinematics also exists with the soft p_{T}^{γ} cut, namely at $m_{\ell^+\ell^-\gamma} \approx 66\,\text{GeV}$. However, in this case the $Z \to \ell^+\ell^-\gamma$ peak is populated already at LO, and the region below the cut does not significantly affect the fiducial cross section. As already expected from Fig. 5.4, the NNLO/NLO ratio in the hard p_{T}^{γ} case is almost independent of $m_{\ell^+\ell^-\gamma}$ above $m_{\ell^+\ell^-\gamma} \approx 140\,\text{GeV}$.

Fig. 5.5 also shows the contribution from the loop-induced gluon-fusion process, which represents a finite and gauge invariant subcontribution to the full NNLO result. This contribution is often argued to be potentially sizeable due to the large gluon luminosities at the LHC. In our calculation, however, the gluon-fusion contribution turns out to be small. It amounts only to around 6(9)% of the full $\mathcal{O}(\alpha_{\text{S}}^2)$ correction and, correspondingly, to less than 1(2)% of the total fiducial cross section in the soft and the hard p_{T}^{γ} case, respectively.

5.1.4 $pp \to \nu_\ell\overline{\nu}_\ell\gamma$

In the $pp \to Z\gamma \to \nu_\ell\overline{\nu}_\ell\gamma$ analysis for proton–proton collisions at $\sqrt{s} = 7\,\text{TeV}$, we again use the selection criteria applied by ATLAS [40]: compared to the $pp \to \ell^+\ell^-\gamma$ analysis, the transverse-momentum cut on the photon is made harder ($p_{\text{T}}^{\gamma} > 100\,\text{GeV}$), and a cut on the missing transverse momentum, i.e. the vectorial sum of the neutrino momenta, $p_{\text{T}}^{\nu\bar{\nu}} > 90\,\text{GeV}$, is imposed. The jet algorithm, the photon isolation and all other event-

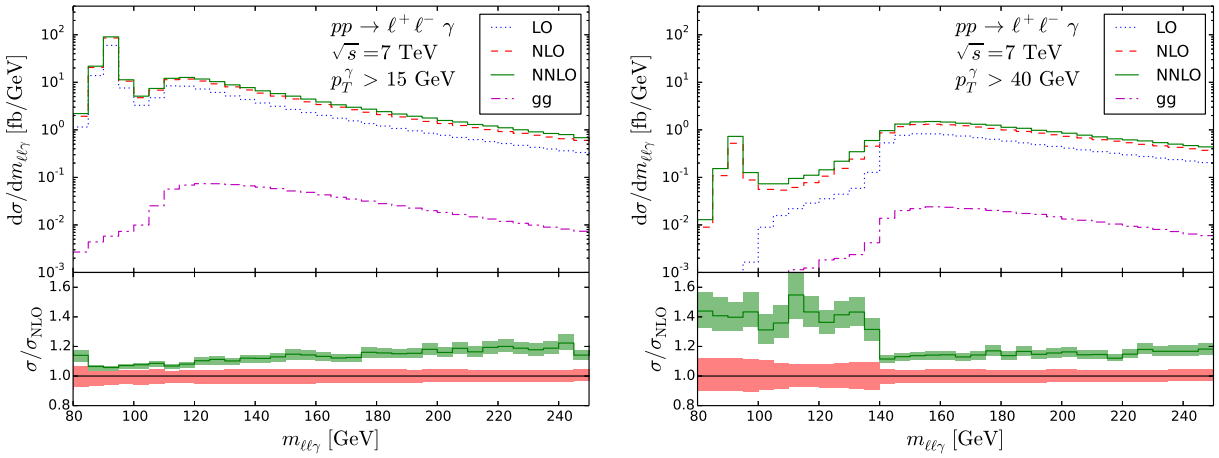

Figure 5.5: Invariant-mass distribution of the $\ell^+\ell^-\gamma$ system at LO (blue, dotted), NLO (red, dashed) and NNLO (green, solid) for the setup with $p_{\mathrm{T}}^{\gamma} > 15\,\mathrm{GeV}$ (left) and the setup with $p_{\mathrm{T}}^{\gamma} > 40\,\mathrm{GeV}$ (right). The loop-induced gluon-fusion contribution is also shown (magenta, dash-dotted). The lower panel shows the NNLO/NLO ratio, and the bands indicate theoretical uncertainty estimates from scale variations.

selection criteria are the same as in the $pp \to \ell^+\ell^-\gamma$ analysis, if applicable.

In the $\sqrt{s} = 8\,\mathrm{TeV}$ analysis, both the photon transverse-momentum and the missing transverse-momentum cuts are increased to $p_{\mathrm{T}}^{\gamma} > 130\,\mathrm{GeV}$ and $p_{\mathrm{T}}^{\nu\bar{\nu}} > 100\,\mathrm{GeV}$, respectively. As in the $Z\gamma \to \ell^+\ell^-\gamma$ analysis the rapidity acceptance for jets is slightly increased to $|\eta^{\mathrm{jet}}| < 4.5$. The cuts are summarised in Table 5.4.

The predicted cross sections at LO, NLO and NNLO can be found in Table 5.5. The results presented are summed over all three neutrino species in the final state. In the inclusive case, i.e. for $N_{\mathrm{jet}} \geq 0$, we find relatively large NLO corrections of around 57% and 68% and NNLO corrections of around 12% and 14% at $\sqrt{s} = 7\,\mathrm{TeV}$ and $\sqrt{s} = 8\,\mathrm{TeV}$, respectively. The inclusive NNLO cross section prediction at $\sqrt{s} = 7\,\mathrm{TeV}$ is in good agreement with the cross section measured by ATLAS. In the exclusive case, $N_{\mathrm{jet}} = 0$, the NNLO corrections are very small, and the scale uncertainties are reduced down to the 1% level. We observe quite a significant discrepancy with respect to the ATLAS measurement for $\sqrt{s} = 7\,\mathrm{TeV}$. Such a discrepancy, however, is not completely unexpected. First of all, as mentioned in Section 5.1.3 the stability of the fixed-order calculation when a jet veto is applied is challenged and the perturbative uncertainties we find through scale variations are likely to be underestimated.

Moreover, the $Z \to \nu\bar{\nu}$ decay implies that the final state can be identified only through the photon and the additional radiation. Hadronisation corrections, which are at the $1-2\%$ level for all the other processes studied in this section, in this case to sizeable effects for $N_{\mathrm{jet}} = 0$. The comparison of our NLO result with that quoted in Table VII of Ref. [40], which is corrected for hadronisation effects, indeed shows that in this case an $\mathcal{O}(30\%)$

	$\sqrt{s} = 7\,\text{TeV}$	$\sqrt{s} = 8\,\text{TeV}$
Neutrinos	$p_\text{T}^{\nu\bar{\nu}} > 90\,\text{GeV}$	$p_\text{T}^{\nu\bar{\nu}} > 100\,\text{GeV}$
Photon	$p_\text{T}^{\gamma} > 100\,\text{GeV}$	$p_\text{T}^{\gamma} > 130\,\text{GeV}$
	$\lvert\eta^{\gamma}\rvert < 2.37$	
	Frixione isolation with $\varepsilon_\gamma = 0.5$, $R = 0.4$, $n = 1$	
Jets	$p_\text{T}^{\text{jet}} > 30\,\text{GeV}$	
	$\lvert\eta^{\text{jet}}\rvert < 4.4$	$\lvert\eta^{\text{jet}}\rvert < 4.5$
	$N_{\text{jet}} \geq 0$ (inclusive) or $N_{\text{jet}} = 0$ (exclusive)	
Separation	$\Delta R(\gamma, \text{jet}) > 0.3$	

Table 5.4: Event selection criteria for $pp \to \nu_\ell \overline{\nu}_\ell \gamma$.

correction must be applied to the parton level theoretical prediction, thus reconciling it with the experimental result.

Fig. 5.6 shows the photon transverse-momentum and the missing transverse-momentum distributions. These distributions are identical for Born kinematics due to momentum conservation, so the difference results purely from real-radiation corrections. Above the photon transverse-momentum cut of $p_\text{T}^{\gamma} > 100\,\text{GeV}$, the difference between the two distributions is very small. Below a missing transverse momentum of 100 GeV, the cross section is only non-vanishing starting from the NLO. Fig. 5.6 shows a perturbative instability around $p_{T,\text{miss}} \approx 100$ GeV. This instability originates from the incomplete cancellation of virtual and real corrections close to the phase-space boundary (see Ref. [134] for a discussion of this phenomenon). This class of singularities is integrable and does not alter the inclusive cross section, but would require a resummed computation to achieve a reliable differential prediction close to the boundary.

We can also study the transverse-mass distribution of the $\nu\bar{\nu}\gamma$ system, defined as

$$(m_\text{T}^{\nu\nu\gamma})^2 = \left(|\vec{p}_T^{\,\gamma}| + E_T^{\text{miss}}\right)^2 - \left|\vec{p}_T^{\,\gamma} + \vec{E}_T^{\text{miss}}\right|^2 . \tag{5.2}$$

Fig. 5.7 shows the transverse-mass distribution in the inclusive (left) and exclusive case (right). Transverse masses below $m_\text{T}^{\nu\nu\gamma} \approx 200\,\text{GeV}$ are not allowed in LO kinematics and thus are only populated by real corrections starting from the NLO. This leads to an increased impact of the NNLO corrections in the region $m_\text{T}^{\nu\nu\gamma} < 200\,\text{GeV}$ in the inclusive case, with corrections of about 100% compared to the NLO prediction. When applying a jet veto, this effect vanishes almost completely, indicating that relatively hard QCD radiation is necessary to overcome the LO kinematics phase-space constraint. In fact, with a 30 GeV jet veto present, the real radiation does only populate the phase space down to $m_\text{T}^{\nu\nu\gamma} \approx 187\,\text{GeV}$ at NLO and down to $m_\text{T}^{\nu\nu\gamma} \approx 175\,\text{GeV}$ at NNLO.

$\sqrt{s}$ [TeV]		σ_{LO} [fb]	σ_{NLO} [fb]	σ_{NNLO} [fb]	σ_{ATLAS} [fb]
7	$N_{\text{jet}} \geq 0$	$78.81^{+0.3\%}_{-0.9\%}$	$123.69^{+4.1\%}_{-3.1\%}$	$138.03^{+2.5\%}_{-2.3\%}$	133 ± 13 (stat) ± 20 (syst) ± 5 (lumi)
	$N_{\text{jet}} = 0$		$88.08^{+1.2\%}_{-1.3\%}$	$86.55^{+1.0\%}_{-0.9\%}$	116 ± 10 (stat) ± 13 (syst) ± 4 (lumi)
8	$N_{\text{jet}} \geq 0$	$42.33^{+1.1\%}_{-1.5\%}$	$70.98^{+4.9\%}_{-3.9\%}$	$80.82^{+2.9\%}_{-2.7\%}$	
	$N_{\text{jet}} = 0$		$45.27^{+1.6\%}_{-1.9\%}$	$44.67^{+1.2\%}_{-1.0\%}$	

Table 5.5: $pp \to \nu_\ell \overline{\nu}_\ell \gamma$ cross sections at LO, NLO and NNLO. Scale uncertainties are evaluated as in Table 5.2. The numerical uncertainty of the NNLO prediction from statistical error and finite r_{cut} is conservatively estimated to be about 0.5%. The last column provides the corresponding result by ATLAS.

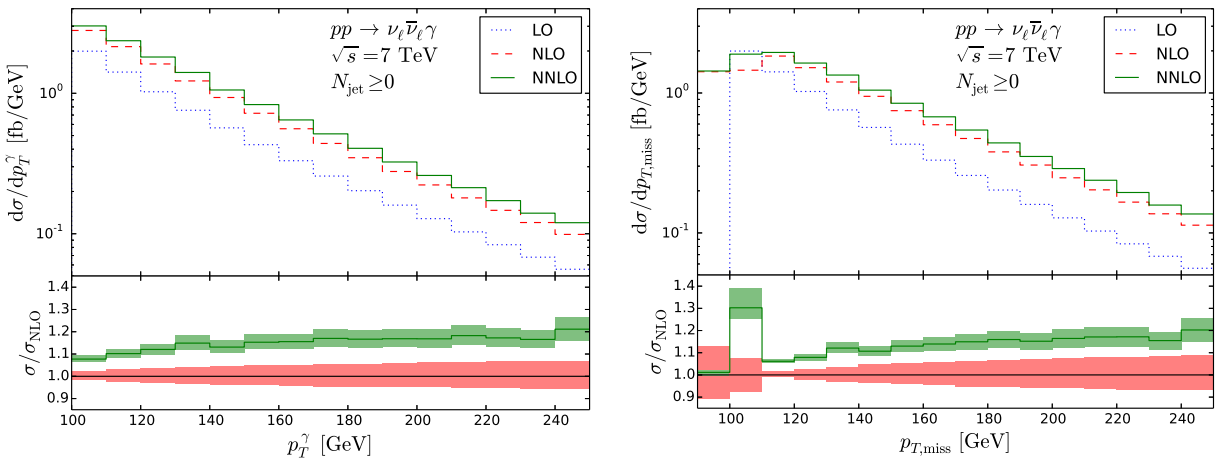

Figure 5.6: Photon transverse-momentum (left) and missing transverse-momentum (right) distribution for $pp \to \nu_\ell \overline{\nu}_\ell \gamma$ at LO (blue, dotted), NLO (red, dashed) and NNLO (green, solid). The lower panel shows the NNLO/NLO ratio, and the bands indicate theoretical uncertainty estimates from scale variations.

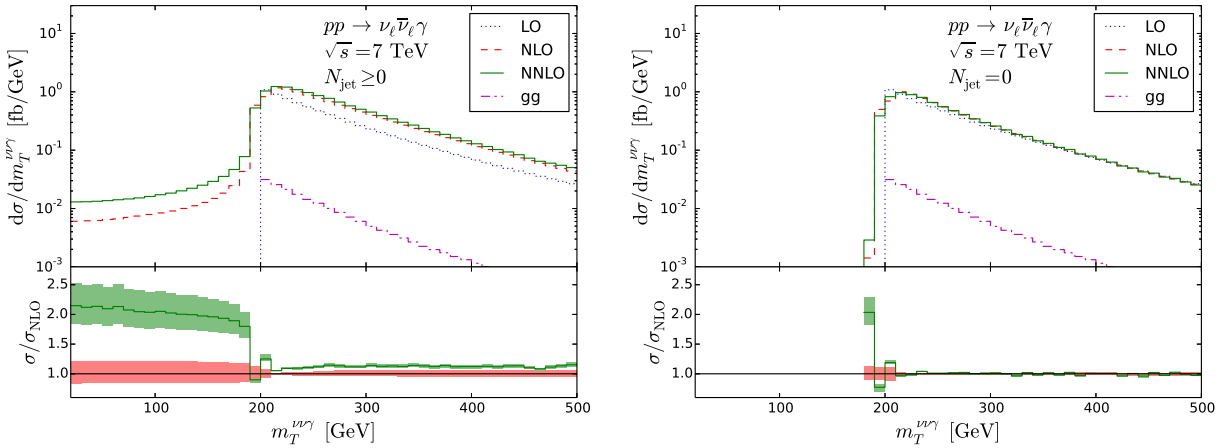

Figure 5.7: Transverse-mass distribution of the $\nu_\ell \overline{\nu}_\ell \gamma$ system in the inclusive (left) and exclusive case (right) at LO (blue, dotted), NLO (red, dashed) and NNLO (green, solid). The loop-induced gluon-fusion contribution is also shown (magenta, dash-dotted). The lower panel shows the NNLO/NLO ratio, and the bands indicate theoretical uncertainty estimates from scale variations.

Fig. 5.7 also shows the contribution from gluon fusion separately, which again is quite small and amounts to less than 2% of the fiducial cross section in the inclusive case and about 3% in the exclusive case.

5.1.5 $pp \to \ell\nu_\ell\gamma$

We now present results for $pp \to \ell\nu_\ell\gamma$ at $\sqrt{s} = 7\,\text{TeV}$ and 8 TeV. We again use the event selection criteria adopted in the ATLAS analysis [40]. This set of cuts is identical to that used in the $pp \to \ell^+\ell^-\gamma$ analysis, apart from the fact that the cut on the invariant mass of the leptons is replaced with a cut on the missing transverse momentum (which coincides with the transverse momentum of the neutrino from the W decay) of $p_T^\nu > 35\,\text{GeV}$. As in the case of $Z\gamma$ in our $\sqrt{s} = 8\,\text{TeV}$ analysis the rapidity of the jets is required to be $|\eta^{\text{jet}}| < 4.5$. A summary of all cuts and event selection criteria can be found in Table 5.6.

All results presented in the following are summed over the W charges, i.e. we combine the processes $pp \to W^+\gamma$ and $pp \to W^-\gamma$, to facilitate the comparison with experimental data. The predicted fiducial cross sections both for the inclusive and the exclusive case can be found in Table 5.7. In the inclusive case, the NLO corrections are quite large, and amount to about 136–143%. The NNLO corrections increase the NLO result by 19–20%. The impact of higher-order corrections is thus much larger than in the case of $Z\gamma$ production. We will come back to this point in Section 5.1.6.

Table 5.7 also shows the cross sections measured by ATLAS. The measurement of the inclusive cross sections shows a 2σ excess with respect to the NLO prediction, which is reduced to well below 1σ when including the NNLO corrections.

The impact of QCD corrections at NLO and NNLO is reduced to 60% and 7%, respect-

	$\sqrt{s} = 7\,\text{TeV}$	$\sqrt{s} = 8\,\text{TeV}$
Lepton	$p_\text{T}^\ell > 25\,\text{GeV}$	
	$\lvert\eta\rvert < 2.47$	
Neutrino	$p_\text{T}^\nu > 35\,\text{GeV}$	
Photon	$p_\text{T}^\gamma > 15\,\text{GeV}$ (soft p_T^γ cut) or $p_\text{T}^\gamma > 40\,\text{GeV}$ (hard p_T^γ cut)	
	$\lvert\eta^\gamma\rvert < 2.37$	
	Frixione isolation with $\varepsilon_\gamma = 0.5$, $R = 0.4$, $n = 1$	
Jets	anti-k_T algorithm with $D = 0.4$	
	$p_\text{T}^\text{jet} > 30\,\text{GeV}$	
	$\lvert\eta^\text{jet}\rvert < 4.4$	$\lvert\eta^\text{jet}\rvert < 4.5$
	$N_\text{jet} \geq 0$ (inclusive) or $N_\text{jet} = 0$ (exclusive)	
Separation	$\Delta R(\ell, \gamma) > 0.7$	
	$\Delta R(\ell/\gamma, \text{jet}) > 0.3$	

Table 5.6: $W^\pm (\to \nu_\ell \ell)\, \gamma$ cuts and event-selection criteria.

ively, when the jet veto is applied ($N_\text{jet} = 0$). As discussed in Section 5.1.3, such an effect is expected and apparently leads to a more stable perturbative prediction, but also to the possible need of more conservative procedures to estimate perturbative uncertainties. In the exclusive case, the excess of the measured fiducial cross sections over the theoretical prediction is reduced from 1.6σ to 1.2σ when going from NLO to NNLO. We note that the scale variations at NLO significantly underestimate the impact of the NNLO corrections, in particular in the inclusive case.

Fig. 5.8 shows the photon transverse-momentum distribution in comparison with the ATLAS measurement, both in the inclusive and in the exclusive case. Although the experimental uncertainties are large, the agreement between data and theory is clearly improved when including the NNLO corrections, in particular if no veto on jets is applied.

Fig. 5.9 shows the $W\gamma$ cross section differential in the transverse mass of the $\ell\nu_\ell\gamma$ system, normalised by the total fiducial cross section at the respective order. Here, the transverse mass is defined as

$$\left(m_\text{T}^{\ell\nu\gamma}\right)^2 = \left(\sqrt{m_{\ell\gamma}^2 + \left|\vec{p}_T^{\,\gamma} + \vec{p}_T^{\,\ell}\right|^2} + E_T^\text{miss}\right)^2 - \left|\vec{p}_T^{\,\gamma} + \vec{p}_T^{\,\ell} + \vec{E}_T^\text{miss}\right|^2. \tag{5.3}$$

The calculation is done with the hard photon transverse-momentum cut $p_\text{T}^\gamma > 40\,\text{GeV}$. The corresponding fiducial cross sections at LO, NLO, and NNLO are reported in Table 5.8. The impact of QCD radiative corrections is 242–260% and 26% at NLO and NNLO, respectively.

$\sqrt{s}$ [TeV]		σ_{LO} [pb]	σ_{NLO} [pb]	σ_{NNLO} [pb]	σ_{ATLAS} [pb]
7	$N_{\text{jet}} \geq 0$	$0.8726^{+6.8\%}_{-8.1\%}$	$2.058^{+6.8\%}_{-6.8\%}$	$2.453^{+4.1\%}_{-4.1\%}$	2.77 ± 0.03 (stat) ± 0.33 (syst) ± 0.14 (lumi)
	$N_{\text{jet}} = 0$		$1.395^{+5.2\%}_{-5.8\%}$	$1.493^{+1.7\%}_{-2.7\%}$	1.76 ± 0.03 (stat) ± 0.21 (syst) ± 0.08 (lumi)
8	$N_{\text{jet}} \geq 0$	$0.9893^{+7.7\%}_{-9.1\%}$	$2.401^{+7.4\%}_{-7.4\%}$	$2.884^{+4.1\%}_{-4.3\%}$	
	$N_{\text{jet}} = 0$		$1.587^{+5.5\%}_{-6.3\%}$	$1.691^{+1.8\%}_{-2.9\%}$	

Table 5.7: $W^{\pm}(\to \nu_\ell \ell)\,\gamma$ cross sections with the soft p_{T}^{γ} cut ($p_{\text{T}}^{\gamma} > 15\,\text{GeV}$). Scale uncertainties are computed as in Table 5.2. The numerical uncertainty of the NNLO prediction from statistical error and finite r_{cut} is conservatively estimated to be about 0.8%. The last column provides the measured cross sections provided by ATLAS.

$\sqrt{s}$ [TeV]		σ_{LO} [fb]	σ_{NLO} [fb]	σ_{NNLO} [fb]
7	$N_{\text{jet}} \geq 0$	$115.8^{+2.6\%}_{-3.7\%}$	$395.9^{+9.0\%}_{-7.3\%}$	$497.1^{+5.3\%}_{-4.7\%}$
8	$N_{\text{jet}} \geq 0$	$133.0^{+3.5\%}_{-4.6\%}$	$478.6^{+8.4\%}_{-7.0\%}$	$604.3^{+5.2\%}_{-4.5\%}$

Table 5.8: $W^{\pm}(\to \nu_\ell \ell)\,\gamma$ cross sections with the hard p_{T}^{γ} cut ($p_{\text{T}}^{\gamma} > 40\,\text{GeV}$). Scale uncertainties are computed as in Table 5.2. The numerical uncertainty of the NNLO prediction from statistical error and finite r_{cut} is conservatively estimated to be about 0.5%.

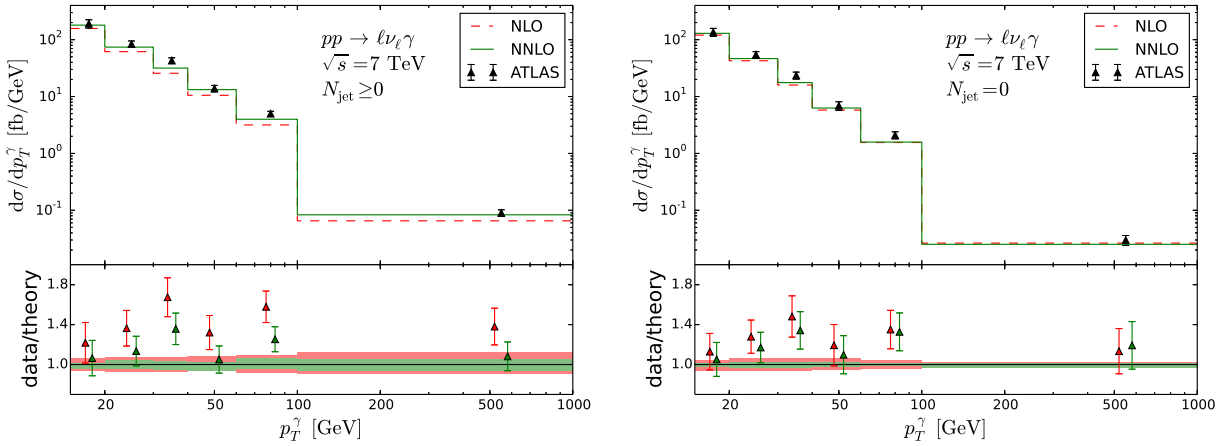

Figure 5.8: Photon transverse-momentum distribution in the inclusive (left) and exclusive case (right) at NLO (red, dashed) and NNLO (green, solid) compared to ATLAS data. In the upper panel, only experimental uncertainties are shown. The lower panel shows the data/theory ratio, and the bands indicate theoretical uncertainty estimates from scale variations.

In Fig. 5.9, due to the normalisation, the large overall corrections mostly cancel out, in particular at high transverse masses, and we observe only a slightly improved agreement with data when going from NLO to NNLO.

The increased relative impact of NLO and NNLO corrections when a harder p_{T}^γ cut ($p_{\text{T}}^\gamma > 40$ GeV) is applied can, in analogy to the $Z\gamma$ case (see Section 5.1.3), be better understood by studying the transverse-mass distributions with the soft and hard p_{T}^γ cut in more detail. The corresponding plots with a finer binning are shown in Fig. 5.10. When $p_{\text{T}}^\gamma > 15$ GeV, for Born kinematics the transverse mass has a lower bound at about $m_{\text{T}}^{\ell\nu\gamma} \gtrsim 75$ GeV, i.e. below the $W \to \ell\nu_\ell\gamma$ peak. When the photon transverse-momentum cut is increased to 40 GeV, the lower bound increases to $m_{\text{T}}^{\ell\nu\gamma} \gtrsim 100\,\text{GeV}$, and the $W \to \ell\nu_\ell\gamma$ peak is only populated by real emissions starting from the NLO, leading to large corrections in the region where the cross section is sizeable, and thus explaining the effect on the fiducial cross section.

5.1.6 The difference between $W\gamma$ and $Z\gamma$

It is interesting to compare the relative size of the NLO and NNLO corrections to the $Z\gamma$ and $W\gamma$ processes we have considered. The results are summarised in Table 5.9. It is clear that the $W\gamma$ process features much larger radiative effects compared to the $Z\gamma$ processes. This should be contrasted to the case of inclusive W and Z boson production, where QCD radiative corrections are essentially identical [135]. It is thus the emission of the additional photon that breaks the similarity between the charged current and the neutral current processes.

Restricting the analysis to NLO for the moment, the main source for the difference

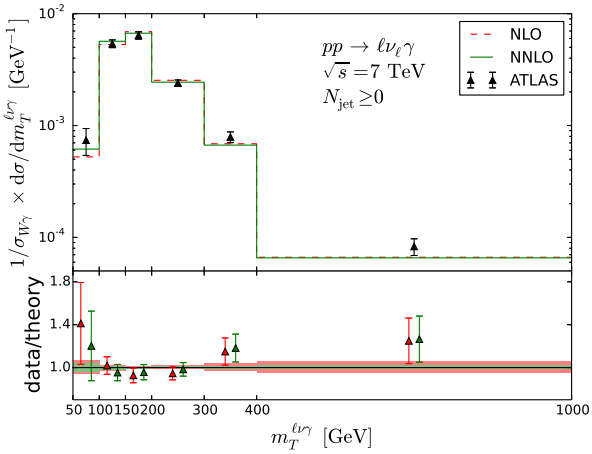

Figure 5.9: Transverse-mass distribution of the $\ell^{\pm}\nu_\ell\gamma$ system, normalised to the respective fiducial cross section at NLO (red, dashed) and NNLO (green, solid), compared to ATLAS data. In the upper panel, only experimental uncertainties are shown. The lower panel shows the data/theory ratio, and the bands indicate theoretical uncertainty estimates from scale variations.

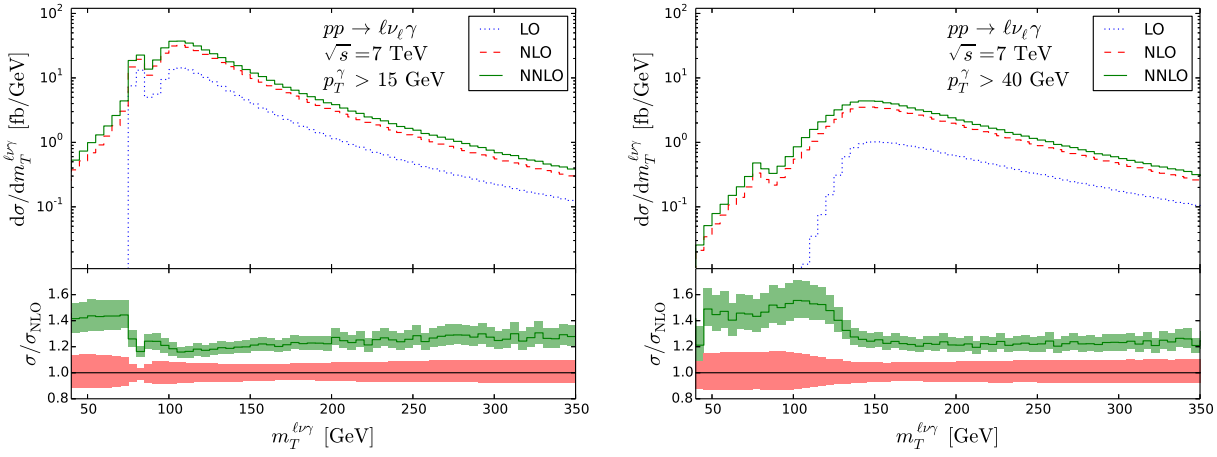

Figure 5.10: Transverse-mass distribution of the $\ell\nu_\ell\gamma$ system at LO (blue, dotted), NLO (red, dashed) and NNLO (green, solid) for $p_{\text{T}}^{\gamma} > 15$ GeV (left) and $p_{\text{T}}^{\gamma} > 40$ GeV (right), in the inclusive case ($N_{\text{jet}} \geq 0$). The lower panel shows the NNLO/NLO ratio, and the bands indicate theoretical uncertainty estimates from scale variations.

process	$p_{\mathrm{T,cut}}^{\gamma}$	$\sqrt{s}$ [TeV]	N_{jet}	$\sigma_{\mathrm{NLO}}/\sigma_{\mathrm{LO}}$	$\sigma_{\mathrm{NNLO}}/\sigma_{\mathrm{NLO}}$
$Z\,(\to \ell^+\ell^-)\,\gamma$	soft	7	$N_{\mathrm{jet}} \geq 0$	+50%	+8%
			$N_{\mathrm{jet}} = 0$	+27%	+3%
		8	$N_{\mathrm{jet}} \geq 0$	+50%	+8%
			$N_{\mathrm{jet}} = 0$	+25%	+3%
	hard	7	$N_{\mathrm{jet}} \geq 0$	+79%	+17%
		8	$N_{\mathrm{jet}} \geq 0$	+82%	+18%
$Z\,(\to \nu_l\overline{\nu}_l)\,\gamma$		7	$N_{\mathrm{jet}} \geq 0$	+57%	+12%
			$N_{\mathrm{jet}} = 0$	+12%	−2%
		8	$N_{\mathrm{jet}} \geq 0$	+68%	+14%
			$N_{\mathrm{jet}} = 0$	+7%	−1%
$W\,(\to \ell\nu_\ell)\,\gamma$	soft	7	$N_{\mathrm{jet}} \geq 0$	+136%	+19%
			$N_{\mathrm{jet}} = 0$	+60%	+7%
		8	$N_{\mathrm{jet}} \geq 0$	+143%	+20%
			$N_{\mathrm{jet}} = 0$	+60%	+7%
	hard	7	$N_{\mathrm{jet}} \geq 0$	+242%	+26%
		8	$N_{\mathrm{jet}} \geq 0$	+260%	+26%

Table 5.9: Summary of the relative NLO and NNLO corrections in the channels under investigation, $Z\,(\to \ell^+\ell^-)\,\gamma$, $Z\,(\to \nu_\ell\overline{\nu}_\ell)\,\gamma$, and $W^{\pm}\,(\to \ell^{\pm}\bar{\nu}_\ell)\,\gamma$. Numbers are reported for both soft and hard p_{T}^{γ} cuts.

between $Z\gamma$ and $W\gamma$ can be traced back to the gq and $g\overline{q}$ channels, which contribute a moderate, negative amount to the cross section in $Z\gamma$ production, but are large and positive for $W^{\pm}\gamma$. It turns out that this effect is driven by resonant $W\gamma$ contributions to the cross section, i.e. by $pp \to W(\to \ell\nu_\ell)\gamma$ topologies, and not by $pp \to W \to \ell(\to \ell\gamma)\nu_\ell$ topologies, where the photon is emitted from the final-state lepton. These two contributions can only be separated in a gauge-invariant way if the W bosons are treated as on-shell particles, i.e. in a narrow-width approximation. By studying the LO contributions to the $Z\gamma$ and $W\gamma$ cross sections (see Fig. 5.1 and Fig. 5.2) it turns out that in $W\gamma$ there is an additional Feynman diagram in which the photon is radiated off the W boson (see Fig. 5.2d). This additional diagram is responsible for a *radiation zero* [136], an exact zero present in the on-shell partonic $W\gamma$ tree-level amplitude at $\cos\theta^* = 1/3$, where θ^* is the scattering angle in the centre-of-mass frame. This radiation zero gets diluted by the convolution with the parton densities and by off-shell effects, but it is responsible for the suppression of the Born-level $W\gamma$ cross section with respect to $Z\gamma$. Real radiation appearing at NLO breaks the radiation zero, and thus the relative impact of higher-order corrections is significantly increased.

To quantitatively test this effect we consider the $pp \to \ell\nu_\ell\gamma$ and $pp \to \ell^+\ell^-\gamma$ processes studied in Section 5.1.3 and Section 5.1.5, with the same selection cuts. Contrary to what was done in the previous sections we disable the contributions from final-state radiation and use the narrow-width approximation. In Fig. 5.11 (left) we plot the distribution in the rapidity difference $\Delta y_{\ell\gamma}$ between the charged lepton and the photon [137].

We see that the LO distribution shows a pronounced dip at central rapidities. Although diluted by the convolution with the parton densities, the dip is clearly visible, and is responsible for the suppression of the $W\gamma$ cross section. Since real radiation does not respect the radiation zero, the dip is filled up by radiative corrections. Roughly speaking, the NLO is a *de facto* LO prediction in the region of the dip and the NNLO corrections are thus relatively large as well. In contrast to $W\gamma$, the $Z\gamma$ amplitude does not exhibit a radiation zero, and no dip appears in the rapidity-difference distribution, as can be seen in Fig. 5.11 (right).

The presence of the radiation zero, and of the corresponding dip in the $\Delta y_{\ell\gamma}$ distribution, are thus the reason for the increased importance of radiative corrections to the $W\gamma$ processes.

5.2 ZZ production

The production of a ZZ pair is an important benchmark process at the LHC. As its final state can be fully reconstructed, it can be measured very precisely. Measurements of the ZZ cross section can be used to constrain potential anomalous triple gauge couplings. It is also important as an irreducible background in Higgs boson measurements and BSM resonance searches.

The first NLO computation for the production of a stable Z pair appeared more than 20 years ago (see Ref. [138, 139]). The decay, neglecting spin correlations, was added

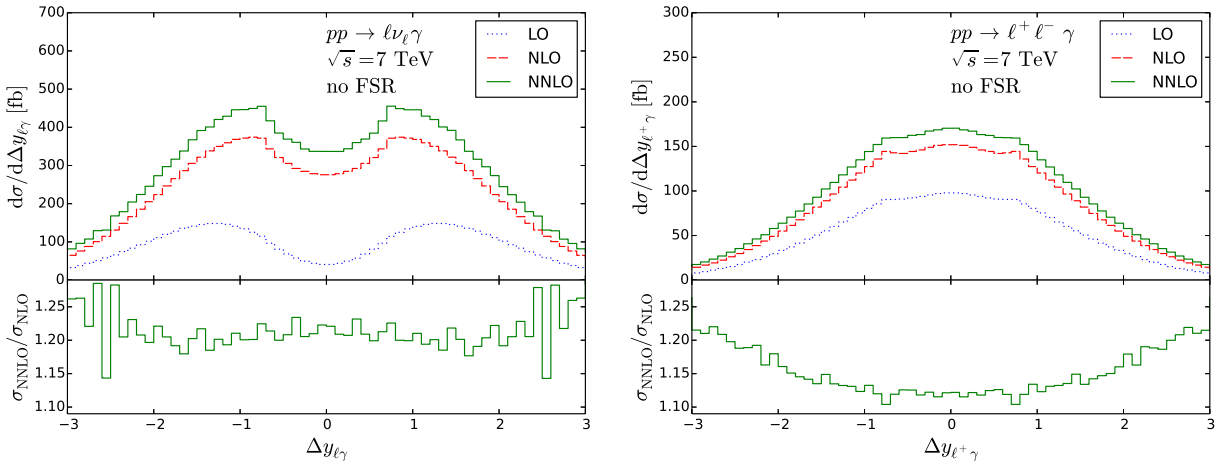

Figure 5.11: Rapidity difference between the charged lepton and the photon for $W\gamma$ (left) and $Z\gamma$ production (right) at LO (blue, dotted), NLO (red, dashed) and NNLO (green, solid). The lower panel shows the NNLO/NLO ratio. Final-state radiation has been disabled for these plots.

in Ref. [140] and the full NLO correction including off-shell effects was completed in Refs. [141, 142] using the one-loop helicity amplitudes from Ref. [143]. As for $Z\gamma$ production, the loop-induced gluon-fusion contribution $gg \to ZZ$ is a finite and gauge invariant contribution entering formally at NNLO. It was first computed in Ref. [144, 145] and supplemented with the leptonic decays in Refs. [146–148]. The full NLO computation, including the gluon-fusion contribution, is implemented in MCFM [120]. Electroweak corrections were computed in Ref. [149].

In the following, we first discuss the computation of NNLO corrections to the production of an on-shell pair of Z bosons, initially presented in Ref. [27]. We then review the first results for the process $pp \to 4$ leptons, where we include off-shell effects and spin correlations as well as all possible interference contributions at NNLO QCD accuracy. These results were first presented in Ref. [37].

5.2.1 The inclusive on-shell cross section

(a) Topology Ia

(b) Topology Ib

Figure 5.12: Feynman diagrams contributing to ZZ production at Born level.

The Feynman diagrams contributing to the on-shell ZZ cross section at LO are shown in Fig. 5.12. We use $G_F = 1.16639 \times 10^{-5}\,\text{GeV}^{-2}$, $m_W = 80.399\,\text{GeV}$ and $m_Z = 91.1876\,\text{GeV}$ for the electroweak parameters. The top-quark mass $m_t = 173.2\,\text{GeV}$ and the Higgs boson mass $m_H = 125\,\text{GeV}$ only enter through the loop-induced gluon-fusion contribution. We use the MSTW2008 sets of parton distributions and consider $N_f = 5$ massless flavours. The central renormalisation and factorisation scales μ_R and μ_F are set to m_Z. Scale uncertainties are computed by varying the scales independently in the range $0.5\,m_Z < \mu_R,\, \mu_F < 2\,m_Z$ with the constraint $0.5 < \mu_R/\mu_F < 2$.

Fig. 5.13 and Table 5.10 show the total cross section at LO, NLO and NNLO as a function of the hadronic centre-of-mass energy. The NLO corrections increase the LO result by about 45%. The NNLO corrections amount to 11%–17% of the NLO cross section, depending on the centre-of-mass energy and significantly exceed the uncertainty band from scale variations at NLO. The combination of the NLO cross section with the gluon-fusion α_S^2 contribution is also shown in Fig. 5.13. Gluon fusion alone contributes about 60% of the NNLO corrections. The scale uncertainties stay at the ±3% level when going from NLO to NNLO, though they are dominated by the gluon-fusion contribution, which is only included at LO and thus comes with large scale uncertainties.

Fig. 5.13 also shows the cross sections measured by ATLAS and CMS. They are, however, included only for illustrative purposes. They cannot be directly compared to our inclusive computation, because in the experiments a cut on the invariant mass of the lepton pairs in the final state is applied to eliminate contributions from off-shell Z bosons and photons. Since in our on-shell computation the Z bosons are always on their mass shell, we cannot implement the experimental cut. Extrapolating from NLO, we can expect the theoretical cross sections to be reduced by $\sim 4\%$ when going from the on-shell to the off-shell case and implementing the experimental mass cuts.

In the meantime, the computation of the inclusive NNLO cross section can for example be used in the Higgs boson width measurement using off-shell $H^* \to ZZ$ events. This approach exploits the fact that many of the experimental uncertainties cancel out when measuring the Higgs boson production cross section both in the on-shell and in the far off-shell region and taking the ratio [154, 155]. The result is proportional to the Higgs width Γ_H:

$$\frac{\sigma^{gg\to H\to ZZ}_{\text{off-shell}}}{\sigma^{gg\to H\to ZZ}_{\text{on-shell}}} \sim \Gamma_H. \tag{5.4}$$

ZZ production is part of the irreducible background, and in the off-shell region our computation has been used in the ATLAS analysis in Ref. [156]. ATLAS reports an upper limit on the Higgs boson width of $\Gamma_H/\Gamma_H^{\text{SM}} < 5.7$ at 95% confidence level.

5.2.2 The fiducial cross section

Using the off-shell helicity amplitudes from Ref. [22], we now present first results for the $ZZ \to 4\,\text{leptons}$ process at NNLO, including off-shell effects and spin correlations. We

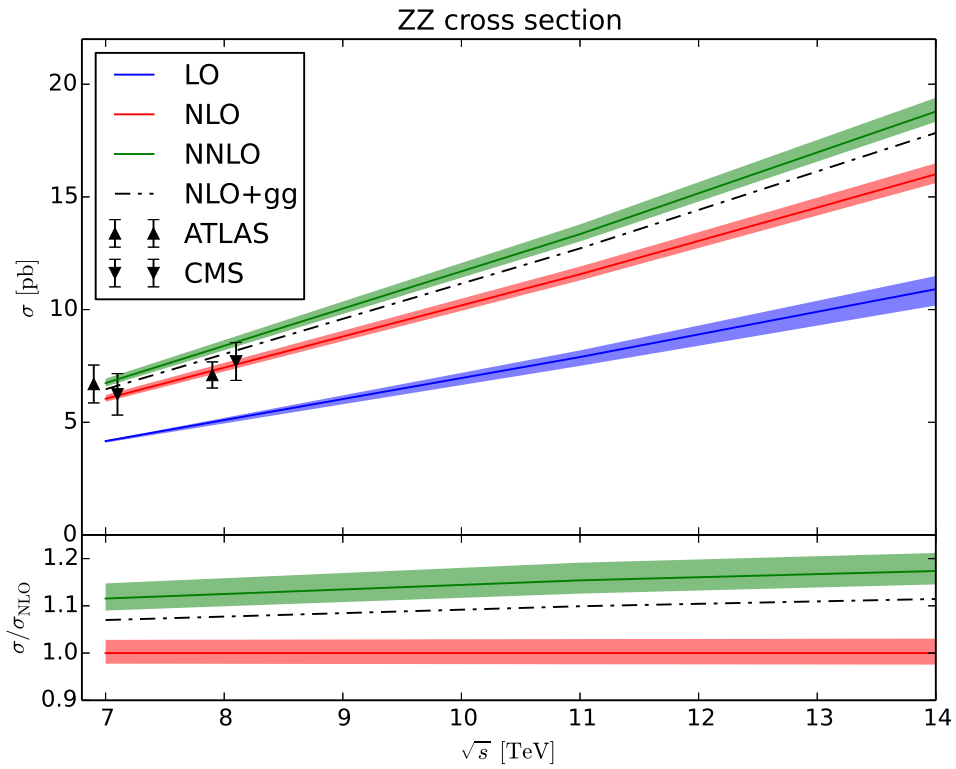

Figure 5.13: ZZ cross section at LO (blue), NLO (red), NLO+gg (black, dash-dotted) and NNLO (green) as a function of $\sqrt{s}$. The ATLAS and CMS experimental results at $\sqrt{s} = 7$ TeV and $\sqrt{s} = 8$ TeV are also shown for comparison [150–153]. The lower panel shows the NNLO and NLO+gg results normalised to the NLO prediction. The bands describe scale variations.

$\sqrt{s}$ (TeV)	$\sigma_{\rm LO}$ (pb)	$\sigma_{\rm NLO}$ (pb)	$\sigma_{\rm NNLO}$ (pb)
7	$4.167^{+0.7\%}_{-1.6\%}$	$6.044^{+2.8\%}_{-2.2\%}$	$6.735^{+2.9\%}_{-2.3\%}$
8	$5.060^{+1.6\%}_{-2.7\%}$	$7.369^{+2.8\%}_{-2.3\%}$	$8.284^{+3.0\%}_{-2.3\%}$
9	$5.981^{+2.4\%}_{-3.5\%}$	$8.735^{+2.9\%}_{-2.3\%}$	$9.931^{+3.1\%}_{-2.4\%}$
10	$6.927^{+3.1\%}_{-4.3\%}$	$10.14^{+2.9\%}_{-2.3\%}$	$11.60^{+3.2\%}_{-2.4\%}$
11	$7.895^{+3.8\%}_{-5.0\%}$	$11.57^{+3.0\%}_{-2.4\%}$	$13.34^{+3.2\%}_{-2.4\%}$
12	$8.882^{+4.3\%}_{-5.6\%}$	$13.03^{+3.0\%}_{-2.4\%}$	$15.10^{+3.2\%}_{-2.4\%}$
13	$9.887^{+4.9\%}_{-6.1\%}$	$14.51^{+3.0\%}_{-2.4\%}$	$16.91^{+3.2\%}_{-2.4\%}$
14	$10.91^{+5.4\%}_{-6.7\%}$	$16.01^{+3.0\%}_{-2.4\%}$	$18.77^{+3.2\%}_{-2.4\%}$

Table 5.10: Inclusive cross section for ZZ production at the LHC at LO, NLO and NNLO with $\mu_F = \mu_R = m_Z$. The uncertainties are obtained by varying the renormalisation and factorisation scales in the range $0.5m_Z < \mu_R, \mu_F < 2m_Z$ with the constraint $0.5 < \mu_F/\mu_R < 2$.

note that the notation $ZZ \to 4$ leptons is slightly misleading. In fact, we consider the process $pp \to 4$ leptons, which includes contributions from $Z\gamma^*$ and $\gamma^*\gamma^*$ (see Fig. 5.14 for the corresponding Feynman diagrams) as well as singly-resonant contributions from $pp \to Z/\gamma^* \to 4$ leptons (see Fig. 5.15 for the Feynman diagrams).

We consider pp collisions with $\sqrt{s} = 8$ TeV. For the electroweak couplings we again use the G_μ scheme. More precisely, consistent with the OpenLoops implementation, we use the complex W and Z boson masses to define the EW mixing angle as $\cos\theta_W^2 = (m_W^2 - i\Gamma_W m_W)/(m_Z^2 - i\Gamma_Z m_Z)$. In particular, we use the values $G_F = 1.16639 \times 10^{-5}$ GeV^{-2}, $m_W = 80.399$ GeV, $\Gamma_W = 2.1054$ GeV, $m_Z = 91.1876$ GeV, $\Gamma_Z = 2.4952$ GeV. For the top quark we use $m_t = 173.2$ GeV, $\Gamma_t = 1.4426$ GeV, and for the Higgs boson $m_H = 125$ GeV, $\Gamma_H = 4.07$ MeV. Both the top quark and the Higgs boson only appear in diagrams with closed top-quark loops, thus entering the gluon-fusion channel and the real–virtual contribution.[2] We use the NNPDF3.0 [53] sets of parton distributions with $\alpha_{\rm S}(m_Z) = 0.118$, and the $\alpha_{\rm S}$ running is evaluated at each corresponding order (i.e., we use $(n+1)$-loop $\alpha_{\rm S}$ at N^{n}LO, with $n = 0, 1, 2$). We consider $N_f = 5$ massless quark flavours. The central renormalisation and factorisation scales are set to $\mu_R = \mu_F = m_Z$.

We first consider the ATLAS analysis of Ref. [152] in the three decay channels $e^+e^-e^+e^-$, $\mu^+\mu^-\mu^+\mu^-$, and $e^+e^-\mu^+\mu^-$. The invariant masses of the two reconstructed lepton pairs are required to fulfil the condition 66 GeV $\leq m_{\ell\ell} \leq$ 116 GeV. In the case of two lepton

[2]The Higgs boson contributes less than 1% to the loop-induced $gg \to ZZ$ cross section, whereas its effect on the real–virtual contribution is numerically negligible.

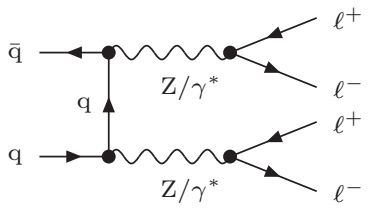

(a) Topology Ia

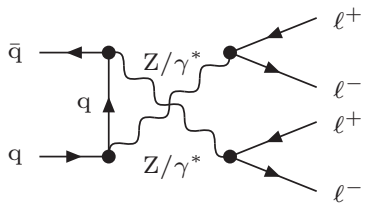

(b) Topology Ib

Figure 5.14: Doubly-resonant Feynman diagrams contributing to pp → 4 leptons at Born level.

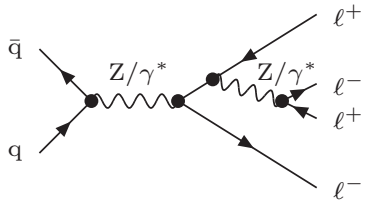

(a) Topology IIa

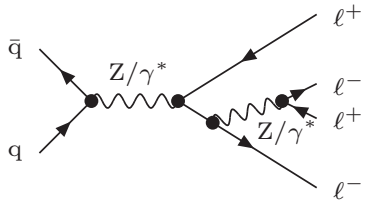

(b) Topology IIb

Figure 5.15: Singly-resonant Feynman diagrams contributing to pp → 4 leptons at Born level.

pairs with the same flavours there is a pairing ambiguity, which is resolved by choosing the pairing that makes the sum of the absolute distances from m_Z smaller. The leptons are required to have $p_T \geq 7$ GeV and rapidity $|\eta| \leq 2.7$. For any lepton pair we require $\Delta R(\ell, \ell') > 0.2$, independently of the flavours and charges of ℓ and ℓ'.

The corresponding cross sections are reported in Table 5.11, where the ATLAS results are also shown. The uncertainties on our theoretical predictions are obtained by varying the renormalisation and factorisation scales in the range $0.5m_Z < \mu_R, \mu_F < 2m_Z$ with the constraint $0.5 < \mu_F/\mu_R < 2$. Independently of the leptonic decay channels, the NNLO corrections increase the NLO result by about 15%, similarly to what was found for the inclusive cross section for on-shell ZZ production, see Section 5.2.1 and Ref. [27]. This is as expected because the selection cuts are mild and do not significantly alter the impact of radiative corrections. The scale uncertainties are about ±3% at NLO and remain of the same order at NNLO. As noted for the inclusive cross section, the NLO scale uncertainty does not cover the NNLO effect. This is not surprising since the loop-induced gluon-fusion contribution, which provides $\sim 60\%$ of the $\mathcal{O}(\alpha_S^2)$ correction, opens up only at NNLO.

The NNLO corrections improve the agreement of the theoretical prediction with the data for the $e^+e^-\mu^+\mu^-$ channel, whereas they deteriorate the agreement in the case of the $4e$ and 4μ channels. We note, however, that the predicted fiducial cross sections are still

consistent with the ATLAS measurements at the 1σ level within the statistics-dominated uncertainties.

Channel	$\sigma_{\rm LO}$ (fb)	$\sigma_{\rm NLO}$ (fb)	$\sigma_{\rm NNLO}$ (fb)	$\sigma_{\rm exp}$ (fb)
$e^+e^-e^+e^-$	$3.547(1)^{+2.9\%}_{-3.9\%}$	$5.047(1)^{+2.8\%}_{-2.3\%}$	$5.79(2)^{+3.4\%}_{-2.6\%}$	$4.6^{+0.8}_{-0.7}(\text{stat})^{+0.4}_{-0.4}(\text{syst.})^{+0.1}_{-0.1}(\text{lumi.})$
$\mu^+\mu^-\mu^+\mu^-$				$5.0^{+0.6}_{-0.5}(\text{stat})^{+0.2}_{-0.2}(\text{syst.})^{+0.2}_{-0.2}(\text{lumi.})$
$e^+e^-\mu^+\mu^-$	$6.950(1)^{+2.9\%}_{-3.9\%}$	$9.864(2)^{+2.8\%}_{-2.3\%}$	$11.31(2)^{+3.2\%}_{-2.5\%}$	$11.1^{+1.0}_{-0.9}(\text{stat})^{+0.5}_{-0.5}(\text{syst.})^{+0.3}_{-0.3}(\text{lumi.})$

Table 5.11: Fiducial cross sections and scale uncertainties for ATLAS cuts at LO, NLO, and NNLO in the three considered leptonic decay channels. The ATLAS data are also shown.

Secondly, we consider the CMS analysis of Ref. [157]. The fiducial region is defined as follows: all muons are required to fulfil $p_T^\mu > 5$ GeV, $|\eta^\mu| < 2.4$, while all electrons are required to fulfil $p_T^e > 7$ GeV, $|\eta^e| < 2.5$. In addition, the leading- and subleading-lepton transverse momenta must satisfy $p_T^{\ell,1} > 20$ GeV and $p_T^{\ell,2} > 10$ GeV, respectively. In the case of two lepton pairs with the same flavours, the pairing ambiguity is resolved by choosing the pair with the smallest distance from m_Z. This pair is called Z_1, the remaining pair is called Z_2. The invariant masses of the two reconstructed lepton pairs are required to fulfil $60\text{ GeV} \leq m_{\ell\ell} \leq 120$ GeV. We note that in the case of identical flavours this definition of the fiducial region does not prevent the invariant masses of the other two possible lepton pairs from becoming arbitrarily small, giving rise to a collinear $\gamma^* \to \ell^-\ell^+$ singularity. To avoid that, we follow CMS and add an additional cut $m_{\ell\ell} > 4$ GeV on all lepton pairs of the same flavours and opposite charges. The corresponding fiducial cross sections and scale uncertainties, computed as above, are reported in Table 5.12. Like for the ATLAS analysis, the NNLO corrections increase the NLO fiducial cross section by about 15%. The scale uncertainties are similar to those reported in Table 5.11.

Channel	$\sigma_{\rm LO}$ (fb)	$\sigma_{\rm NLO}$ (fb)	$\sigma_{\rm NNLO}$ (fb)
$e^+e^-e^+e^-$	$3.149(1)^{+3.0\%}_{-4.0\%}$	$4.493(1)^{+2.8\%}_{-2.3\%}$	$5.16(1)^{+3.3\%}_{-2.6\%}$
$\mu^+\mu^-\mu^+\mu^-$	$2.973(1)^{+3.1\%}_{-4.1\%}$	$4.255(1)^{+2.8\%}_{-2.3\%}$	$4.90(1)^{+3.4\%}_{-2.6\%}$
$e^+e^-\mu^+\mu^-$	$6.179(1)^{+3.1\%}_{-4.0\%}$	$8.822(1)^{+2.8\%}_{-2.3\%}$	$10.15(2)^{+3.3\%}_{-2.6\%}$

Table 5.12: Fiducial cross sections and scale uncertainties for CMS cuts at LO, NLO, and NNLO in the three considered leptonic decay channels.

CMS does not report the fiducial cross sections corresponding to the above cuts, but only normalised distributions, to which we compare our results. We start with the invariant-

mass distribution of the four leptons, which is depicted in Fig. 5.16. The lower panels show the theory/data comparison, and the NNLO result normalised to the central NLO prediction. We see that the NNLO corrections have a limited impact in the comparison with the data, which still have large uncertainties. The NNLO effects on the normalised distribution are relatively small: they are completely negligible at low invariant masses, and they increase to -5% in the high-mass region. This means that the NNLO corrections make the invariant mass distribution slightly softer. We have checked that this effect is due to the gluon-fusion contribution, whose relative effect decreases at high masses, due to the larger values of Bjorken x that are probed. The NLO (NNLO) scale uncertainties range from about $\pm 2\%$ ($\pm 1\%$) at low m_{ZZ} to $\pm 4\%$ ($\pm 2\%$) at high m_{ZZ}.

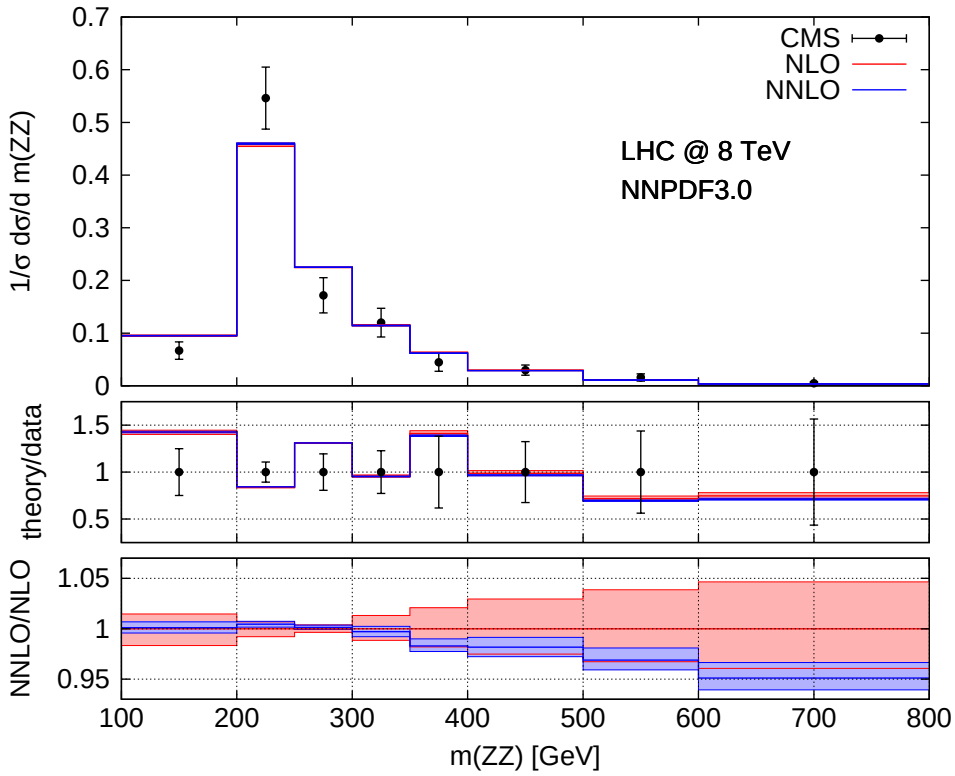

Figure 5.16: The four-lepton invariant-mass distribution at NLO and NNLO compared to the CMS data. In the lower panels the ratio of our theoretical results over the data, and the NNLO result normalised to the central NLO prediction are presented. The bands correspond to scale variations as described in the text.

In Fig. 5.17 we show the analogous results for the leading-lepton p_T distribution (left) and the azimuthal separation ($\Delta\Phi$) of the two Z candidates (right). As in Fig. 5.16, we see that the NNLO effects on the p_T distribution do not change the comparison with the data in a significant way. The NNLO corrections are also relatively small in most of the range of p_T considered, except for the low p_T region, where they increase significantly. This effect is due to the gluon-fusion contribution, whose relative impact increases as p_T

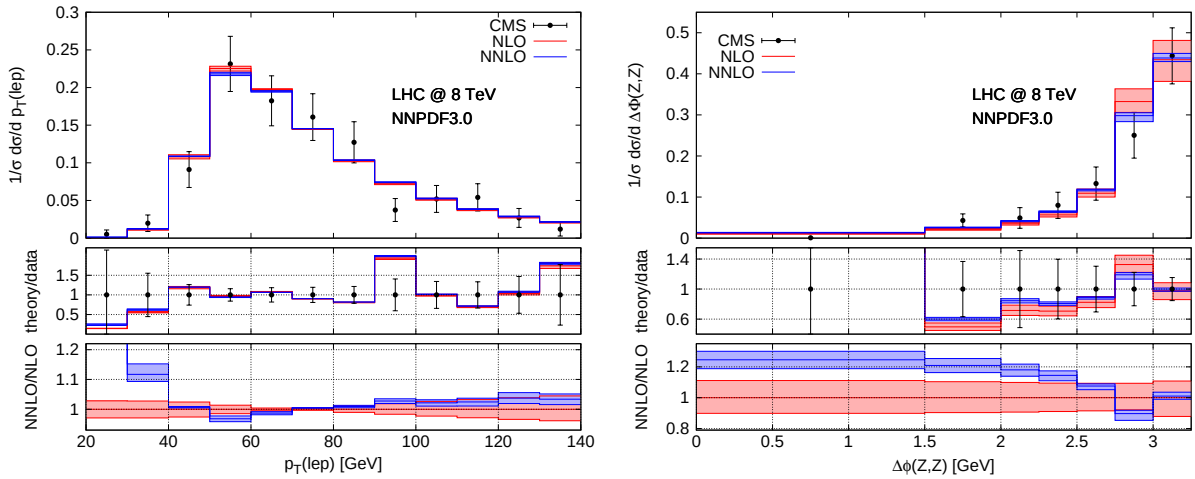

Figure 5.17: The leading-lepton p_T (left) and the $\Delta\phi$ (right) distributions at NLO and NNLO compared to the CMS data. In the lower panels the ratio of our theoretical results over the data, and the NNLO result normalised to the central NLO prediction are presented. The bands correspond to scale variations as described in the text.

decreases. The situation is different for the $\Delta\Phi$ distribution. Here the NNLO corrections improve the agreement with the data, except for the first bin, where the CMS measurement is an order of magnitude below the theoretical NNLO prediction. The larger impact of NNLO corrections in the $\Delta\Phi$ distribution can be understood easily by the observation that at LO the reconstructed Z bosons are always back-to-back, i.e., $\Delta\Phi(Z_1, Z_2) = \pi$. As a consequence, the NNLO calculation is effectively NLO in the region $0 \leq \Delta\Phi < \pi$. The NNLO corrections amount to about $+25\%$ when $\Delta\Phi \lesssim 1.5$, and decrease as $\Delta\Phi$ increases. We note that this effect is entirely due to the NNLO corrections to the $q\bar{q}$ channel addressed in this paper, since the loop-induced gluon-fusion contribution, which also enters at NNLO, affects the $\Delta\Phi$ distribution only at $\Delta\Phi = \pi$. The NLO scale uncertainties are about $\pm 11\%$, while at NNLO the uncertainties are about $\pm 5\%$ at low $\Delta\Phi$, and decrease to about $\pm 2\%$ at high $\Delta\Phi$.

5.3 W^+W^- production

Just as ZZ production, W^+W^- production is interesting both as a Standard Model test and as a background process in new physics searches. It however takes a somewhat special role among the diboson production processes in having a larger cross section than ZZ production and, after the leptonic decay, a more challenging final state with $W^+W^- \to \ell^+\nu\ell^-\bar{\nu}_\ell$. Due to the presence of two neutrinos, the final state cannot be reconstructed completely. The presence of a large top background from $t\bar{t} \to W^+W^-b\bar{b}$ further complicates the experimental measurement, requiring strict selection cuts which in turn prove challenging for

	measured	SM NLO
ATLAS 7 TeV	51.9 ± 4.8	$44.7^{+2.1}_{-1.9}$
CMS 7 TeV	52.4 ± 5.1	
ATLAS 8 TeV	71.4 ± 5.3	$57.3^{+2.4}_{-1.6}$
CMS 8 TeV	69.9 ± 7.0	

Table 5.13: Inclusive W^+W^- production cross sections in picobarn measured at the LHC compared to the SM NLO predictions.

the theoretical modelling of the process.

NLO predictions for the production of a stable W pair first appeared in Refs. [158, 159]. Spin correlations and off-shell effects were taken into account in Refs. [141, 142] after the computation of the one-loop helicity amplitudes in Ref. [143]. The gluon-fusion contribution $gg \to W^+W^-$ was computed in Refs. [145, 160] and supplemented by the leptonic decay in Refs. [161, 162]. The full NLO QCD corrections and the (formally NNLO) gluon-fusion contribution is implemented in MCFM [120]. Electroweak corrections were presented in Refs. [163–165]. Beyond fixed order, transverse-momentum [166–169] (see also Section 5.4), jet veto [170] and threshold [171] resummation have been studied.

The Born-level diagrams for the production of an on-shell W^+W^- pair are shown in Fig. 5.18.

The W^+W^- production cross section has been measured at the Tevatron [172, 173] and the LHC [41–44]. The LHC measurements of the inclusive cross section are, together with the reference NLO prediction (including the gluon-fusion contribution), summarised in Table 5.13. The ATLAS measurement at 8 TeV exceeds the theoretical prediction by more than two standard deviations, which has triggered extensive discussions, both about possible new physics explanations [174] and about shortcomings in the theoretical description [175].

(a) Topology Ia (b) Topology Ib

Figure 5.18: Feynman diagrams contributing to W^+W^- production at Born level.

One of the dominant theoretical uncertainties however was the missing NNLO QCD correction, which we first presented in Ref. [28]. The computation of NNLO corrections to W^+W^- production parallels the one for NNLO corrections to ZZ productions, except for one important complication. This complication comes from the presence of (massless)

b-quarks in the final state of the real-radiation contributions when performing the computation in a five flavour scheme (5FS). At NLO, the real correction contains processes of the form $gb \to W^+W^-b$, in which an initial state gluon splits into a $b\bar{b}$ pair. The exact same final state however results from the production of an intermediate on-shell top quark, which then decays into a W and a b-quark, $gb \to tW^- \to W^+W^-b$, see Fig. 5.19 for the relevant diagrams. This implies that the NLO W^+W^- cross section is contaminated by LO Wt production, which amounts to 30 (60)% of the LO W^+W^- cross section at 7 (14) TeV. At NNLO, the contamination becomes even more severe: the double-real correction involves processes of the form $gg/q\bar{q} \to W^+W^-b\bar{b}$, in which a $b\bar{b}$ pair is produced by QCD radiation from the initial state. However, production of an intermediate on-shell $t\bar{t}$ pair, $gg/q\bar{q} \to t\bar{t} \to W^+W^-b\bar{b}$, produces the exact same final state; see Fig. 5.20 for some relevant diagrams. The resonant $t\bar{t}$ contributions amounts to about 300 (700)% of the LO cross section at 7 (14) TeV.

(a) Non-resonant contribution. (b) Resonant contribution.

Figure 5.19: Feynman diagrams contributing to the $gb \to W^+W^-b$ subprocess.

(a) Non-resonant contribution. (b) Resonant contribution.

Figure 5.20: Feynman diagrams contributing to the $u\bar{u} \to W^+W^-b\bar{b}$ subprocess.

This contamination clearly calls for a theoretical definition of the W^+W^- cross section in which the top-quark contributions are consistently subtracted. Defining such a subtraction is however far from trivial: simply discarding the problematic subcontributions would lead to a non-cancellation of the collinear $g \to b\bar{b}$ singularity. On the other hand, the top

quark does not decouple in the limit $m_t \to \infty$, so also removing the single and double top diagrams is not possible in a consistent way.

One viable option to remove the top contaminations is to work in a four flavour scheme (4FS), that is to introduce a physical b-mass and work consistently with $N_f = 4$ light flavours. The $g \to b\bar{b}$ splitting becomes collinearly finite and all partonic channels involving a bottom quark in the initial or in the final state can be removed. While this provides a theoretically clean definition of the inclusive W^+W^- cross section, neglecting all bottom quarks as external particles a priori is somewhat unsatisfactory in a precision calculation, and an alternative subtraction procedure to quantify the inherent theoretical ambiguities of the prescription is desirable.

Experimentally, the top-quark background is suppressed by applying a jet veto, where the veto threshold is of the order of $\sim 25\,\text{GeV}$. The remaining top contamination is then subtracted and the result extrapolated to a total W^+W^- cross section. Theoretically, applying a b-jet veto would be better motivated. However, a veto threshold around $p_{T,\,\text{b-jet}}^{\text{veto}} = 30\,\text{GeV}$ still leaves a remaining top contamination of around 10%. The limit $p_{T,b-\text{jet}}^{\text{veto}} \to 0$ cannot be taken due to the presence of a logarithmic singularity.

However, we can adopt a subtraction procedure similar to the one in Refs. [78, 176], that is to exploit the characteristic scaling behaviour of the $t\bar{t}$, Wt and top-free W^+W^- contributions to the cross section with respect to the top width Γ_t. Double (single) resonant top production is enhanced by $1/\Gamma_t^2$ ($1/\Gamma_t$) for small Γ_t, while the top-free contribution to the W^+W^- cross section should stay constant.

Turning this observation around, it can be used to define a top-free W^+W^- cross section by the following procedure: we repeatedly compute the full NNLO cross section in the 5FS for different values of Γ_t to obtain the cross section σ as a function of $x \equiv \Gamma_t/\Gamma_t^{\text{phys}}$. Fig. 5.21 shows $x^2\sigma(x)$. Fitting a quadratic polynomial of the form

$$\sigma_{t\bar{t}} + x\sigma_{Wt} + x^2\sigma_{W^+W^-} \tag{5.5}$$

to $x^2\sigma(x)$ then provides a theoretically clean definition of the top-free W^+W^- cross section $\sigma_{W^+W^-}$.

To assess the validity of this definition, we can apply a b-jet veto and study the dependence of $\sigma_{W^+W^-}$ on the b-jet veto threshold $p_{T,\,\text{b-jet}}^{\text{veto}}$. In the following, we use the same electroweak parameters as in Section 5.2 and $\Gamma_t^{\text{phys}} = 1.443\,\text{GeV}$. All results are obtained using the MSTW2008 sets of parton distributions with four [177] or five [49] active flavours.

Fig. 5.22 (left) shows the full cross section in the 5FS as a function of $p_{T,\,\text{b-jet}}^{\text{veto}}$, compared to the cross section obtained in the 4FS, which does not contain any b-quarks in the external states and is thus $p_{T,\,\text{b-jet}}^{\text{veto}}$-independent[3]. In the inclusive case, $p_{T,\,\text{b-jet}}^{\text{veto}} \to \infty$, the contamination of the NLO and in particular of the NNLO W^+W^- cross section by single and double top production can be clearly seen. A $p_{T,\,\text{b-jet}}^{\text{veto}}$ in the range of 30 GeV suppresses around 90% of the contamination, as can be seen in the comparison with the

[3] Jets are defined using the anti-k_T algorithm [68] with $R = 0.4$, and in order to guarantee the cancellation of final-state collinear singularities, $b\bar{b}$ pairs that are recombined by the jet algorithm are not vetoed.

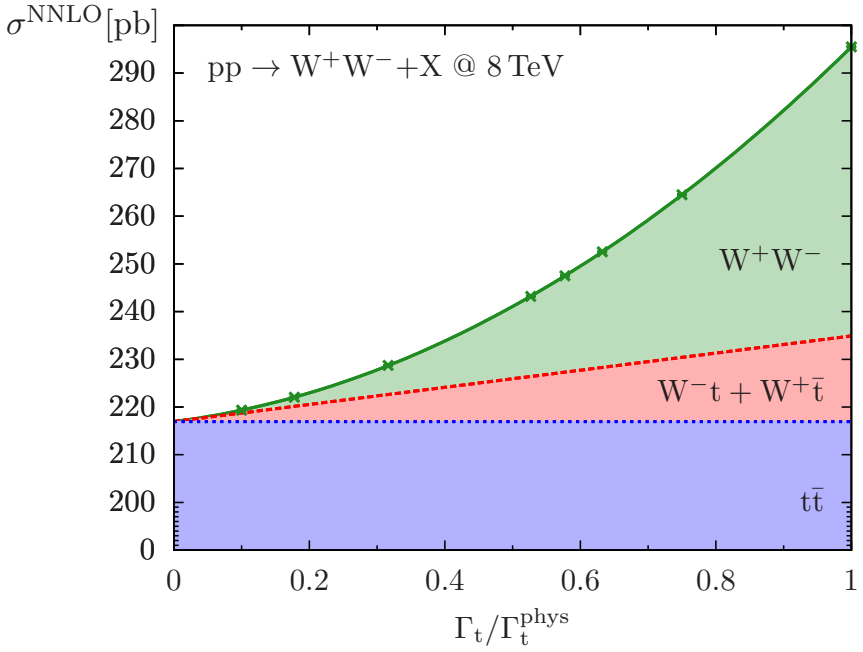

Figure 5.21: W^+W^- cross section at NNLO in the 5FS at $\sqrt{s} = 8\,\mathrm{TeV}$ as a function of $x \equiv \Gamma_t/\Gamma_t^{\mathrm{phys}}$, multiplied by x^2.

4FS cross section (lower panel), which is free of any top contamination. For veto thresholds of $p_{T,\,\mathrm{b-jet}}^{\mathrm{veto}} \sim 1\,\mathrm{GeV}$, the onset of the logarithmic singularity is visible, as the NLO cross section starts to diverge.

The top subtracted cross section $\sigma_{W^+W^-}$, as defined via Eq. (5.5) and the fitting procedure described above, on the other hand, is almost completely independent of $p_{T,\,\mathrm{b-jet}}^{\mathrm{veto}}$, as can be seen in Fig. 5.22 (right), and agrees with the 4FS cross section within uncertainties. In particular, in the inclusive limit $p_{T,\,\mathrm{b-jet}}^{\mathrm{veto}} \to \infty$, both cross sections agree within 1-2%.

In summary, we demonstrated that two independent ways to consistently define the inclusive top-free W^+W^- cross section, working in a 4FS or subtracting the contamination by exploiting its Γ_t scaling behaviour, result in predictions which are compatible within theoretical uncertainties. In the following, we will present all predictions as obtained in the 4FS.

Fig. 5.23 shows the total W^+W^- cross section as a function of the hadronic centre-of-mass energy. The experimentally measured cross section also contains a contribution from $H \to WW^*$, in which an off-shell W^+W^- pair is produced by an intermediate on-shell Higgs boson. As one of the W's has to be off-shell, this contribution is beyond our on-shell computation. In the upper panel of Fig. 5.23 it has been added by hand to all theory curves to make a direct comparison with data meaningful. We note however that the interpretation of the experimental values is in principle more subtle: while the Higgs boson contribution is present in the fiducial cross section, it is not taken into account in the extrapolation to the inclusive cross section, i.e. it is scaled according to the extrapolation of the pure on-shell W^+W^- contribution. This implies that the comparison with data in Fig. 5.23 should

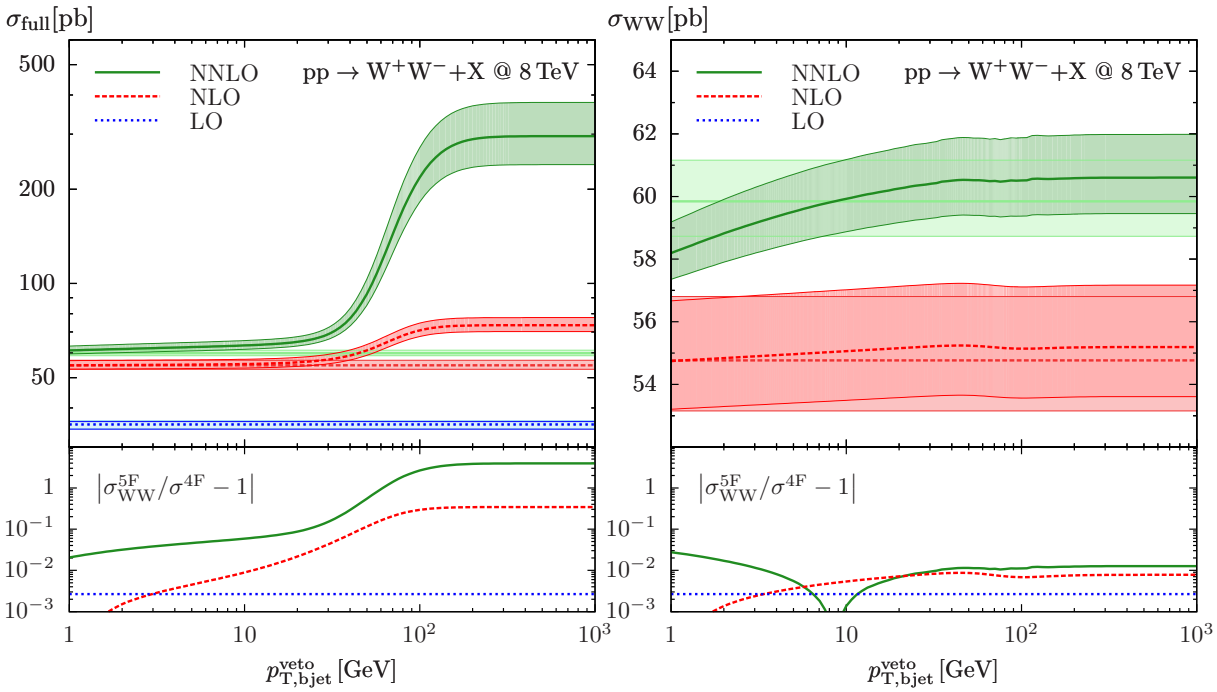

Figure 5.22: The $pp \to W^+W^-$ cross section in the 5FS at $\sqrt{s} = 8$ TeV is plotted versus a b-jet veto, $p_{T,\,\text{bjet}} < p^{\text{veto}}_{T,\,\text{b-jet}}$, and compared to results in the 4FS (which are $p^{\text{veto}}_{T,\,\text{b-jet}}$ independent). Full 5FS results (left plot) are contrasted with top-subtracted 5FS predictions (right plot). The relative agreement between 5FS and 4FS results is displayed in the lower frames.

only be considered to be a qualitative one. In the more recent analysis in Ref. [178], CMS properly subtracted the Higgs boson contribution, facilitating a comparison with the NNLO prediction.

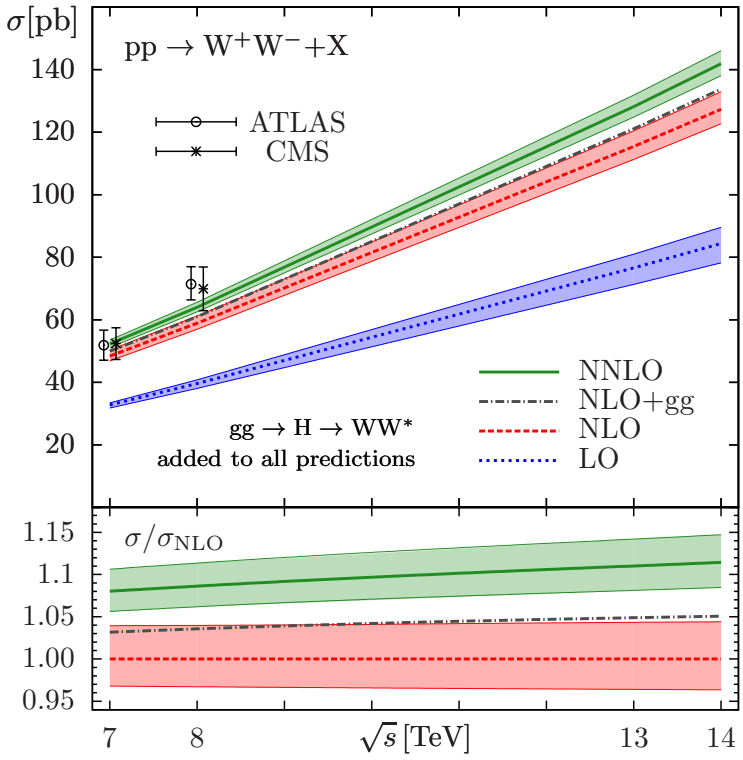

Figure 5.23: The on-shell W^+W^- cross section in the 4FS at LO (blue, dotted), NLO (red, dashed), NLO+gg (black, dash-dotted) and NNLO (green, solid) combined with $gg \to H \to WW^*$ is compared to recent ATLAS and CMS measurements [41–44]. In the lower panel NNLO and NLO+gg results are normalised to NLO predictions. The bands describe scale variations.

Table 5.14 reports separately the on-shell W^+W^- cross section at LO, NLO and NNLO, including scale uncertainties, and the off-shell $H \to WW^*$ contribution taken from Ref. [179]. The Higgs boson contribution amounts to 8% of the on-shell NNLO cross section. The NLO corrections increase the LO cross section from 53% at 7 TeV to 58% at 14 TeV and the NNLO corrections amount to an additional positive correction between 9% (at 7 TeV) and 12% (at 14 TeV). The scale uncertainty at NLO is on the level of ±4% and clearly underestimates the size of the NNLO corrections. At NNLO, the scale uncertainty reduces only slightly to ±3%, which is however dominated by the gluon-fusion contribution. Compared to ZZ production, the relative importance of the gluon-fusion contribution is reduced: it only amounts to about 35% of the α_S^2 correction.

The agreement with data is significantly improved once the NNLO corrections are included. A further increase in the theoretical prediction can be expected from the missing NLO corrections to the gluon-fusion contribution. On the other hand, off-shell effects will

$\frac{\sqrt{s}}{\text{TeV}}$	σ_{LO}	σ_{NLO}	σ_{NNLO}	$\sigma_{gg\to H\to WW^*}$
7	$29.52^{+1.6\%}_{-2.5\%}$	$45.16^{+3.7\%}_{-2.9\%}$	$49.04^{+2.1\%}_{-1.8\%}$	$3.25^{+7.1\%}_{-7.8\%}$
8	$35.50^{+2.4\%}_{-3.5\%}$	$54.77^{+3.7\%}_{-2.9\%}$	$59.84^{+2.2\%}_{-1.9\%}$	$4.14^{+7.2\%}_{-7.8\%}$
13	$67.16^{+5.5\%}_{-6.7\%}$	$106.0^{+4.1\%}_{-3.2\%}$	$118.7^{+2.5\%}_{-2.2\%}$	$9.44^{+7.4\%}_{-7.9\%}$
14	$73.74^{+5.9\%}_{-7.2\%}$	$116.7^{+4.1\%}_{-3.3\%}$	$131.3^{+2.6\%}_{-2.2\%}$	$10.64^{+7.5\%}_{-8.0\%}$

Table 5.14: LO, NLO and NNLO cross sections (in picobarn) for on-shell W^+W^- production in the 4FS and reference results for $gg \to H \to WW^*$ from Ref. [179].

likely have a negative impact of around -2% on the total cross section.

5.4 Transverse-momentum resummation effects in W^+W^- and ZZ production

In this section we present our results for the resummed transverse-momentum distributions of W^+W^- and ZZ pairs, obtained with the implementation of the q_{T} resummation formalism in Matrix as outlined in Section 4.3. We compare our NNLL+NNLO predictions to the results at the NLL+NLO, and discuss the corresponding theoretical uncertainties. Additionally, we also study the rapidity dependence of the p_T cross section as well as the p_T-veto efficiency.

For the EW couplings we use the G_μ scheme with input parameters $G_F = 1.16639 \times 10^{-5}$ GeV^{-2}, $m_W = 80.399$ GeV and $m_Z = 91.1876$ GeV. We use the NNPDF3.0 sets of parton distribution functions (PDFs) [53] with $\alpha_{\text{S}}(m_Z) = 0.118$. At NLL+NLO and NNLL+NNLO the running of α_{S} is evaluated at two- and three-loop order, respectively. For ZZ production we consider $N_f = 5$ massless quarks/antiquarks. For W^+W^- production we make use of the 4FS, which allows us to split off all contributions related to bottom-quark final states in order to remove the $t\bar{t}$ and Wt contamination from our computation, as explained in Section 5.3.

We consider proton-proton collisions at $\sqrt{s} = 8$ TeV. The central values of the factorisation and renormalisation scales are set to $\mu_F = \mu_R = \mu_0 = 2\,m_V$. The choice of the central resummation scale Q_0 is discussed in the next subsection.

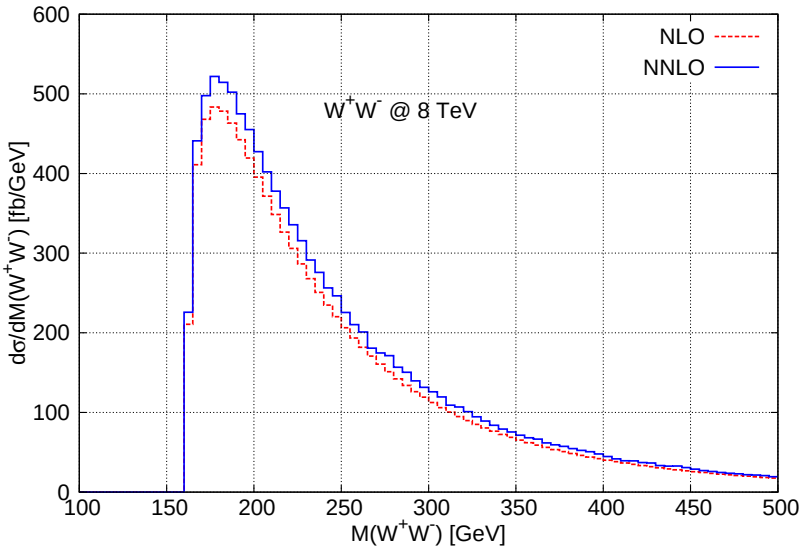

Figure 5.24: Invariant-mass (M_{WW}) distribution in W^+W^- pair production at NLO (red, dashed) and NNLO (blue, solid).

5.4.1 Choice of the central resummation scale

As discussed in Section 3.3, the resummation scale Q is the scale entering the large logarithmic terms we are resumming (see Eq. (3.16)). It plays the role of the scale up to which resummation is effective. In on-shell Higgs [87] and vector boson [180] production, the scale is typically chosen equal to half the mass of the heavy boson (i.e. $Q = m_H/2$ for Higgs and $Q = m_V/2$ in the case of single vector boson production). Higher values of the scale lead to a worse matching at high p_T. The natural extension of this choice for vector boson pair production is a dynamical resummation scale $Q = M_{VV}/2$, since M_{VV} is the hardness of the process, and this is indeed the choice that was adopted in the calculations of Refs. [166, 181].

The following considerations apply both to ZZ and W^+W^- production, and we will focus on W^+W^- production from now on. In Fig. 5.24 we consider the invariant-mass distribution of the W^+W^- pair at NLO and NNLO. We see that the distribution is strongly peaked in the threshold region, and that it quickly decreases as M_{WW} increases. As a consequence, for most of the W^+W^- events, $M_{WW} \gtrsim 2m_W$.

We can compare the transverse-momentum distributions obtained with a dynamical resummation scale $Q_0 = M_{WW}/2$, and a fixed resummation scale $Q_0 = m_W$. In Fig. 5.25 we show the ratio (solid blue curve) of the $Q = m_W$ result over the $Q = M_{WW}/2$ result. The bands are obtained by varying the resummation scale around the central value by a factor of two. Considering the ratio of the central curves for $p_T \lesssim 250\,\text{GeV}$, the differences between a fixed and a dynamical scale are extremely small and remain at the 1-2% level over the whole range. In this region of transverse momenta the uncertainty bands obtained with the

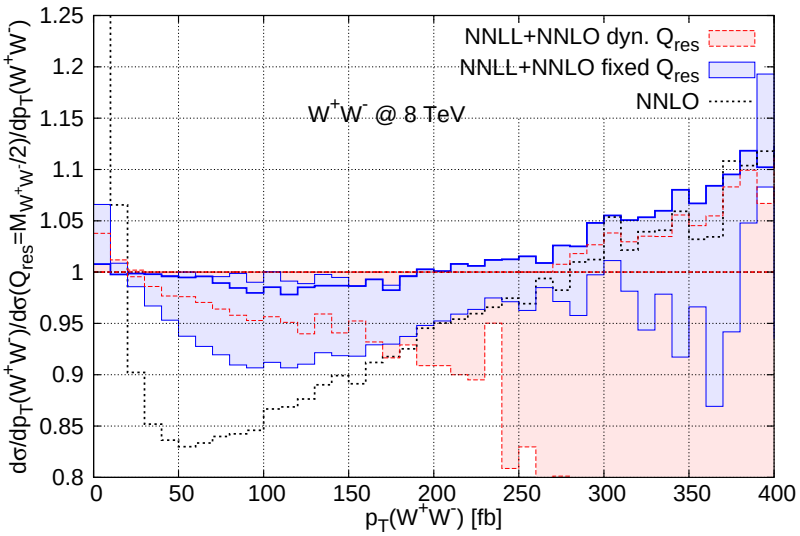

Figure 5.25: NNLL+NNLO transverse-momentum distribution of the W^+W^- pair with a fixed scale $Q = m_W$ normalised to the same cross section with a dynamical scale $Q = M_{WW}/2$. The bands are obtained by variation of the resummation scales in the numerator by a factor of two around the central scale. For reference, we show the fixed-order NNLO curve with the same normalisation.

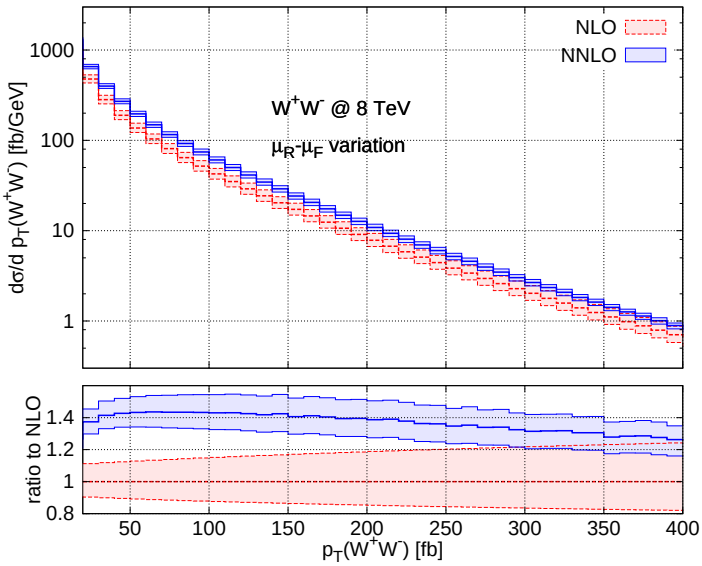

Figure 5.26: Transverse-momentum distribution of the W^+W^- pair at NLO (red, dashed) and NNLO (blue, solid); thick lines: central scale choices; bands: scale uncertainty from μ_F and μ_R obtained as described in the text. Lower inset: results normalised to the NLO prediction at central values of the scales.

two choices overlap and are similar in size. In fact, since $Q = m_W$ leads to slightly larger uncertainties, it appears to be the more conservative choice. Therefore, we can conclude that either choice of the resummation scale is perfectly valid and indeed consistent with each other as expected from the discussion of the invariant-mass distribution.

Looking further at the comparison of the high-p_T tails in Fig. 5.25 ($p_T \gtrsim 250\,\text{GeV}$), we observe a very well known feature [87,109,110,180,182] of the applied matching procedure, namely the fact that for large values of the resummation scale the fixed-order cross section (black dotted curve) is not recovered in the tail of the distribution. It is important to recall that transverse-momentum resummation is supposed to improve the perturbative expansion in the low-p_T region. At large p_T, any large dependence on the resummation scale is necessarily artificial and an unwanted remnant of the matching procedure. This behaviour is precisely what we observe for the dynamical scale choice $Q_0 = M_{WW}/2$ in Fig. 5.25. With this choice, in fact, the resummed result loses predictivity, as its uncertainty becomes increasingly large. By contrast, a fixed resummation scale $Q_0 = m_W$, which is always smaller than $Q_0 = M_{WW}/2$, eventually leads to a more consistent high-p_T behaviour of the resummed prediction.

Based on the above results, we make $Q_0 = m_V$ our default choice of the resummation scale in what follows.

5.4.2 Inclusive transverse-momentum distribution

We now present our resummed predictions for the inclusive transverse-momentum spectrum of the vector boson pair and compare them with the corresponding fixed-order results. We concentrate on W^+W^- production since we observe no saliently different features in the ZZ case. For completeness, we provide the corresponding reference prediction with uncertainties for ZZ below.

Before presenting our resummed predictions, we recall the well known fixed-order results at $\mathcal{O}(\alpha_S)$ and $\mathcal{O}(\alpha_S^2)$ [183–185]. In Fig. 5.26 we show the NLO and NNLO distributions together with their perturbative uncertainties. The uncertainty bands are obtained by varying μ_F and μ_R in the range $m_W \leq \{\mu_F, \mu_R\} \leq 4m_W$ with the constraint $0.5 \leq \mu_F/\mu_R \leq 2$. The lower inset shows the same results normalised to the central NLO curve. The NNLO effects range from about 40% at $p_T \sim 50$ GeV to about 30% at $p_T \sim 400$ GeV. The NLO (NNLO) uncertainty ranges from about $\pm 15\%$ ($\pm 10\%$) at $p_T \sim 50$ GeV to about $\pm 20\%$ ($\pm 8\%$) at $p_T \sim 400$ GeV. We note that the NLO and NNLO bands do not overlap in the region where $p_T \lesssim 300$ GeV. This implies that, in this region of transverse momenta, the size of the band obtained through scale variations at NLO definitely underestimates the theoretical uncertainty.

We now move on to the resummed results. In Fig. 5.27 (a) the NLL+NLO spectrum is compared to the fixed-order NLO result and to the finite component of the resummed cross section (see Eq. (3.18)) in the region between 0 and 80 GeV. As expected, the NLO cross section diverges to $+\infty$ as $p_T \to 0$, while the resummation provides a physically well behaved spectrum down to low values of p_T, which exhibits a kinematical peak at $p_T \sim 4$

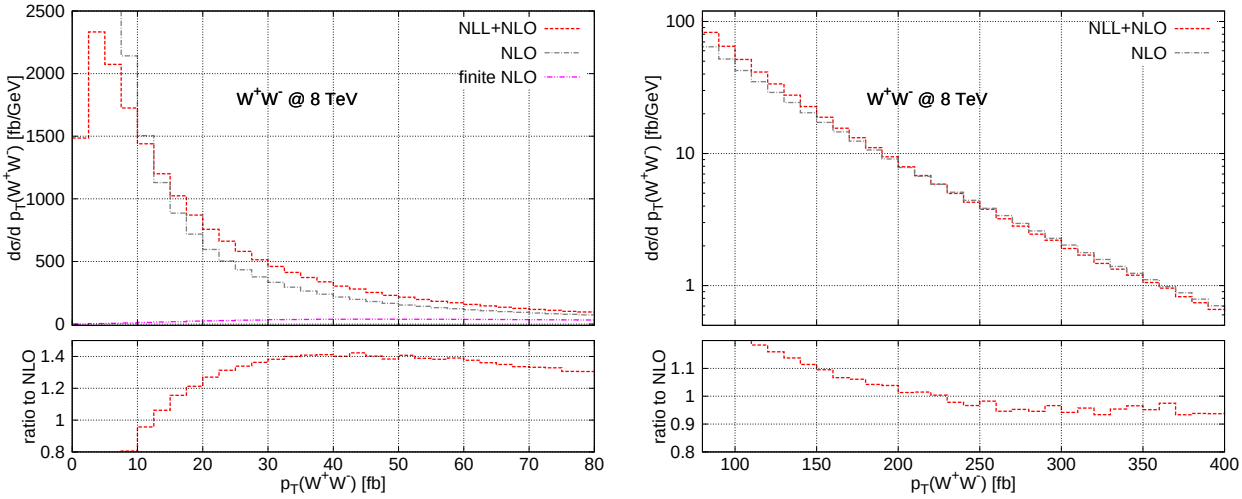

Figure 5.27: The transverse-momentum spectrum of the W^+W^- pair at NLL+NLO (a) in the low-p_T region and (b) at high transverse momenta. The NLL+NLO result (red, dashed) is compared to the fixed-order NLO prediction (grey, dash-dotted) and to the finite component of Eq. (3.18) (magenta, dash-double dotted). The lower insets show the NLL+NLO result normalised to NLO.

GeV. The finite component contributes less than 1% in the peak region, where the result is dominated by resummation, and it increases to $\sim 18\%$ at $p_T = 50$ GeV. The lower inset shows the NLL+NLO result normalised to NLO. In Fig. 5.27 (b) the region between 80 and 400 GeV is displayed. We see that even at large values of p_T the NLL+NLO resummed result does not match the fixed-order NLO result very well, with a difference of about 5%.

The analogous results at NNLL+NNLO are shown in Fig. 5.28. The NNLO has an unphysical (divergent) behaviour as $p_T \to 0$, whereas the resummed spectrum is well behaved, with a slightly harder peak with respect to the NLL+NLO. The finite component contributes less than 1% in the peak region, increasing to $\sim 19\%$ at $p_T = 50$ GeV. Comparing the right panels of Fig. 5.27 and Fig. 5.28, we see that the quality of the matching at high p_T is significantly improved when going from NLL+NLO to NNLL+NNLO, and we find that this behaviour is indeed preserved up to very high transverse momenta of the order of 1 TeV. The NNLL+NNLO result thus provides a prediction with uniform accuracy from the low- to the very high-p_T region and, in fact, provides a sufficiently large region where a hard switching to the fixed-order result is feasible. We point out that, thanks to our unitarity constraint in Eq. (3.64), both at NLL+NLO and at NNLL+NNLO the integral of the resummed spectrum is in excellent agreement with the respective total cross sections; the differences are at the few-permille level.

We now turn to the scale uncertainties of our resummed results. We start our discussion

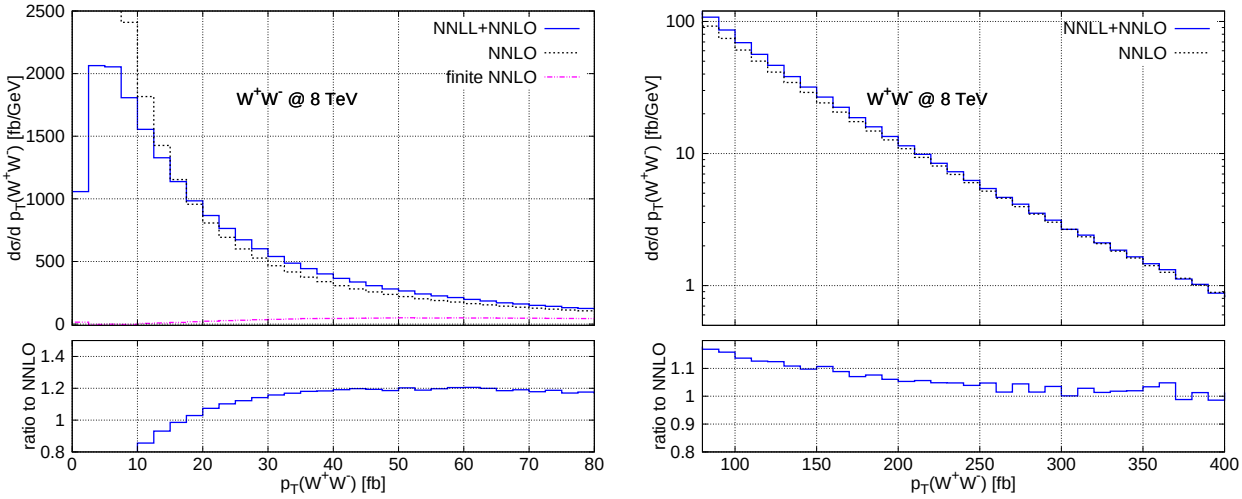

Figure 5.28: The transverse-momentum spectrum of the W^+W^- pair at NNLL+NNLO (a) in the low-p_T region and (b) at high transverse momenta. The NNLL+NNLO result (red, dashed) is compared to the fixed-order NNLO prediction (grey, dash-dotted) and to the finite component of Eq. (3.18) (magenta, dash-double dotted). The lower insets show the NNLL+NNLO result normalised to NNLO.

by separately considering factorisation and renormalisation scale variations. In Fig. 5.29 we compare the NLL+NLO (red, dashed) and NNLL+NNLO (blue, solid) predictions with their uncertainty bands from μ_F and μ_R variations (left and right panel, respectively). In both cases, the bands are obtained by varying the factorisation (renormalisation) scale by a factor of two around its central value, while keeping the other scales at their default values. First of all, we notice that when going from NLL+NLO to NNLL+NNLO the p_T spectrum becomes harder. Comparing with the results of Ref. [166], where the NNLL resummation was implemented without $\mathcal{O}(\alpha_S^2)$ matching, we see that the increased hardness of the p_T spectrum is a combined effect of both features, i.e., NNLL resummation and NNLO matching at high p_T.

We note that neither when varying the factorisation scale, nor when varying the renormalisation scale, the NLL+NLO and NNLL+NNLO bands overlap. Actually, in the case of the factorisation scale, there is no reduction in scale dependence when going from NLL+NLO to NNLL+NNLO, and the uncertainty slightly increases with the perturbative order, even if it is always well below 10%, except at very low p_T. The renormalisation scale dependence instead exhibits the expected reduction when going from NLL+NLO to NNLL+NNLO.

In Fig. 5.30 we present our resummed predictions with uncertainty bands obtained from simultaneous variations of μ_F and μ_R (left panel), and variation of the resummation scale

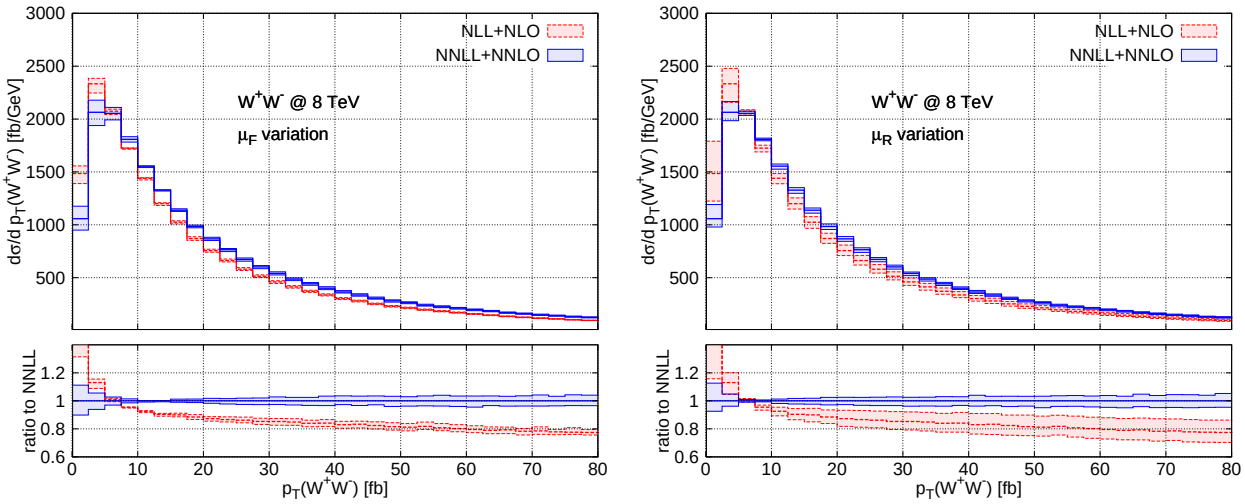

(a) (b)

Figure 5.29: W^+W^- transverse-momentum distribution at the NLL+NLO (red, dashed) and NNLL+NNLO (blue, solid); thick lines: central scale choices; bands: uncertainty due to (a) μ_F variation and (b) μ_R variation; thin lines: borders of bands.

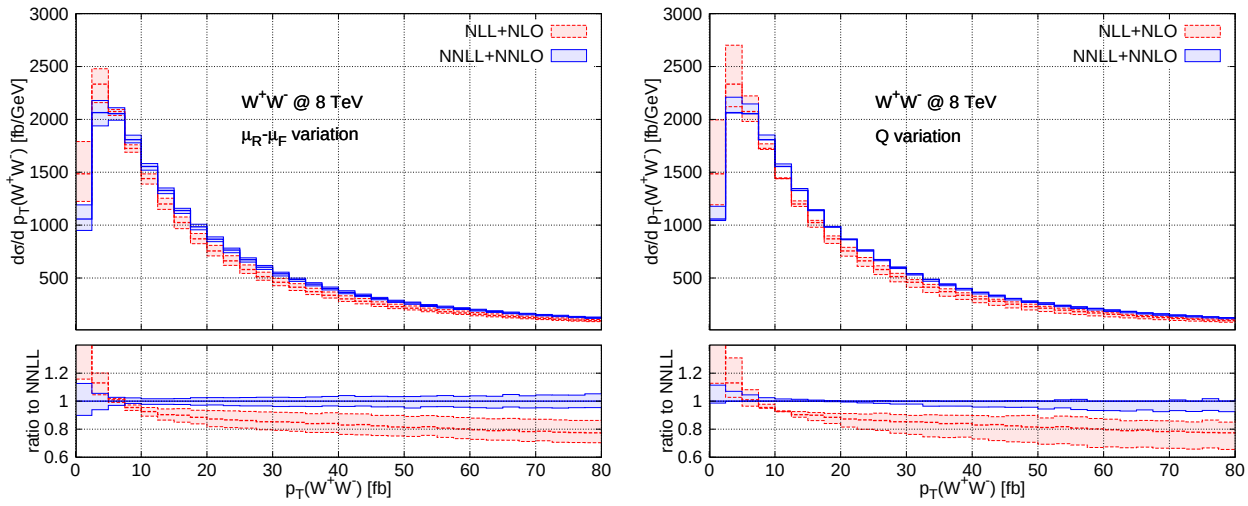

(a) (b)

Figure 5.30: W^+W^- transverse-momentum distribution at the NLL+NLO (red, dashed) and NNLL+NNLO (blue, solid); thick lines: central scale choices; bands: uncertainty due to (left) μ_F, μ_R variation and (right) Q variation; thin lines: borders of bands.

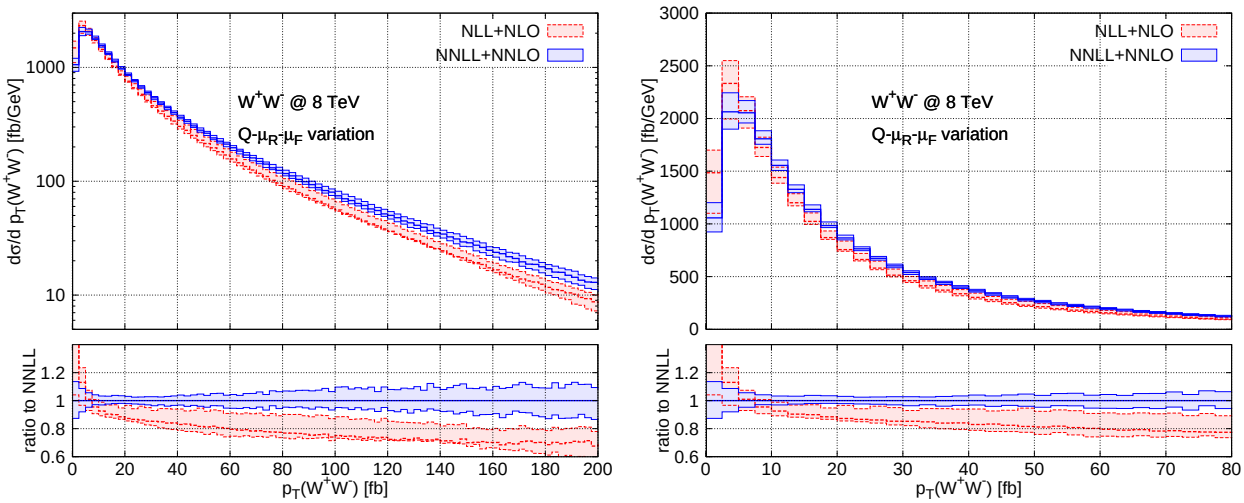

Figure 5.31: (a) Transverse-momentum distribution of the W^+W^- pair at NLL+NLO (red, dashed) and NNLL+NNLO (blue, solid); thick lines: central scale choices; bands: uncertainty from μ_F, μ_R and Q variations obtained as described in the text; thin lines: borders of bands. (b) detail of the low-p_T region.

Q (right panel). In the left panel the uncertainty bands are obtained by varying μ_F and μ_R as in Fig. 5.26. In the right panel the resummation scale is varied in the range $m_W/2 \leq Q \leq 2m_W$. As in Fig. 5.29, we see that the uncertainty bands do not overlap. The uncertainty from μ_F and μ_R variations is $\pm 10 - 15\%$ at NLL+NLO and is reduced to $8 - 10\%$ at NNLL+NNLO. At NLL+NLO the resummation scale uncertainty is generally about $\pm 15\%$ except in the region of $p_T \sim 10$ GeV, where it shrinks to smaller values. We find that at NNLL+NNLO the resummation scale uncertainty is reduced roughly by a factor of two in the region of transverse momenta considered in the figure.

In Fig. 5.31 and 5.32 we show our reference resummed prediction for W^+W^- and ZZ, respectively, with an estimate of their full perturbative uncertainty. In order to obtain a combined uncertainty from μ_F, μ_R and Q variations, we follow Ref. [180] and independently vary μ_F, μ_R and Q in the ranges $m_V \leq \{\mu_F, \mu_R\} \leq 4m_V$ and $m_V/2 \leq Q \leq 2m_V$ with the constraints $0.5 \leq \mu_F/\mu_R \leq 2$ and $0.5 \leq Q/\mu_R \leq 2$. We recall that the constraint on μ_F/μ_R, which is the same as applied in Fig. 5.26 and Fig. 5.30 (left), has the purpose of avoiding large logarithmic contributions from the evolution of parton densities. Analogously, the constraint on Q/μ_R avoids large logarithmic contributions in the expansion of the Sudakov form factor.

For W^+W^- production the perturbative uncertainty at NNLL+NNLO (NLL+NLO) is about $\pm 8\%$ ($\pm 12\%$) at the peak, it decreases to about $\pm 3\%$ ($\pm 5\%$) at $p_T = 20$ GeV, and it increases again to $\pm 10\%$ ($\pm 15\%$) at $p_T = 200$ GeV. In the high-p_T region, the difference

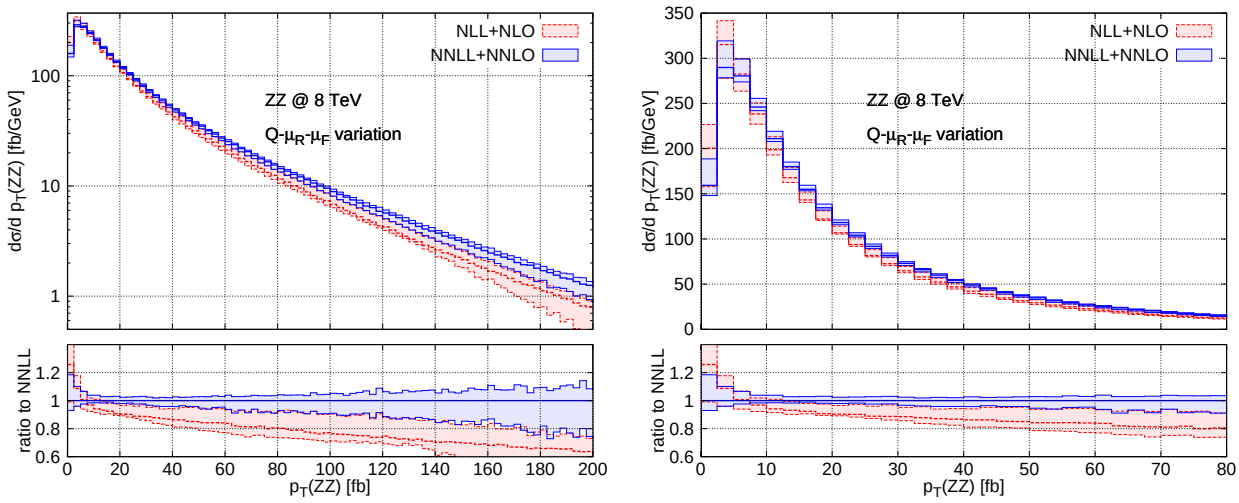

Figure 5.32: Same plot as Fig. 5.31, but for ZZ.

between the NNLL+NNLO and NLL+NLO predictions is driven by the NNLO effects, which increase the NLO result by about 30%.

For ZZ production the uncertainties have essentially the same pattern in the small- and intermediate-p_T region, while at high p_T they are larger than for W^+W^- production, reaching about $\pm 17\%$ at NNLL+NNLO for $p_T = 200$ GeV. We have checked that this effect is entirely driven by the resummation-scale dependence. As previously pointed out, this behaviour is not particularly worrying since, in the large-p_T region, the resummed results should be replaced by the corresponding fixed-order prediction. Also in the ZZ case the large enhancement of the NNLL+NNLO distribution in the high-p_T tail stems from the fixed-order cross section.

5.4.3 Rapidity dependence of the transverse-momentum distribution

So far, we only considered p_T spectra for on-shell W^+W^- and ZZ production that are inclusive in the kinematics of the vector boson pair. Our numerical program, however, allows us to compute arbitrary observables that are differential with respect to the VV' phase space.

In the following we study the behaviour of the transverse-momentum spectrum in different rapidity regions of the vector boson pair. In Fig. 5.33 we study the shape of the NNLL+NNLO transverse-momentum distribution, i. e. normalised such that its integral yields one, for $|y| < 0.5$ (red, solid), $0.5 < |y| < 1$ (blue, dashed), $1 < |y| < 2$ (black, dotted), $2 < |y| < 3$ (magenta, dash-dotted) and $3 < |y|$ (orange, dash-double dotted). The right panel shows the same results normalised to the fully inclusive distribution. We see

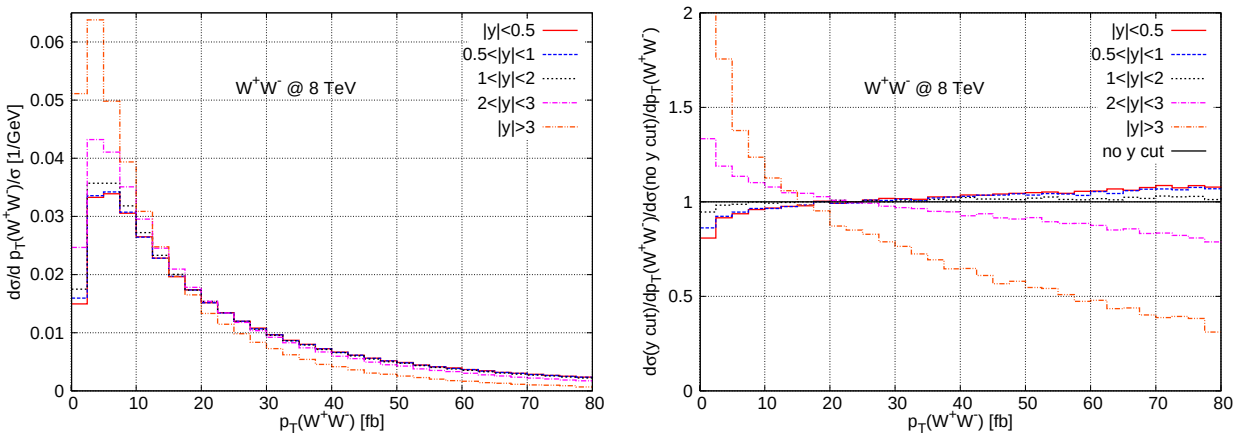

Figure 5.33: (a) Shapes of the W^+W^- transverse-momentum distribution differential in the rapidity of the W^+W^- pair at the NNLL+NNLO for $|y| < 0.5$ (red, solid), $0.5 < |y| < 1$ (blue, dashed), $1 < |y| < 2$ (black, dotted), $2 < |y| < 3$ (magenta, dash-dotted), $3 < |y|$ (orange, double-dash dotted); and (b) the shape-ratio with respect to the inclusive result.

that the p_T shapes become softer as the rapidity increases. In the central region ($|y| < 2$) the distributions are still quite insensitive to the specific value of the rapidity and only slightly harder than the inclusive spectrum. In the forward rapidity region, however, the shapes become increasingly softer.

The observed pattern can be understood in the following way: rapidity and transverse momentum are two not completely independent phase-space variables. Indeed, they affect their mutual upper integration boundaries. At higher rapidities the kinematically allowed region of transverse momenta is reduced: this squeezes the p_T spectrum which consequently becomes softer. This effect has been observed also in previous studies in the case of Higgs-boson production [186].

5.4.4 The W^+W^- cross section and p_T-veto efficiencies

The excess in the W^+W^- production cross section measured by ATLAS [44] with respect to the SM prediction has drawn a lot of attention to the W^+W^- process, since the W^+W^- signature appears in many new physics scenarios [174]. The inclusion of the recently computed NNLO corrections, see Section 5.3 and Ref. [28], considerably reduces the significance of the excess. However, particular attention must be payed to the modelling of the jet veto [168,175,187] when extrapolating from the fiducial region to obtain the inclusive cross section. Effects of jet veto resummation have been considered in Refs. [170,188],

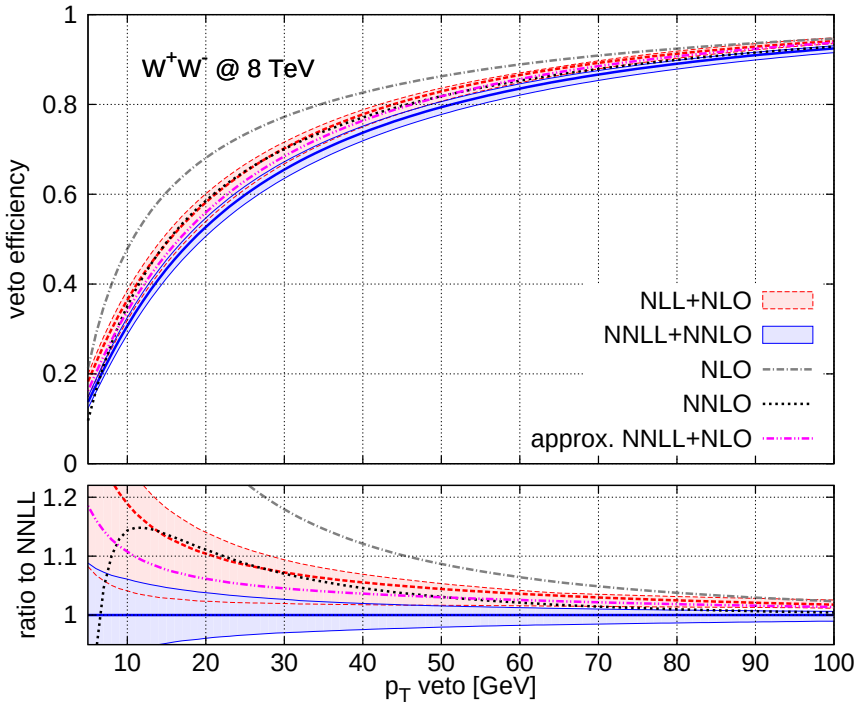

Figure 5.34: Veto efficiency for the transverse momentum of the W^+W^- pair at various orders: NLL+NLO (red, dashed), NNLL+NNLO (blue, solid), NLO (grey, dash-dotted), NNLO (black, dotted), approximate NNLL+NLO (magenta, dash-double dotted); thick lines: central scale choices; bands: uncertainty due to combined scale variations; thin lines: borders of bands.

though still matching to the fixed-order $\mathcal{O}(\alpha_S)$ result.

In this paper we are dealing with transverse-momentum spectra, and we perform a resummation on a different variable with respect to the jet p_T. However, the vector boson pair p_T and the jet p_T are clearly related variables (at $\mathcal{O}(\alpha_S)$ they coincide). We will therefore study the p_T-veto efficiency in W^+W^- production at different orders in resummed and fixed-order perturbation theory. We define the p_T-veto efficiency as

$$\epsilon(p_T^{\text{veto}}) = \sigma(p_T < p_T^{\text{veto}})/\sigma_{\text{tot}}\,. \tag{5.6}$$

In Fig. 5.34 we show $\epsilon(p_T^{\text{veto}})$ at the NNLL+NNLO (blue, solid), approximate NNLL+NLO (magenta, dash-double dotted), NLL+NLO (red, dashed), NNLO (black, dotted) and NLO (grey, dash-dotted). The lower inset shows the same curves normalised to our reference prediction at NNLL+NNLO. Our approximate NNLL+NLO result is obtained by simply

adding the $g^{(3)}$ function in the Sudakov exponent in Eq. (3.30) at NLL+NLO. This is the approximation considered in Refs. [166, 168].

For reference, the corresponding numerical values of the efficiencies are given in Table 5.15 for p_T = 5-40 GeV. The uncertainty bands are obtained by a combined variation of resummation, factorisation and renormalisation scales as in Fig. 5.31. The first thing we observe is that the NLO result appears to be well above the others and cannot be really considered a reliable prediction for the efficiency. This is due to it being essentially a LO prediction at finite values of p_T^{veto}. We also note that in the small-p_T region (say below $p_T \sim 10\,\text{GeV}$) the fixed-order NLO and NNLO predictions diverge and cannot be trusted. Comparing the fixed-order results among each other and the resummed results among each other, we observe that higher-order corrections in fixed-order and resummed perturbation theory reduce the p_T-veto efficiency.

Both effects can be easily understood in light of the results presented up to now. As seen in Fig. 5.26, the inclusion of the NNLO corrections makes the p_T distribution harder. Furthermore, resummation effects generally harden the spectrum. A qualitatively similar result is obtained when going from NLL+NLO to NNLL+NNLO, see Fig. 5.31.

It is interesting to compare the approximated NNLL+NLO result with the NNLO and NNLL+NNLO predictions. For values of $p_T^{\text{veto}} \sim 25-30$ GeV we see that the approximated result is in between the NNLO one and our best NNLL+NNLO prediction. This means that the effect of NNLL resummation obtained by the inclusion of the $g^{(3)}$ function in the Sudakov exponent in Eq. (3.30) is quantitatively important. Nonetheless, the efficiency obtained within this approximation is still about 5% higher than the NNLL+NNLO prediction. We also notice that in this region of p_T^{veto}, the NNLO and NLL+NLO results differ only by less than 1%.

Comparing the NNLL+NNLO and NLL+NLO results, we find that they are nicely compatible within the corresponding uncertainties.

We add a few comments on the recent measurement of the W^+W^- cross section carried out by the CMS collaboration [187]. The result shows good agreement with the NNLO prediction of Ref. [28]. The corresponding analysis, however, is based on a reweighting procedure of the p_T spectrum of the W^+W^-pair. The events generated with POWHEG [189] plus Pythia6 [190] were reweighted using the calculation of Ref. [168], which corresponds to our NNLL+NLO approximation, and does include neither the second order hard-collinear coefficient $\mathcal{H}^{WW,(2)}$ in Eq. (3.29), nor the NNLO matching. The results in Fig. 5.34 show that the NNLL+NNLO p_T-veto efficiency is lower than the efficiency obtained with the approximated NNLL+NLO calculation. As a consequence, a reweighting to the full NNLL+NNLO prediction for the W^+W^- spectrum would most likely lead to a decrease of the jet-veto efficiency.

$p_T^{\rm veto}$ [GeV]	$\sigma(p_T < p_T^{\rm veto})/\sigma_{\rm tot}$ [%] NNLO+NNLL	approx. NNLL+NLO	NLO+NLL	NNLO	NLO
5	$13.7^{+8.8\%}_{-9.6\%}$	16.2	$18.3^{+8.8\%}_{-19\%}$	9.6	21.2
10	$30.7^{+6.1\%}_{-6.2\%}$	34.0	$36.5^{+5.9\%}_{-12\%}$	35.1	47.8
15	$43.4^{+4.7\%}_{-4.8\%}$	46.7	$49.1^{+4.3\%}_{-9.2\%}$	49.3	60.4
20	$52.7^{+3.8\%}_{-3.9\%}$	55.9	$58.2^{+3.3\%}_{-7.3\%}$	58.5	68.1
25	$59.9^{+3.1\%}_{-3.4\%}$	63.0	$65.0^{+2.6\%}_{-5.9\%}$	65.1	73.4
30	$65.5^{+2.7\%}_{-3.0\%}$	68.4	$70.2^{+2.0\%}_{-4.9\%}$	70.1	77.2
35	$70.0^{+2.3\%}_{-2.7\%}$	72.8	$74.4^{+1.6\%}_{-4.2\%}$	74.0	80.2
40	$73.7^{+2.0\%}_{-2.5\%}$	76.4	$77.8^{+1.3\%}_{-3.6\%}$	77.1	82.6

Table 5.15: Predictions for the p_T-veto efficiency (in percent) at various perturbative orders.

6 Conclusions and outlook

In this thesis we presented the computation of NNLO QCD corrections to the production processes of vector boson pairs at the LHC. In particular, we discussed the computation of NNLO corrections to $Z\gamma$, $W\gamma$, ZZ and W^+W^- production. We also presented first results for the $pp(\to ZZ) \to 4\,\text{leptons}$ process at NNLO. All computations were performed with the numerical program Matrix, which combines the general purpose NLO generator Munich [39] with q_T subtraction [38] and the one-loop amplitude provider OpenLoops [11]. Due to its general structure, Matrix is able to perform NNLO computations for various important processes at hadron colliders once the relevant two-loop amplitudes are available.

The phenomenological applications discussed in Chapter 5 of this thesis are of immediate interest for the ongoing experimental studies at the LHC. During the course of this thesis, we provided tailor-made predictions, both for inclusive cross sections and for differential observables, to several groups at ATLAS, CMS and to a local LHCb group. Examples include background predictions for the ATLAS Higgs boson width measurement in the ZZ and W^+W^- decay channels [191], signal predictions for the CMS measurement of $Z\gamma$ cross sections [127], and estimates of background uncertainties in the ATLAS $H \to W^+W^-$ measurement [128] and an ATLAS BSM Higgs boson search [192].

The large NNLO correction of the order of 20% we found for the $W\gamma$ production cross section, see Section 5.1, explains an excess measured by the ATLAS collaboration [40]. Our study also clarified the underlying cause for the large size of the NNLO corrections in this case by tracing it back to the radiation zero present at LO, see the discussion in Section 5.1.6.

Our computation of NNLO corrections to the production of an on-shell W^+W^- pair is particularly interesting in light of the excess in the total W^+W^- cross section reported by ATLAS [44] and to a lesser degree by CMS [43]. We found a correction of more than 9% with respect to the NLO result, significantly reducing the tension with the experimental measurements. While other theoretical issues, such as the jet-veto modelling, have not been settled completely, the new CMS analysis published in Ref. [178] now finds very good agreement with our NNLO prediction.

Exploiting the fact that q_T subtraction is derived from transverse-momentum resummation, we extended Matrix to also perform NNLL+NNLO resummation of the large logarithms in the low transverse-momentum region. The first application to the case of on-shell ZZ and W^+W^- pairs was discussed in Section 5.4. It is of direct relevance in the case of ZZ production, where the total transverse momentum of the final-state system

can be fully reconstructed. In the case of W^+W^- production, the resummed spectrum can be employed for a reweighting of the Monte Carlo spectrum used in the extrapolation of the measured fiducial cross section to a total W^+W^- cross section. This was for example done in the CMS analysis of Ref. [178], where the approximated NNLL+NLO prediction of Ref. [168] was used. In the future, this prediction will likely be superseded by our NNLL+NNLO computation.

The two processes still missing to complete the list of NNLO corrections to diboson production processes are off-shell W^+W^- production and WZ production, both with their respective leptonic decays. As all ingredients are available to assemble the relevant two-loop amplitudes, finishing these computations will only require a limited amount of work.

Another step to improve the theoretical accuracy in the case of ZZ and W^+W^- production would be the inclusion of NLO corrections to the gluon-fusion subcontribution. Formally, these NLO corrections are of order $\mathcal{O}(\alpha_S^3)$, i.e. part of the N^{3}LO corrections to the quark-antiquark initiated process. However, similar to the case of Higgs production in gluon fusion, the relative size of the higher-order corrections might be large, and therefore they could amount to several percent of the LO $q\bar{q} \to ZZ/W^+W^-$ cross section. The computation of NLO corrections to $gg \to ZZ/W^+W^-$ requires the relevant two-loop amplitudes. These are now available for the contribution where only massless quarks run in the loops [193, 194], which is expected to provide the dominant part of the corrections [195].

In addition, the resummation of large logarithms in the small transverse-momentum region can be extended to all diboson processes. Particularly interesting would be the computation of NNLL+NNLO corrections to the transverse-momentum spectrum of leptonically decaying ZZ pairs with realistic experimental selection cuts, which could for example be directly compared to the measured transverse-momentum spectrum published by CMS in Ref. [157].

Besides the many immediate applications of the phenomenological studies presented in this thesis, the main outcome is two-fold: on a conceptual level, Matrix serves as a proof-of-concept for the combination of sophisticated NLO technology, both on the amplitude and on the phase-space integration side, with a suitable NNLO subtraction scheme, in this case q_T subtraction. We found that this strategy is able to significantly reduce the manual work required to obtain a numerical NNLO code for a given process. Other subtraction schemes are also likely to benefit from such an approach to a varying degree. A particularly natural candidate – due to its conceptual similarity with q_T subtraction – would be N-jettiness subtraction [18].

In addition, the numerical program Matrix will continue to be developed and will become publicly available at some point in the future. To our knowledge, Matrix is the first integrated code able to perform fully differential NNLO computations for a wide class of important processes. Its release, together with progress in other areas such as the computation of multi-loop matrix elements and efforts to merge NNLO computations with parton showers, will mark an important step forward in pushing the standard accuracy of the field to a new level.

Bibliography

[1] K. A. Olive et al., Particle Data Group collaboration, *Review of Particle Physics*, Chin. Phys. **C38** (2014), 090001.

[2] G. Aad et al., ATLAS collaboration, *Observation of a new particle in the search for the Standard Model Higgs boson with the ATLAS detector at the LHC*, Phys.Lett. **B716** (2012), 1–29, [arXiv:1207.7214 [hep-ex]].

[3] S. Chatrchyan et al., CMS collaboration, *Observation of a new boson at a mass of 125 GeV with the CMS experiment at the LHC*, Phys.Lett. **B716** (2012), 30–61, [arXiv:1207.7235 [hep-ex]].

[4] E. Gildener, *Gauge Symmetry Hierarchies*, Phys. Rev. **D14** (1976), 1667.

[5] S. Weinberg, *Gauge Hierarchies*, Phys. Lett. **B82** (1979), 387.

[6] P. A. R. Ade et al., Planck collaboration, *Planck 2015 results. XIII. Cosmological parameters*, arXiv:1502.01589 [astro-ph.CO].

[7] M. Drees and G. Gerbier, *Mini-Review of Dark Matter: 2012*, arXiv:1204.2373 [hep-ph].

[8] S. Frixione, Z. Kunszt and A. Signer, *Three jet cross-sections to next-to-leading order*, Nucl.Phys. **B467** (1996), 399–442, [arXiv:hep-ph/9512328 [hep-ph]].

[9] S. Catani and M. Seymour, *The Dipole formalism for the calculation of QCD jet cross-sections at next-to-leading order*, Phys.Lett. **B378** (1996), 287–301, [arXiv:hep-ph/9602277 [hep-ph]].

[10] S. Catani and M. Seymour, *A General algorithm for calculating jet cross-sections in NLO QCD*, Nucl.Phys. **B485** (1997), 291–419, [arXiv:hep-ph/9605323 [hep-ph]].

[11] F. Cascioli, P. Maierhofer and S. Pozzorini, *Scattering Amplitudes with Open Loops*, Phys.Rev.Lett. **108** (2012), 111601, [arXiv:1111.5206 [hep-ph]].

[12] J. Alwall, R. Frederix, S. Frixione, V. Hirschi, F. Maltoni et al., *The automated computation of tree-level and next-to-leading order differential cross sections, and their matching to parton shower simulations*, JHEP **1407** (2014), 079, [arXiv:1405.0301 [hep-ph]].

[13] G. Cullen et al., *GOSAM-2.0: a tool for automated one-loop calculations within the Standard Model and beyond*, Eur. Phys. J. **C74** (2014), no. 8, 3001, [arXiv:1404.7096 [hep-ph]].

[14] T. Gleisberg, S. Hoeche, F. Krauss, M. Schonherr, S. Schumann et al., *Event generation with SHERPA 1.1*, JHEP **0902** (2009), 007, [arXiv:0811.4622 [hep-ph]].

[15] A. Gehrmann-De Ridder, T. Gehrmann and E. N. Glover, *Antenna subtraction at NNLO*, JHEP **0509** (2005), 056, [arXiv:hep-ph/0505111 [hep-ph]].

[16] M. Czakon, *A novel subtraction scheme for double-real radiation at NNLO*, Phys.Lett. **B693** (2010), 259–268, [arXiv:1005.0274 [hep-ph]].

[17] M. Czakon and D. Heymes, *Four-dimensional formulation of the sector-improved residue subtraction scheme*, Nucl.Phys. **B890** (2014), 152–227, [arXiv:1408.2500 [hep-ph]].

[18] J. Gaunt, M. Stahlhofen, F. J. Tackmann and J. R. Walsh, *N-jettiness Subtractions for NNLO QCD Calculations*, arXiv:1505.04794 [hep-ph].

[19] T. Gehrmann and L. Tancredi, *Two-loop QCD helicity amplitudes for $q\bar{q} \to W^{\pm}\gamma$ and $q\bar{q} \to Z^0\gamma$*, JHEP **1202** (2012), 004, [arXiv:1112.1531 [hep-ph]].

[20] T. Gehrmann, A. von Manteuffel, L. Tancredi and E. Weihs, *The two-loop master integrals for $q\overline{q} \to VV$*, JHEP **1406** (2014), 032, [arXiv:1404.4853 [hep-ph]].

[21] F. Caola, J. M. Henn, K. Melnikov, A. V. Smirnov and V. A. Smirnov, *Two-loop helicity amplitudes for the production of two off-shell electroweak bosons in quark-antiquark collisions*, JHEP **1411** (2014), 041, [arXiv:1408.6409 [hep-ph]].

[22] T. Gehrmann, A. von Manteuffel and L. Tancredi, *The two-loop helicity amplitudes for $q\bar{q}' \to V_1V_2 \to 4$ leptons*, arXiv:1503.04812 [hep-ph].

[23] R. Boughezal, F. Caola, K. Melnikov, F. Petriello and M. Schulze, *Higgs boson production in association with a jet at next-to-next-to-leading order in perturbative QCD*, JHEP **1306** (2013), 072, [arXiv:1302.6216 [hep-ph]].

[24] M. Czakon, P. Fiedler and A. Mitov, *Total Top-Quark Pair-Production Cross Section at Hadron Colliders Through $O(\alpha_S^4)$*, Phys.Rev.Lett. **110** (2013), 252004, [arXiv:1303.6254 [hep-ph]].

[25] M. Grazzini, S. Kallweit, D. Rathlev and A. Torre, *$Z\gamma$ production at hadron colliders in NNLO QCD*, Phys.Lett. **B731** (2014), 204–207, [arXiv:1309.7000 [hep-ph]].

[26] J. Currie, A. Gehrmann-De Ridder, E. Glover and J. Pires, *NNLO QCD corrections to jet production at hadron colliders from gluon scattering*, JHEP **1401** (2014), 110, [arXiv:1310.3993 [hep-ph]].

[27] F. Cascioli, T. Gehrmann, M. Grazzini, S. Kallweit, P. Maierhöfer, A. von Manteuffel, S. Pozzorini, D. Rathlev, L. Tancredi and E. Weihs, *ZZ production at hadron colliders in NNLO QCD*, Phys. Lett. **B735** (2014), 311–313, [arXiv:1405.2219 [hep-ph]].

[28] T. Gehrmann, M. Grazzini, S. Kallweit, P. Maierhöfer, A. von Manteuffel et al., W^+W^- *Production at Hadron Colliders in Next to Next to Leading Order QCD*, Phys.Rev.Lett. **113** (2014), no. 21, 212001, [arXiv:1408.5243 [hep-ph]].

[29] X. Chen, T. Gehrmann, E. Glover and M. Jaquier, *Precise QCD predictions for the production of Higgs + jet final states*, Phys.Lett. **B740** (2015), 147–150, [arXiv:1408.5325 [hep-ph]].

[30] G. Abelof and A. Gehrmann-De Ridder, *Light fermionic NNLO QCD corrections to top-antitop production in the quark-antiquark channel*, JHEP **1412** (2014), 076, [arXiv:1409.3148 [hep-ph]].

[31] M. Czakon, P. Fiedler and A. Mitov, *Resolving the Tevatron Top Quark Forward-Backward Asymmetry Puzzle: Fully Differential Next-to-Next-to-Leading-Order Calculation*, Phys. Rev. Lett. **115** (2015), no. 5, 052001, [arXiv:1411.3007 [hep-ph]].

[32] M. Grazzini, S. Kallweit and D. Rathlev, $W\gamma$ *and* $Z\gamma$ *production at the LHC in NNLO QCD*, JHEP **07** (2015), 085, [arXiv:1504.01330 [hep-ph]].

[33] R. Boughezal, C. Focke, X. Liu and F. Petriello, *W-boson production in association with a jet at next-to-next-to-leading order in perturbative QCD*, arXiv:1504.02131 [hep-ph].

[34] R. Boughezal, F. Caola, K. Melnikov, F. Petriello and M. Schulze, *Higgs Boson Production in Association with a Jet at Next-to-Next-to-Leading Order*, arXiv:1504.07922 [hep-ph].

[35] G. Abelof, A. Gehrmann-De Ridder and I. Majer, *Top quark pair production at NNLO in the quark-antiquark channel*, arXiv:1506.04037 [hep-ph].

[36] A. G.-D. Ridder, T. Gehrmann, E. W. N. Glover, A. Huss and T. A. Morgan, *Precise QCD predictions for the production of a Z boson in association with a hadronic jet*, arXiv:1507.02850 [hep-ph].

[37] M. Grazzini, S. Kallweit and D. Rathlev, *ZZ production at the LHC: fiducial cross sections and distributions in NNLO QCD*, arXiv:1507.06257 [hep-ph].

[38] S. Catani and M. Grazzini, *An NNLO subtraction formalism in hadron collisions and its application to Higgs boson production at the LHC*, Phys.Rev.Lett. **98** (2007), 222002, [arXiv:hep-ph/0703012 [hep-ph]].

[39] S. Kallweit, *in preparation*, MUNICH is the abbreviation of "MUlti-chaNnel Integrator at Swiss (CH) precision"—an automated parton level NLO generator.

[40] G. Aad et al., ATLAS collaboration, *Measurements of $W\gamma$ and $Z\gamma$ production in pp collisions at $\sqrt{s}$=7 TeV with the ATLAS detector at the LHC*, Phys.Rev. **D87** (2013), no. 11, 112003, [arXiv:1302.1283 [hep-ex]].

[41] G. Aad et al., ATLAS collaboration, *Measurement of W^+W^- production in pp collisions at $\sqrt{s}$=7 TeV with the ATLAS detector and limits on anomalous WWZ and $WW\gamma$ couplings*, Phys.Rev. **D87** (2013), no. 11, 112001, [arXiv:1210.2979 [hep-ex]].

[42] S. Chatrchyan et al., CMS collaboration, *Measurement of the W^+W^- Cross section in pp Collisions at $\sqrt{s} = 7$ TeV and Limits on Anomalous $WW\gamma$ and WWZ couplings*, Eur.Phys.J. **C73** (2013), no. 10, 2610, [arXiv:1306.1126 [hep-ex]].

[43] S. Chatrchyan et al., CMS collaboration, *Measurement of W^+W^- and ZZ production cross sections in pp collisions at sqrt(s) = 8 TeV*, Phys.Lett. **B721** (2013), 190–211, [arXiv:1301.4698 [hep-ex]].

[44] T. A. collaboration, ATLAS collaboration, *Measurement of the W^+W^- production cross section in proton-proton collisions at $\sqrt{s} = 8$ TeV with the ATLAS detector*.

[45] T. van Ritbergen, J. Vermaseren and S. Larin, *The Four loop beta function in quantum chromodynamics*, Phys.Lett. **B400** (1997), 379–384, [arXiv:hep-ph/9701390 [hep-ph]].

[46] M. Czakon, *The Four-loop QCD beta-function and anomalous dimensions*, Nucl.Phys. **B710** (2005), 485–498, [arXiv:hep-ph/0411261 [hep-ph]].

[47] R. K. Ellis, W. J. Stirling and B. Webber, *QCD and collider physics*, Camb.Monogr.Part.Phys.Nucl.Phys.Cosmol. **8** (1996), 1–435.

[48] A. Buckley, J. Butterworth, S. Gieseke, D. Grellscheid, S. Hoche et al., *General-purpose event generators for LHC physics*, Phys.Rept. **504** (2011), 145–233, [arXiv:1101.2599 [hep-ph]].

[49] A. Martin, W. Stirling, R. Thorne and G. Watt, *Parton distributions for the LHC*, Eur.Phys.J. **C63** (2009), 189–285, [arXiv:0901.0002 [hep-ph]].

[50] H.-L. Lai, M. Guzzi, J. Huston, Z. Li, P. M. Nadolsky et al., *New parton distributions for collider physics*, Phys.Rev. **D82** (2010), 074024, [arXiv:1007.2241 [hep-ph]].

[51] A. Cooper-Sarkar, ZEUS, H1 collaboration, *PDF Fits at HERA*, PoS **EPS-HEP2011** (2011), 320, [arXiv:1112.2107 [hep-ph]].

[52] S. Alekhin, J. Bluemlein and S. Moch, *The ABM parton distributions tuned to LHC data*, Phys.Rev. **D89** (2014), no. 5, 054028, [arXiv:1310.3059 [hep-ph]].

[53] R. D. Ball et al., NNPDF collaboration, *Parton distributions for the LHC Run II*, JHEP **1504** (2015), 040, [arXiv:1410.8849 [hep-ph]].

[54] L. Harland-Lang, A. Martin, P. Motylinski and R. Thorne, *Parton distributions in the LHC era: MMHT 2014 PDFs*, arXiv:1412.3989 [hep-ph].

[55] V. Gribov and L. Lipatov, *Deep inelastic e p scattering in perturbation theory*, Sov.J.Nucl.Phys. **15** (1972), 438–450.

[56] G. Altarelli and G. Parisi, *Asymptotic Freedom in Parton Language*, Nucl.Phys. **B126** (1977), 298.

[57] Y. L. Dokshitzer, *Calculation of the Structure Functions for Deep Inelastic Scattering and e^+e^- Annihilation by Perturbation Theory in Quantum Chromodynamics.*, Sov.Phys.JETP **46** (1977), 641–653.

[58] F. Bloch and A. Nordsieck, *Note on the Radiation Field of the electron*, Phys.Rev. **52** (1937), 54–59.

[59] T. Kinoshita, *Mass singularities of Feynman amplitudes*, J.Math.Phys. **3** (1962), 650–677.

[60] T. Lee and M. Nauenberg, *Degenerate Systems and Mass Singularities*, Phys.Rev. **133** (1964), B1549–B1562.

[61] J. M. Campbell and E. W. N. Glover, *Double unresolved approximations to multiparton scattering amplitudes*, Nucl. Phys. **B527** (1998), 264–288, [arXiv:hep-ph/9710255 [hep-ph]].

[62] Z. Bern, V. Del Duca, W. B. Kilgore and C. R. Schmidt, *The infrared behavior of one loop QCD amplitudes at next-to-next-to leading order*, Phys. Rev. **D60** (1999), 116001, [arXiv:hep-ph/9903516 [hep-ph]].

[63] S. Catani and M. Grazzini, *The soft gluon current at one loop order*, Nucl.Phys. **B591** (2000), 435–454, [arXiv:hep-ph/0007142 [hep-ph]].

[64] S. Catani and M. Grazzini, *Infrared factorization of tree level QCD amplitudes at the next-to-next-to-leading order and beyond*, Nucl.Phys. **B570** (2000), 287–325, [arXiv:hep-ph/9908523 [hep-ph]].

[65] S. Catani, Y. L. Dokshitzer, M. Seymour and B. Webber, *Longitudinally invariant K_t clustering algorithms for hadron hadron collisions*, Nucl.Phys. **B406** (1993), 187–224.

[66] S. D. Ellis and D. E. Soper, *Successive combination jet algorithm for hadron collisions*, Phys.Rev. **D48** (1993), 3160–3166, [arXiv:hep-ph/9305266 [hep-ph]].

[67] Y. L. Dokshitzer, G. Leder, S. Moretti and B. Webber, *Better jet clustering algorithms*, JHEP **9708** (1997), 001, [arXiv:hep-ph/9707323 [hep-ph]].

[68] M. Cacciari, G. P. Salam and G. Soyez, *The Anti-k(t) jet clustering algorithm*, JHEP **0804** (2008), 063, [arXiv:0802.1189 [hep-ph]].

[69] M. Wobisch and T. Wengler, *Hadronization corrections to jet cross-sections in deep inelastic scattering*, arXiv:hep-ph/9907280 [hep-ph].

[70] G. F. Sterman and S. Weinberg, *Jets from Quantum Chromodynamics*, Phys.Rev.Lett. **39** (1977), 1436.

[71] W. Giele and E. N. Glover, *Higher order corrections to jet cross-sections in e^+e^- annihilation*, Phys.Rev. **D46** (1992), 1980–2010.

[72] W. Giele, E. N. Glover and D. A. Kosower, *Higher order corrections to jet cross-sections in hadron colliders*, Nucl.Phys. **B403** (1993), 633–670, [arXiv:hep-ph/9302225 [hep-ph]].

[73] R. K. Ellis, D. A. Ross and A. E. Terrano, *The Perturbative Calculation of Jet Structure in e^+e^- Annihilation*, Nucl. Phys. **B178** (1981), 421.

[74] S. Frixione, *A General approach to jet cross-sections in QCD*, Nucl.Phys. **B507** (1997), 295–314, [arXiv:hep-ph/9706545 [hep-ph]].

[75] T. Gleisberg and S. Hoeche, *Comix, a new matrix element generator*, JHEP **0812** (2008), 039, [arXiv:0808.3674 [hep-ph]].

[76] Z. Bern, G. Diana, L. Dixon, F. Febres Cordero, S. Hoeche et al., *Four-Jet Production at the Large Hadron Collider at Next-to-Leading Order in QCD*, Phys.Rev.Lett. **109** (2012), 042001, [arXiv:1112.3940 [hep-ph]].

[77] A. Denner, S. Dittmaier, S. Kallweit and S. Pozzorini, *NLO QCD corrections to WWbb production at hadron colliders*, Phys.Rev.Lett. **106** (2011), 052001, [arXiv:1012.3975 [hep-ph]].

[78] F. Cascioli, S. Kallweit, P. Maierhöfer and S. Pozzorini, *A unified NLO description of top-pair and associated Wt production*, Eur.Phys.J. **C74** (2014), no. 3, 2783, [arXiv:1312.0546 [hep-ph]].

[79] R. Frederix, S. Frixione, F. Maltoni and T. Stelzer, *Automation of next-to-leading order computations in QCD: The FKS subtraction*, JHEP **0910** (2009), 003, [arXiv:0908.4272 [hep-ph]].

[80] G. Somogyi, Z. Trocsanyi and V. Del Duca, *A Subtraction scheme for computing QCD jet cross sections at NNLO: Regularization of doubly-real emissions*, JHEP **01** (2007), 070, [arXiv:hep-ph/0609042 [hep-ph]].

[81] G. Somogyi and Z. Trocsanyi, *A Subtraction scheme for computing QCD jet cross sections at NNLO: Regularization of real-virtual emission*, JHEP **01** (2007), 052, [arXiv:hep-ph/0609043 [hep-ph]].

[82] R. Boughezal, X. Liu and F. Petriello, *N-jettiness soft function at next-to-next-to-leading order*, Phys.Rev. **D91** (2015), no. 9, 094035, [arXiv:1504.02540 [hep-ph]].

[83] A. Gehrmann-De Ridder, T. Gehrmann, E. W. N. Glover and G. Heinrich, *Infrared structure of $e^+e^- \to 3$ jets at NNLO*, JHEP **11** (2007), 058, [arXiv:0710.0346 [hep-ph]].

[84] A. Gehrmann-De Ridder, T. Gehrmann, E. W. N. Glover and G. Heinrich, *NNLO QCD corrections to event shape variables in electron positron annihilation*, J. Phys. Conf. Ser. **110** (2008), 022014, [arXiv:0709.4221 [hep-ph]].

[85] S. Weinzierl, *NNLO corrections to 3-jet observables in electron-positron annihilation*, Phys. Rev. Lett. **101** (2008), 162001, [arXiv:0807.3241 [hep-ph]].

[86] V. Del Duca, C. Duhr, G. Somogyi, F. Tramontano and Z. Trócsányi, *Higgs boson decay into b-quarks at NNLO accuracy*, JHEP **04** (2015), 036, [arXiv:1501.07226 [hep-ph]].

[87] G. Bozzi, S. Catani, D. de Florian and M. Grazzini, *Transverse-momentum resummation and the spectrum of the Higgs boson at the LHC*, Nucl.Phys. **B737** (2006), 73–120, [arXiv:hep-ph/0508068 [hep-ph]].

[88] S. Catani, L. Cieri, D. de Florian, G. Ferrera and M. Grazzini, *Universality of transverse-momentum resummation and hard factors at the NNLO*, Nucl.Phys. **B881** (2014), 414–443, [arXiv:1311.1654 [hep-ph]].

[89] S. Catani, *The Singular behavior of QCD amplitudes at two loop order*, Phys.Lett. **B427** (1998), 161–171, [arXiv:hep-ph/9802439 [hep-ph]].

[90] S. Catani and M. Grazzini, *Higgs Boson Production at Hadron Colliders: Hard-Collinear Coefficients at the NNLO*, Eur.Phys.J. **C72** (2012), 2013, [arXiv:1106.4652 [hep-ph]].

[91] S. Catani, L. Cieri, D. de Florian, G. Ferrera and M. Grazzini, *Vector boson production at hadron colliders: hard-collinear coefficients at the NNLO*, Eur.Phys.J. **C72** (2012), 2195, [arXiv:1209.0158 [hep-ph]].

[92] M. Procura, W. J. Waalewijn and L. Zeune, *Resummation of Double-Differential Cross Sections and Fully-Unintegrated Parton Distribution Functions*, JHEP **1502** (2015), 117, [arXiv:1410.6483 [hep-ph]].

[93] A. Jain, M. Procura and W. J. Waalewijn, *Fully-Unintegrated Parton Distribution and Fragmentation Functions at Perturbative k_T*, JHEP **1204** (2012), 132, [arXiv:1110.0839 [hep-ph]].

[94] J. R. Gaunt and M. Stahlhofen, *The Fully-Differential Quark Beam Function at NNLO*, JHEP **1412** (2014), 146, [arXiv:1409.8281 [hep-ph]].

[95] G. P. Lepage, *A New Algorithm for Adaptive Multidimensional Integration*, J.Comput.Phys. **27** (1978), 192.

[96] R. Kleiss and R. Pittau, *Weight optimization in multichannel Monte Carlo*, Comput.Phys.Commun. **83** (1994), 141–146, [arXiv:hep-ph/9405257 [hep-ph]].

[97] C. G. Papadopoulos, *PHEGAS: A Phase space generator for automatic cross-section computation*, Comput.Phys.Commun. **137** (2001), 247–254, [arXiv:hep-ph/0007335 [hep-ph]].

[98] S. Kallweit, J. M. Lindert, P. Maierhöfer, S. Pozzorini and M. Schönherr, *NLO electroweak automation and precise predictions for W+multijet production at the LHC*, arXiv:1412.5157 [hep-ph].

[99] T. Matsuura, S. van der Marck and W. van Neerven, *The Calculation of the Second Order Soft and Virtual Contributions to the Drell-Yan Cross-Section*, Nucl.Phys. **B319** (1989), 570.

[100] T. Gehrmann and E. Remiddi, *Numerical evaluation of two-dimensional harmonic polylogarithms*, Comput.Phys.Commun. **144** (2002), 200–223, [arXiv:hep-ph/0111255 [hep-ph]].

[101] J. Vollinga and S. Weinzierl, *Numerical evaluation of multiple polylogarithms*, Comput.Phys.Commun. **167** (2005), 177, [arXiv:hep-ph/0410259 [hep-ph]].

[102] C. W. Bauer, A. Frink and R. Kreckel, *Introduction to the GiNaC framework for symbolic computation within the C++ programming language*, arXiv:cs/0004015 [cs-sc].

[103] A. Denner, S. Dittmaier and L. Hofer, *COLLIER - A fortran-library for one-loop integrals*, PoS **LL2014** (2014), 071, [arXiv:1407.0087 [hep-ph]].

[104] A. Denner and S. Dittmaier, *Reduction schemes for one-loop tensor integrals*, Nucl.Phys. **B734** (2006), 62–115, [arXiv:hep-ph/0509141 [hep-ph]].

[105] G. Ossola, C. G. Papadopoulos and R. Pittau, *Reducing full one-loop amplitudes to scalar integrals at the integrand level*, Nucl.Phys. **B763** (2007), 147–169, [arXiv:hep-ph/0609007 [hep-ph]].

[106] G. Ossola, C. G. Papadopoulos and R. Pittau, *CutTools: A Program implementing the OPP reduction method to compute one-loop amplitudes*, JHEP **0803** (2008), 042, [arXiv:0711.3596 [hep-ph]].

[107] A. van Hameren, *OneLOop: For the evaluation of one-loop scalar functions*, Comput.Phys.Commun. **182** (2011), 2427–2438, [arXiv:1007.4716 [hep-ph]].

[108] S. Frixione, *Isolated photons in perturbative QCD*, Phys.Lett. **B429** (1998), 369–374, [arXiv:hep-ph/9801442 [hep-ph]].

[109] D. de Florian, G. Ferrera, M. Grazzini and D. Tommasini, *Higgs boson production at the LHC: transverse momentum resummation effects in the H→2gamma, H→WW→lnu lnu and H→ZZ→4l decay modes*, JHEP **1206** (2012), 132, [arXiv:1203.6321 [hep-ph]].

[110] R. V. Harlander, A. Tripathi and M. Wiesemann, *Higgs production in bottom quark annihilation: Transverse momentum distribution at NNLO+NNLL*, Phys.Rev. **D90** (2014), no. 1, 015017, [arXiv:1403.7196 [hep-ph]].

[111] J. C. Collins and D. E. Soper, *Angular Distribution of Dileptons in High-Energy Hadron Collisions*, Phys. Rev. **D16** (1977), 2219.

[112] S. Catani, D. de Florian, G. Ferrera and M. Grazzini, *Vector boson production at hadron colliders: transverse-momentum resummation and leptonic decay*, arXiv:1507.06937 [hep-ph].

[113] M. Grazzini, *Vector-boson pair production at NNLO*, PoS **LL2014** (2014), 027, [arXiv:1407.1618 [hep-ph]].

[114] J. Ohnemus, *Order α_s calculations of hadronic $W^{\pm}\gamma$ and $Z\gamma$ production*, Phys.Rev. **D47** (1993), 940–955.

[115] U. Baur, T. Han and J. Ohnemus, *QCD corrections and anomalous couplings in $Z\gamma$ production at hadron colliders*, Phys.Rev. **D57** (1998), 2823–2836, [arXiv:hep-ph/9710416 [hep-ph]].

[116] D. De Florian and A. Signer, *W gamma and Z gamma production at hadron colliders*, Eur.Phys.J. **C16** (2000), 105–114, [arXiv:hep-ph/0002138 [hep-ph]].

[117] L. Ametller, E. Gava, N. Paver and D. Treleani, *Role of the QCD Induced Gluon - Gluon Coupling to Gauge Boson Pairs in the Multi - Tev Region*, Phys.Rev. **D32** (1985), 1699.

[118] J. van der Bij and E. N. Glover, *Photon Z Boson Pair Production Via Gluon Fusion*, Phys.Lett. **B206** (1988), 701.

[119] K. Adamson, D. de Florian and A. Signer, *Gluon induced contributions to $Z\gamma$ production at hadron colliders*, Phys.Rev. **D67** (2003), 034016, [arXiv:hep-ph/0211295 [hep-ph]].

[120] J. M. Campbell, R. K. Ellis and C. Williams, *Vector boson pair production at the LHC*, JHEP **1107** (2011), 018, [arXiv:1105.0020 [hep-ph]].

[121] W. Hollik and C. Meier, *Electroweak corrections to gamma Z production at hadron colliders*, Phys.Lett. **B590** (2004), 69–75, [arXiv:hep-ph/0402281 [hep-ph]].

[122] E. Accomando, A. Denner and C. Meier, *Electroweak corrections to $W\gamma$ and $Z\gamma$ production at the LHC*, Eur.Phys.J. **C47** (2006), 125–146, [arXiv:hep-ph/0509234 [hep-ph]].

[123] A. Denner, S. Dittmaier, M. Hecht and C. Pasold, *NLO QCD and electroweak corrections to $W+\gamma$ production with leptonic W-boson decays*, JHEP **1504** (2015), 018, [arXiv:1412.7421 [hep-ph]].

[124] K. Hamilton, P. Nason and G. Zanderighi, *MINLO: Multi-Scale Improved NLO*, JHEP **1210** (2012), 155, [arXiv:1206.3572 [hep-ph]].

[125] L. Barze, M. Chiesa, G. Montagna, P. Nason, O. Nicrosini et al., *$W\gamma$ production in hadronic collisions using the POWHEG+MiNLO method*, JHEP **1412** (2014), 039, [arXiv:1408.5766 [hep-ph]].

[126] J. Butterworth, G. Dissertori, S. Dittmaier, D. de Florian, N. Glover et al., *Les Houches 2013: Physics at TeV Colliders: Standard Model Working Group Report*, arXiv:1405.1067 [hep-ph].

[127] V. Khachatryan et al., CMS collaboration, *Measurement of the $Z\gamma$ production cross section in pp collisions at 8 TeV and search for anomalous triple gauge boson couplings*, arXiv:1502.05664 [hep-ex].

[128] G. Aad et al., ATLAS collaboration, *Observation and measurement of Higgs boson decays to WW^* with the ATLAS detector*, arXiv:1412.2641 [hep-ex].

[129] S. Catani, D. de Florian and M. Grazzini, *Direct Higgs production and jet veto at the Tevatron and the LHC in NNLO QCD*, JHEP **0201** (2002), 015, [arXiv:hep-ph/0111164 [hep-ph]].

[130] A. Banfi, P. F. Monni, G. P. Salam and G. Zanderighi, *Higgs and Z-boson production with a jet veto*, Phys.Rev.Lett. **109** (2012), 202001, [arXiv:1206.4998 [hep-ph]].

[131] T. Becher and M. Neubert, *Factorization and NNLL Resummation for Higgs Production with a Jet Veto*, JHEP **1207** (2012), 108, [arXiv:1205.3806 [hep-ph]].

[132] I. W. Stewart, F. J. Tackmann, J. R. Walsh and S. Zuberi, *Jet p_T resummation in Higgs production at $NNLL' + NNLO$*, Phys.Rev. **D89** (2014), no. 5, 054001, [1307.1808].

[133] I. W. Stewart and F. J. Tackmann, *Theory Uncertainties for Higgs and Other Searches Using Jet Bins*, Phys.Rev. **D85** (2012), 034011, [arXiv:1107.2117 [hep-ph]].

[134] S. Catani and B. Webber, *Infrared safe but infinite: Soft gluon divergences inside the physical region*, JHEP **9710** (1997), 005, [arXiv:hep-ph/9710333 [hep-ph]].

[135] R. Hamberg, W. van Neerven and T. Matsuura, *A Complete calculation of the order α_s^2 correction to the Drell-Yan K factor*, Nucl.Phys. **B359** (1991), 343–405.

[136] K. Mikaelian, M. Samuel and D. Sahdev, *The Magnetic Moment of Weak Bosons Produced in pp and $p\bar{p}$ Collisions*, Phys.Rev.Lett. **43** (1979), 746.

[137] U. Baur, S. Errede and G. L. Landsberg, *Rapidity correlations in $W\gamma$ production at hadron colliders*, Phys.Rev. **D50** (1994), 1917–1930, [arXiv:hep-ph/9402282 [hep-ph]].

[138] J. Ohnemus and J. Owens, *An Order α_s calculation of hadronic ZZ production*, Phys.Rev. **D43** (1991), 3626–3639.

[139] B. Mele, P. Nason and G. Ridolfi, *QCD radiative corrections to Z boson pair production in hadronic collisions*, Nucl.Phys. **B357** (1991), 409–438.

[140] J. Ohnemus, *Hadronic ZZ, W^-W^+, and $W^\pm Z$ production with QCD corrections and leptonic decays*, Phys.Rev. **D50** (1994), 1931–1945, [arXiv:hep-ph/9403331 [hep-ph]].

[141] J. M. Campbell and R. K. Ellis, *An Update on vector boson pair production at hadron colliders*, Phys.Rev. **D60** (1999), 113006, [arXiv:hep-ph/9905386 [hep-ph]].

[142] L. J. Dixon, Z. Kunszt and A. Signer, *Vector boson pair production in hadronic collisions at order α_s : Lepton correlations and anomalous couplings*, Phys.Rev. **D60** (1999), 114037, [arXiv:hep-ph/9907305 [hep-ph]].

[143] L. J. Dixon, Z. Kunszt and A. Signer, *Helicity Amplitudes for $\mathcal{O}(\alpha_s)$ Production of W^+W^-, $W^\pm Z$, ZZ, $W^\pm\gamma$, or $Z\gamma$ pairs at hadron colliders*, Nucl.Phys. **B531** (1998), 3–23, [arXiv:hep-ph/9803250 [hep-ph]].

[144] E. N. Glover and J. van der Bij, *Z-boson pair production via gluon fusion*, Nucl.Phys. **B321** (1989), 561.

[145] D. A. Dicus, C. Kao and W. Repko, *Gluon Production of Gauge Bosons*, Phys.Rev. **D36** (1987), 1570.

[146] T. Matsuura and J. van der Bij, *Characteristics of leptonic signals for Z boson pairs at hadron colliders*, Z.Phys. **C51** (1991), 259–266.

[147] C. Zecher, T. Matsuura and J. van der Bij, *Leptonic signals from off-shell Z boson pairs at hadron colliders*, Z.Phys. **C64** (1994), 219–226, [arXiv:hep-ph/9404295 [hep-ph]].

[148] T. Binoth, N. Kauer and P. Mertsch, *Gluon-induced QCD corrections to pp → ZZ → $\ell\bar{\ell}\ell'\bar{\ell}'$*, 142, arXiv:0807.0024 [hep-ph].

[149] A. Bierweiler, T. Kasprzik and J. H. Kühn, *Vector-boson pair production at the LHC to $\mathcal{O}(\alpha^3)$ accuracy*, JHEP **1312** (2013), 071, [arXiv:1305.5402 [hep-ph]].

[150] G. Aad et al., ATLAS collaboration, *Measurement of ZZ production in pp collisions at $\sqrt{s} = 7$ TeV and limits on anomalous ZZZ and ZZγ couplings with the ATLAS detector*, JHEP **1303** (2013), 128, [arXiv:1211.6096 [hep-ex]].

[151] S. Chatrchyan et al., CMS collaboration, *Measurement of the ZZ production cross section and search for anomalous couplings in $2\ell 2\ell'$ final states in pp collisions at $\sqrt{s} = 7$ TeV*, JHEP **1301** (2013), 063, [arXiv:1211.4890 [hep-ex]].

[152] T. A. collaboration, ATLAS collaboration, *Measurement of the total ZZ production cross section in proton-proton collisions at $\sqrt{s}$ = 8 TeV in 20 fb^{-1} with the ATLAS detector*.

[153] V. Khachatryan et al., CMS collaboration, *Measurement of the pp → ZZ production cross section and constraints on anomalous triple gauge couplings in four-lepton final states at $\sqrt{s}$ =8 TeV*, Phys.Lett. **B740** (2015), 250–272, [arXiv:1406.0113 [hep-ex]].

[154] F. Caola and K. Melnikov, *Constraining the Higgs boson width with ZZ production at the LHC*, Phys.Rev. **D88** (2013), 054024, [arXiv:1307.4935 [hep-ph]].

[155] J. M. Campbell, R. K. Ellis and C. Williams, *Bounding the Higgs width at the LHC using full analytic results for $gg \to e^-e^+\mu^-\mu^+$*, JHEP **04** (2014), 060, [arXiv:1311.3589 [hep-ph]].

[156] G. Aad et al., ATLAS collaboration, *Determination of the off-shell Higgs boson signal strength in the high-mass ZZ and WW final states with the ATLAS detector*, arXiv:1503.01060 [hep-ex].

[157] V. Khachatryan et al., CMS collaboration, *Measurement of the pp → ZZ production cross section and constraints on anomalous triple gauge couplings in four-lepton final states at $\sqrt{s}$ =8 TeV*, Phys. Lett. **B740** (2015), 250–272, [arXiv:1406.0113 [hep-ex]].

[158] J. Ohnemus, *An Order α_s calculation of hadronic W^-W^+ production*, Phys.Rev. **D44** (1991), 1403–1414.

[159] S. Frixione, *A Next-to-leading order calculation of the cross-section for the production of W^+W^- pairs in hadronic collisions*, Nucl.Phys. **B410** (1993), 280–324.

[160] E. N. Glover and J. van der Bij, *Vector Boson Pair Production Via Gluon Fusion*, Phys.Lett. **B219** (1989), 488.

[161] T. Binoth, M. Ciccolini, N. Kauer and M. Kramer, *Gluon-induced WW background to Higgs boson searches at the LHC*, JHEP **0503** (2005), 065, [arXiv:hep-ph/0503094 [hep-ph]].

[162] T. Binoth, M. Ciccolini, N. Kauer and M. Kramer, *Gluon-induced W-boson pair production at the LHC*, JHEP **0612** (2006), 046, [arXiv:hep-ph/0611170 [hep-ph]].

[163] A. Bierweiler, T. Kasprzik, J. H. Kühn and S. Uccirati, *Electroweak corrections to W-boson pair production at the LHC*, JHEP **1211** (2012), 093, [arXiv:1208.3147 [hep-ph]].

[164] J. Baglio, L. D. Ninh and M. M. Weber, *Massive gauge boson pair production at the LHC: a next-to-leading order story*, Phys.Rev. **D88** (2013), 113005, [1307.4331].

[165] M. Billoni, S. Dittmaier, B. Jäger and C. Speckner, *Next-to-leading order electroweak corrections to $pp \to W^+W^- \to 4$ leptons at the LHC in double-pole approximation*, JHEP **1312** (2013), 043, [arXiv:1310.1564 [hep-ph]].

[166] M. Grazzini, *Soft-gluon effects in WW production at hadron colliders*, JHEP **0601** (2006), 095, [arXiv:hep-ph/0510337 [hep-ph]].

[167] Y. Wang, C. S. Li, Z. L. Liu, D. Y. Shao and H. T. Li, *Transverse-Momentum Resummation for Gauge Boson Pair Production at the Hadron Collider*, Phys.Rev. **D88** (2013), 114017, [1307.7520].

[168] P. Meade, H. Ramani and M. Zeng, *Transverse momentum resummation effects in W^+W^- measurements*, Phys.Rev. **D90** (2014), no. 11, 114006, [arXiv:1407.4481 [hep-ph]].

[169] M. Grazzini, S. Kallweit, D. Rathlev and M. Wiesemann, *Transverse-momentum resummation for vector-boson pair production at NNLL+NNLO*, arXiv:1507.02565 [hep-ph].

[170] P. Jaiswal and T. Okui, *Explanation of the WW excess at the LHC by jet-veto resummation*, Phys.Rev. **D90** (2014), no. 7, 073009, [arXiv:1407.4537 [hep-ph]].

[171] S. Dawson, I. M. Lewis and M. Zeng, *Threshold resummed and approximate next-to-next-to-leading order results for W^+W^- pair production at the LHC*, Phys.Rev. **D88** (2013), no. 5, 054028, [1307.3249].

[172] V. M. Abazov et al., D0 collaboration, *Measurements of WW and WZ production in W + jets final states in $p\bar{p}$ collisions*, Phys.Rev.Lett. **108** (2012), 181803, [arXiv:1112.0536 [hep-ex]].

[173] T. C. Collaboration, CMS collaboration, *Measurement of the W^+W^- Production Cross Section and Differential Cross Sections with Jets in $p\bar{p}$ Collisions at $\sqrt{s} = 1.96$ TeV*, CDF note **11098** (2014)

[174] D. E. Morrissey, T. Plehn and T. M. Tait, *Physics searches at the LHC*, Phys.Rept. **515** (2012), 1–113, [arXiv:0912.3259 [hep-ph]].

[175] P. F. Monni and G. Zanderighi, *On the excess in the inclusive $W^+W^- \to l^+l^-\nu\bar{\nu}$ cross section*, arXiv:1410.4745 [hep-ph].

[176] A. Denner, S. Dittmaier, S. Kallweit and S. Pozzorini, *NLO QCD corrections to off-shell top-antitop production with leptonic decays at hadron colliders*, JHEP **1210** (2012), 110, [arXiv:1207.5018 [hep-ph]].

[177] A. Martin, W. Stirling, R. Thorne and G. Watt, *Heavy-quark mass dependence in global PDF analyses and 3- and 4-flavour parton distributions*, Eur.Phys.J. **C70** (2010), 51–72, [arXiv:1007.2624 [hep-ph]].

[178] V. Khachatryan et al., *Measurement of the WW cross section in pp collisions at $\sqrt{s}$ = 8 TeV and limits on anomalous gauge couplings*, Tech. Report CERN-PH-EP-2015-122. CMS-SMP-14-016-003. arXiv:1507.03268 , CERN, Geneva, Jul 2015, Comments: Submitted to EPJC.

[179] S. Heinemeyer et al., LHC Higgs Cross Section Working Group collaboration, *Handbook of LHC Higgs Cross Sections: 3. Higgs Properties*, arXiv:1307.1347 [hep-ph].

[180] G. Bozzi, S. Catani, G. Ferrera, D. de Florian and M. Grazzini, *Production of Drell-Yan lepton pairs in hadron collisions: Transverse-momentum resummation at next-to-next-to-leading logarithmic accuracy*, Phys. Lett. **B696** (2011), 207–213, [arXiv:1007.2351 [hep-ph]].

[181] R. Frederix and M. Grazzini, *Higher-order QCD effects in the $h \to ZZ$ search channel at the LHC*, Phys. Lett. **B662** (2008), 353–359, [arXiv:0801.2229 [hep-ph]].

[182] R. V. Harlander, H. Mantler and M. Wiesemann, *Transverse momentum resummation for Higgs production via gluon fusion in the MSSM*, JHEP **11** (2014), 116, [arXiv:1409.0531 [hep-ph]].

[183] S. Dittmaier, S. Kallweit and P. Uwer, *NLO QCD corrections to WW+jet production at hadron colliders*, Phys. Rev. Lett. **100** (2008), 062003, [arXiv:0710.1577 [hep-ph]].

[184] J. M. Campbell, R. K. Ellis and G. Zanderighi, *Next-to-leading order predictions for $WW + 1$ jet distributions at the LHC*, JHEP **12** (2007), 056, [arXiv:0710.1832 [hep-ph]].

[185] S. Dittmaier, S. Kallweit and P. Uwer, *NLO QCD corrections to pp/ppbar $\to$ WW+jet+X including leptonic W-boson decays*, Nucl. Phys. **B826** (2010), 18–70, [arXiv:0908.4124 [hep-ph]].

[186] G. Bozzi, S. Catani, D. de Florian and M. Grazzini, *Higgs boson production at the LHC: Transverse-momentum resummation and rapidity dependence*, Nucl. Phys. **B791** (2008), 1–19, [arXiv:0705.3887 [hep-ph]].

[187] C. Collaboration, CMS collaboration, *Measurement of the W^+W^- cross section in pp collisions at sqrt(s) = 8 TeV and limits on anomalous gauge couplings*.

[188] T. Becher, R. Frederix, M. Neubert and L. Rothen, *Automated NNLL + NLO resummation for jet-veto cross sections*, Eur. Phys. J. **C75** (2015), no. 4, 154, [arXiv:1412.8408 [hep-ph]].

[189] P. Nason, *A New method for combining NLO QCD with shower Monte Carlo algorithms*, JHEP **11** (2004), 040, [arXiv:hep-ph/0409146 [hep-ph]].

[190] T. Sjostrand, S. Mrenna and P. Z. Skands, *PYTHIA 6.4 Physics and Manual*, JHEP **05** (2006), 026, [arXiv:hep-ph/0603175 [hep-ph]].

[191] J. D. Long, *Observation and Measurements of the Higgs Boson with the $H \to WW^{(*)} \to \ell\nu\ell\nu$ Decay*, Ph.D. thesis, Michigan U., 2015.

[192] G. Aad et al., ATLAS collaboration, *Search for an additional, heavy Higgs boson in the $H \to ZZ$ decay channel at $\sqrt{s} = 8$ TeV in pp collision data with the ATLAS detector*, arXiv:1507.05930 [hep-ex].

[193] F. Caola, J. M. Henn, K. Melnikov, A. V. Smirnov and V. A. Smirnov, *Two-loop helicity amplitudes for the production of two off-shell electroweak bosons in gluon fusion*, JHEP **06** (2015), 129, [arXiv:1503.08759 [hep-ph]].

[194] A. von Manteuffel and L. Tancredi, *The two-loop helicity amplitudes for $gg \to V_1V_2 \to$ 4 leptons*, JHEP **06** (2015), 197, [arXiv:1503.08835 [hep-ph]].

[195] K. Melnikov and M. Dowling, *Production of two Z-bosons in gluon fusion in the heavy top quark approximation*, Phys. Lett. **B744** (2015), 43–47, [arXiv:1503.01274 [hep-ph]].

Acknowledgement

I would like to thank Massimiliano Grazzini for supervising this thesis, his valuable input, and investment of time and patience during our discussions.

Furthermore, I am indebted to Sophia Borowka and Danilo Paulikat for proofreading this thesis.